UNIVERSITY OF TRENTO

Doctoral School in Civil, Environmental and
Mechanical Engineering

Curriculum 1. Civil and Environmental Engineering

Riccardo Busti

The influence of the Critical Zone on hillslope hydrology and stability

2025 - Doctoral thesis

UNIVERSITY OF TRENTO - Italy
Department of Civil, Environmental and Mechanical Engineering

Doctoral School in Civil, Environmental and Mechanical Engineering
Topic 1. Civil and Environmental Engineering, XXXVII cycle 2021-2025

Doctoral Thesis - April 2026

Riccardo Busti

The influence of the Critical Zone on hillslope hydrology and stability

Supervisors
Giuseppe Formetta (University of Trento DICAM)
Seulgi Moon (University of Californa Los Angeles, Eidgenössische Technische Hochschule Zürich)

Cover Image: Val Campelle, Provincia Autonoma di Trento, Italia

Credits of the Cover Image: Riccardo Busti (all rights reserved)

University of Trento
Doctoral School in Civil, Environmental and Mechanical Engineering
http://web.unitn.it/en/dricam
Via Mesiano 77, I-38123 Trento
Tel. +39 0461 282670 / 2611 - *dicamphd@unitn.it*

Table of Contents

Summary

Chapter 1: Introduction 13

1.1 Motivation 13

1.2 Research Questions and Goals 15

1.3 Thesis structure 17

References 17

Chapter 2: Exploring hydrological dynamics of layered pyroclastic soils by combining laboratory and field experiments with a numerical model 22

2.1 Introduction 24

2.2 Study area and soil properties 27

2.3 Methodology 29
- 2.3.1 Hydrological Modeling 29
- 2.3.2 Application 1 32
- 2.3.3 Application 2 33
- 2.3.4 Model performance quantification and uncertainty analysis 35

2.4 Results 35
- 2.4.1 Application 1 35
- 2.4.2 Application 2 41

2.5 Discussion 44
- 2.5.1 Hydrological responses of layered pyroclastic soils 44
- 2.5.2 Limitations 48

2.6 Conclusions 48

References 50

Chapter 3: Predicting Large-Scale Landslide Initiation Based on the Local Field Factor of Safety: An Application to the Braies Catchment in Northern Italy 57

3.1 Introduction 59

3.2 Study area 62

3.3 Modeling Framework 63
3.3.1 Hydrologic Model 64
3.3.2 Mechanical Model 65
3.3.3 Landslide Model 67

3.4 Applications 70
3.4.1 Benchmark Test on a Slope Instability with Homogeneous Soil 70
3.4.2 Large-Scale Application to the Alto Adige Hillslopes 71

3.5 Results and Discussion 74
3.5.1 Prediction Results and Analysis 74
3.5.2 Practical Implications of Using Physically Based LFS Framework 78
3.5.3 Comparison with Other Landslide Studies in Alto Adige 81
3.5.4 Limitations 82

3.6 Conclusions 84

References 85

Chapter 4: Surface and Subsurface Hydrological Responses to Different Critical Zone Geometries on Steep Hillslopes 93

4.1 Introduction 95

4.2 Study area and data 99

4.3 Methods 102
4.3.1 Critical Zone Models 102
4.3.2 Hydrological Modeling 104
4.3.3 Hydrological model post-processing and data comparison 106

4.4 Results 108
4.4.1 Sprinkling experiment (EXP) 108
4.4.2 Landslide-triggered Rainfall Event (STORM) 113

4.5 Discussion 120
4.5.1 Advance from previous CB1 CZ hydrological modeling 120
4.5.2 Impact of CZ structures on subsurface hydrology 121
4.5.3 Limitations, uncertainties, and future directions 123

4.6 Conclusions 125

References 126

Chapter 5: Integrating Field Geophysics and Stress Modeling to Characterize 3D Subsurface Heterogeneity in the Critical Zone: Implications for Hillslope Hydrology and Landslide .134

5.1 Introduction 135

5.2 Study area 137

5.3 Data and Methods 139

5.3.1 $ks - z$ scenario 139

5.3.2 $ks - \mathrm{vp} - \sigma$ scenario 141

5.4 Numerical simulations 146

5.4.1 Hydrological modeling 146

5.4.2 Landslide modeling 147

5.5 Results and Discussion 149

5.6 Conclusions 153

References 154

Chapter 6: Conclusions 160

6.1 Research outcomes 160

6.2 Limitations and future work 161

6.3 Final comments 163

Supplementary Material 164

Figure 1. (a) Campania region location in South Italy (the study area is pointed with a black dot); (b) Sarno municipality showing the town, the elevation contours, the 1998 landslides (in red), the analysed Tuostolo site (in blue); (c) flume test sketch showing instrument positions and pressure initial condition. Measures are expressed in (mm); (d) digital elevation model with elevation contour lines every 25 m and monitoring station location, the mapped 1998 landslide is highlighted in red; (e) terrain aspect; (f) surface slope; and (g) soil stratigraphy. 28

Figure 2. Interdisciplinary approach between real site (a: view of Tuostolo hillslope and Sarno town and b: example of pyroclastic soil stratigraphy), physical modelling (c: flume test and d: metallic structure) and numerical modelling (e). 29

Figure 3. Application 1 results. Comparison between pressure measurements (grey dots) and simulated values (blue lines) for different tensiometers located in the upper and lower ashes, with relative Kling-Gupta efficiency (KGE). Comparison between soil moisture measurements (grey dots) and simulated values (red lines), with relative KGE. Red lines correspond to ashy layers, while dark red lines correspond to the pumice layer. The red and blue shaded coloured areas are the 95% prediction interval of the Monte Carlo analysis. The dashed vertical lines represent the moments when rainfall intensity changes. 37

Figure 4. Application 1 results. (a) Normalized flux vectors and pressure distribution for a centered cross section at different hours. Red lines correspond to the ash-pumice interfaces. (b) Water balance for the flume and (c) lateral subsurface runoff subdivision across the three layers. The dashed vertical lines in (b, c) represent the moments when rainfall intensity changes. 39

Figure 5. Application 2 results. Starting from the top, observed rainfall, the vertical grey dashed lines refer the dates at which the pressure maps are presented. Comparison between observed (grey dots) and modeled (blue line) pressure in the topsoil tensiometer, with relative Kling-Gupta efficiency (KGE). Comparison between observed (grey dots) and simulated (red lines) soil moisture for at different depths and layers, with relative KGE. Red lines correspond to ashy layers, while dark red lines correspond to the pumice layer. The red and blue shaded coloured areas are the 95% prediction interval of the Monte Carlo analysis... 43

Figure 6. Application 2 results. Pressure layer maps above each soil interface. Maps are shown moving to the right with increasing depth and moving down with increasing time... 47

Figure 7. Hydromechanical framework for stability analysis of variably saturated hillslopes: geomorphologic model; hydrologic model; and mechanical and landslide models. The framework is independent of the hydrological model usde. The java-based mechanical and landslide model is presented in this paper.(Modified from Lu and Godt 2013.)... 62

Figure 8. (a) Orthophoto of the Braies municipality, with an inset showing its location within the Province of Bolzano, northern Italy. Mapped August 5^{th}-6^{th}, 2017 landslide features include points, scars or deposits, and flow paths. (b) Time series of rainfall (shaded area) and

temperature (black line) used in the hydrological analysis; (c) digital elevation model; (d) slope map; and (e) land cover classification map, where categories are: 1 = agricultural land, 2 = shrubs, 3 = urban area, 4 = forest, 5 = water bodies, 6 = meadow, 7 = rock, and 8 = debris zones. Panels (a and c-e) show the elaboration of topographic maps (WEBGIS Bolzano 2025) and landslide geospatial features (Ufficio Centro Funzionale Provinciale, personal communication, May 8, 2025). 63

Figure 9. Conceptual model illustrating the local factor of safety (LFS), adapted from Lu et al. (2012). The current stress state (bold line) has a shear stress (dashed line) and a shear strength (dotted line). The gray area is the region of stability individuated by the Coulomb-Mohr criterion. The ratio between these two quantities, $\tau */\tau$ represents the proximity to failure. A reduction in suction stress (due to an increase in positive pore pressure) causes the Mohr circle to shift leftward, decreasing the LFS. When the condition LFS ≤ 1 is satisfied, failure occurs. 69

Figure 10. (a) Hillslope geometry, initial and boundary conditions for hydrologic (water table position and flux at borders) and mechanical models (displacements). The dashed black rectangle is the zoomed-in view shown in Fig. 12; (b) soil water retention curve; (c) hydraulic conductivity function; and (d) suction stress characteristic curve. 71

Figure 11. Cross sections of 9 failed hillslope pointed out in Fig. 8-a. For each hillslope we display: the soil layer (in dark grey), the bedrock layer (in light grey), the soil depth map close to the landslide area. Dashed rectangle is the zoom in view showed in Figs. 14 and 15. 73

Figure 12. Soil moisture, suction stress, and LFS contours in a hillslope with constant slope angle and homogeneous soil at 0, 1, 3, 15 h. The first column shows the evolution of the infiltration, the second column shows the evolution in the suction stress field, and the third column shows the evolution of the failure surface, indicated by the red is with LFS ≤ 1. 75

Figure 13. Time series of suction stress (dashed line) and local field safety factor (solid line) in correspondence of the 9 triggered landslides at different depths (i.e., 0.5 m, 1m and right above the soil-bedrock interface), together with the rainfall intensity (on top). Gray area indicates the region of LFS ≤ 1. The shaded area represents the 5th-95th percentile prediction interval of the LFS at the base of the soil,

derived from the Monte Carlo analysis performed on soil friction angle and soil cohesion. 76

Figure 14. Cross sections of 9 hillslopes within the Braies catchment before the storm. The LFS is mapped along each hillslope, with darker shades representing areas of higher stability. 78

Figure 15. Cross sections of 9 hillslopes within the Braies catchment at the timing of landslide occurrences. The LFS is mapped along each hillslope, with darker shades representing areas of higher stability. The red segments indicate portions of the soil where LFS ≤ 1, corresponding to the initiation zones of landslides........................... 79

Figure 16. (a) Location map for the CB1 study area in the Oregon Coast Range (from Ebel et al. 2007a). (b) Digital elevation model with North–South (in red, profile shown in panels j and k) and East–West (in blue, profile shown in panel l) cross-sections, with CB1 boundary, 1996 landslide scar and bedrock fractures open after the event. (c) Soil thickness which is used also as CZ(soil) scenario. (d) Locations of measurement instruments: 14 piezometers, 100 tensiometers, 1 upper weir, and 1 lower weir; the grey background indicates terrain aspect, also used in subsequent figures. (e) Spatial distribution of cumulative rainfall from 13 sprinklers during Experiment 3. The yellow contour indicates the target mean cumulative rate, corresponding to a constant application rate of 1.65 mm/h and a total of 274 mm over 166 hours (Ebel et al. 2007a). (f, g, h) Depth from the surface to the unweathered bedrock and, in white contours, thickness of weathered bedrock for the CZ(RD4m), CZ(RD9m), and CZ(stress) scenarios, respectively. (i) Rainfall intensity during the November 1996 storm (black line filled in grey) and air temperature (red line). The blue shaded area represents cumulative rainfall from 00:00 on November 15th to 20:00 on November 18th, 1996. (j) North-South view of each layer with an inset on the top-right position showing a schematic view of the full computational domain. (k) N-S and (l) E-W cross section showing the depth of the CZ structure in each scenario. The grey dashed zoom areas in these panels show the extent of the cross section visualized in Fig. 7 and in the supplementary material Fig. S5 to S8. Bottom left corner maps coordinates are (x,y)=(410002,4812902.5) in EPSG:26910 reference system. 100

Figure 17. a EXP results. Scatter plot between observed and simulated pore water pressure in the 100 tensiometers for each CZ scenario subdivided by ks=10^{-7} m/s (a, b, c, d) and ks=10^{-10} m/s (e, f, g, h). The

color ranges from blue (begin of the experiment in May 27th, 1992) to red (after the end of the experiment in June 7th, 1992). The dashed-grey lines indicate the separation between unsaturated-saturated domains. (i) histogram and (k, l, m, n) spatial variation of NBIAS across all CZ for ks=10^{-7} m/s. (j, o, p, q, r) The same for ks=10^{-10} m/s. 109

Figure 18. Comparison between modeled and observed discharge during EXP at the Upper Weir, at Lower Weir and their Sum for each CZ scenario subdivided by ks=10^{-7} m/s (a, b, c) and ks=10^{-10} m/s (e, f, g). In the background (c, g), the mean measured sprinkling rate in grey. Comparison between modeled and observed discharge during STORM at the Upper Weir ks=10^{-7} m/ (d) and ks=10^{-10} m/s (h)... 112

Figure 19. STORM results. Simulated pore water pressure at soil base for each CZ scenario subdivided by ks=10^{-7} m/s (left panels) and ks=10^{-10} m/s (right panels) at landslide timing, 2, 12 and 24 hours before. From top to bottom, the degree of bedrock weathering increases, while from left to right, the time approaches the landslide event. Red colors indicate unsaturated areas and blue colors saturated areas. Dashed black line is the 1996 CB1 landslide scar, continuous black lines are the fractures exposed after the event........................ 114

Figure 20. STORM results. Comparison between simulated and observed soil saturation ratio h/z for 14 piezometers at landslide time. The sub-panels (a to h) show scatter plots of measured against simulated h/z values for each CZ scenario subdivided by ks=10^{-7} m/s (a, b, c, d) and ks=10^{-10} m/s (e, f, g, h). Marker shape indicates the absolute error quantile, and color represents soil thickness. (i) Piezometer locations colored by the observed h/z. The sub-panels (j to q) display the extent of the saturated area at landslide time (black hatch) and the piezometers colored by soil depth and shaped according to absolute error quantile for all CZ and bedrock conductivities. Dashed black line is the 1996 CB1 landslide scar, continuous black lines are the fractures exposed after the event. 116

Figure 21. STORM results. Simulated seepage angle at soil-bedrock interface for each CZ scenario subdivided by ks=10^{-7} m/s (left panels) and ks=10^{-10} m/s (right panels) at landslide timing, 2, 12 and 24 hours before. The angle indicates the flux orientation with respect to soil base: $\lambda > 90$ water is infiltrating into bedrock, $\lambda \sim 90$ water flow is slope parallel, $\lambda < 90$ the water is exfiltrating from the bedrock.

Dashed black line is the 1996 CB1 landslide scar, continuous black lines are the fractures exposed after the event. 117

Figure 22. STORM results. North-South CB1 profile showing pressure field and flux direction and magnitude (in log scale) for each CZ scenario at landslide time subdivided by ks=10^{-7} m/s (a, b, c, d) and ks=10^{-10} m/s s (e, f, g, h). East-West CB1 profile showing pressure field and flux direction and magnitude (in log scale) for each CZ scenario at landslide time subdivided by ks=10^{-7} m/s (i, j, k, l) and ks=10^{-10} m/s (m, n, o, p). Black lines represent topographic surface, soil-bedrock boundary and, if present, weathered- unweathered bedrock boundary. The red line represents the position of the water table. The sub-panel are the zoomed-in area depicted in Fig. 16-k,l. 119

Figure 23. (a) Aerial photo of CB1 catchment and inset showing its location in Mettman Ridge, Coosbay, Oregon. (b) B1 catchment outline (dashed black line) with channel network (cyan line); at the ridge are shown the experimental catchment CB1 (black bold line), and the two seismic refraction survey lines (red and blue bold lines). (c) Soil depth map and 1996 landslide scar (dashed black line)...... 138

Figure 24. (a) Scatter plot of falling head slug tests into CB1 piezometers showing sample depth and estimated saturated hydraulic conductivity for soil (in red) and weathered bedrock (in blue). Colors get darker as distance from CB1 outlet increases. (b) ECDF of slug test depths. (c) ECDF of slug test saturated conductivities. (d), (e) Exponential decay of ks with z, obtained using four depth mean bins defined by the 25th-percentile interval, for soil and weathered bedrock respectively. (f) ks profiles at the borehole location; horizontal dashed lines indicate the boundaries of soil, oxidized rock and oxidized-fractured rock. “x” markers are raw data....................................... 140

Figure 25. (a) Seismic Line #1 tomogram at the ridge; the inset shows the vertical profile at borehole location. (b) The same for Seismic Line #2 profile across the upper portion of CB1. 142

Figure 26. (a) Seismic Line #1 LCS field at the ridge; the inset shows the vertical profile at borehole location. (b) The same for Seismic Line #2 profile across the upper portion of CB1. 143

Figure 27. Least squares regression of seismic velocity as function of least compressive stresses $vp = vpLCS$. The data are binned such that

each 10% quantile contains an equal number of points for Seismic lines #1 and #2 together. 144

Figure 28. Extrapolated seismic velocity field. (a) North-South view across CB1 hillslope. (b) East-West view across CB1 landslide scar. 145

Figure 29. Linear decay of $\log(ks)$ with vp infered from LCS, obtained using four depth mean bins defined by the 25th-percentile interval, for soil (a) and weathered bedrock (b) respectively. "x" markers are raw data. 146

Figure 30. Saturated hydraulic conductivity scenarios: (a,d) constant scenario $ks - const$; (b,e) depth-decay scenario $ks - z$; (c,f) seismic-decay scenario $ks - pv - \sigma$. Profiles are shown for North-South cross section across CB1 hillslope (a,b,c) and for East-West cross section across CB1 landslide (d,e,f). In (a,b,d,e) the weathered-unweathered bedrock boundary is CZ(RD9m). 148

Figure 31. $ks - const$ results: (a) pore water pressure at soil base; (b) soil saturation ratio h/z; (c) comaprison between observed and simulated h/z in the piezometers. Maps and points are presented at the moment of hillslope failure. The piezometers are colored by the distance from the CB1 outlet, why their shape in (c) is based on the quantiles of the absolute error between measurements and simulations. (d,e,f) The same for $ks - z$. (g,h,f) The same for $ks - vp - \sigma$. The dashed-black line is the 1996 landslide scar, and the three black patches are the fractures exposed after the event. Background is the aspect. 150

Figure 32. $ks - const$ results: (a) seepage vector at soil-bedrock interface; (b) relative frequency of discrete landslides. (c,d) the same for $ks - z$. (e,f) the same for $ks - vp - \sigma$. The dashed-black line is the 1996 landslide scar, and the three black patches are the fractures exposed after the event. Background is the aspect.......................... 152

Table 1. Hydraulic parameters used. 34

Table 2. Hydraulic and mechanical parameters used for the benchmark application 70

Table 3. Hydraulic and mechanical parameters used for the large-scale application 74

Table 4. Van Genuchten hydraulic parameters used for the Soil Water Retention Curve (SWRC, Eq. 1) and Hydraulic Conductivity Function (HCF, Eq. 2) for each CZ layer. Parameter values are taken from Ebel et al. (2007b) and Ebel et al. (2008). The highest value for unweathered bedrock saturated conductivity (*) is from Ebel et al. (2007b), whereas the lowest value (**) is from Rempe and Dietrich (2014). 105

Table 5. a Summary of the GOF indicators (NSE [-] , MAE [m] and NBIAS [-]) for all 100 tensiometers and for the discharges measured at the two weirs during EXP. The GOF were computed first using all instruments, and then considering only those with NSE > 0, following Ebel et al. (2007b). Results are presented for all CZ scenarios, subdivided by saturated hydraulic conductivity values of ks=10^{-7} m/s and ks=10^{-10} m/s. For STORM, the only available measurement in time is the discharge at the upper weir. Bold numbers indicate the best GOF in each column. (UW=upper weir, LW=lower weir, SUM=upper weir+lower weir) 111

Abstract

The Earth's near-surface layer, which extends from the vegetation canopy to unweathered bedrock, is known as the Critical Zone (CZ). It is essential for regulating the incidence of hydrological processes and hydro-geo hazards. Enhancing predictive models of infiltration, discharge production, and landslide initiation, requires an understanding of the relationships between the CZ and hillslope hydrology. In this research, the impact of changes in CZ configuration and characteristics on hillslope hydrology and stability is examined in various geomorphological and climatic contexts.

The research begins by investigating rainfall infiltration mechanisms in the stratified pyroclastic soil-mantled slopes of the Campania region, Southern Italy. Field monitoring, laboratory infiltration experiments, and physically based hydrological modeling were combined to reproduce observed pore-water pressures, soil-moisture dynamics, and subsurface flow mechanisms. The findings enhanced our understanding of rainfall-induced slope instability and provided further insights into the redistribution of water in layered volcanic deposits.

The work expands by using a coupled hydro-mechanical framework to forecast the onset of shallow landslides. The framework combines i) a transient hydrological model with ii) a finite element solver for slope stability in order to iii) compute local field factors of safety (LFS) under dynamic rainfall conditions. The framework's ability to faithfully replicate observed hillslope failures is validated against a benchmark test and actual storm events in the Braies Alpine Catchment, Alto Adige, Northern Italy. This supports the framework's use as a large-scale, cost-effective tool for quantitative hazard assessment in mountainous regions.

The focus then shifts to exploring how the internal structure of the CZ controls hydrological response and slope stability, using the Coos Bay experimental catchment CB1 in Oregon, USA, as a test case. Extensive field data supported hydrological simulations of four distinct CZ configurations, ranging from soil-only to scenarios including variably weathered bedrock layers shaped by topographic and stress-field controls. Simulations of both controlled sprinklers and natural storm

events revealed that the presence of a deep, irregularly weathered bedrock layer controls subsurface storage, groundwater movements, and localized pressure build-up, improving the agreement between simulated and observed streamflow and pore-pressure responses with respect to the commonly adopted soil-unweathered bedrock configuration.

Lastly, the latter study was refined by adding a spatially variable field of hydraulic conductivity at CB1, which was constructed by seismic refraction data, hundreds of field slug tests, and predicted topographic stress fields. The value of combining geophysical constraints with hydromechanical modeling for a more realistic characterization of CZ behavior was demonstrated by the notable improvement in reproducing hydrological responses and slope failure processes derived from the improved characterization of CZ heterogeneity.

All of these studies demonstrate that hillslope hydrology and stability are subject to first-order influences imposed by the CZ shape, stratification, and hydraulic characteristics. To provide more accurate prediction tools for hydrological forecasting and geohazard mitigation, this dissertation emphasizes the importance of explicitly representing CZ heterogeneity in physically-based hydrological analyses.

Chapter 1: Introduction

1.1 Motivation

The US National Research Council defined the Critical Zone (hereafter CZ) as "*the heterogeneous, near surface environment in which complex interactions involving rock, soil, water, air and living organisms regulate the natural habitat and determine availability of life sustaining resources*" (NRC 2001). The CZ is the Earth's permeable near-surface layer, which extends from the vegetation canopy to unweathered fresh bedrock ecompassing coupled physical, biological and chemical processes (e.g., Brantley et al. 2007). Expertises from various scientific disciplines including geology, soil sciences, biology, ecology, geochemistry, hydrology, geomorphology, and more, are needed to understand the CZ structure and its phenomena (e.g., White et al. 2015, Zhang et al. 2024). Over the last decades, hydrology has become an integrative discipline linking environmental and civil applications in the CZ (e.g., Brooks et al. 2015), with a particular interest in the future directions of the coupled human-natural system (Godderis and Brantley 2014). The CZ is essential for regulating the incidence of hydrological processes and hydro-geohazard such as goundwater dynamics (e.g., Fan 2015; Singha and Navarre-Sitchler 2021), evapotranspiration (e.g., Scott and Biederman 2018), nutrients exchange (e.g., Roque-Malo at al. 2020; Dawson et al. 2020), physical and chemical weathering (e.g., Anderson et al. 2007; Chorover et al. 2007; Lin 2010; Fisher et al. 2017;), water resources (e.g., Kirkby 2016), runoff production (e.g., Montgomery and Dietrich 2001; Kim et al. 2017; Zhang et al. 2022), soil erosion (e.g., Rapuc et al. 2021), and landslides (e.g., Montgomery et al. 2009; Moon et al. (under review)).

Recognizing the importance of Earth's critical systems, the U.S. National Science Foundation (NSF) established 46 Critical Zone Observatories (CZOs) in the United States (e.g., Anderson et al. 2008). This effort was followed by the European Union's 17 Soil Transformations in European Catchments (SoilTrEC) sites and similar initiatives worldwide, bringing the total to 64 CZOs across the planet (Giardino and Houser 2015). The CZO program is an interdisciplinary, collaborative research effort aimed at developing a theoretical framework for qualitative and quantitative Earth surface evolution models and for conceptualizing data analysis, both for understanding the past and projecting the future (e.g., White et al. 2015). Addressing such questions requires synoptic, multi-scale investigation that spans from treetops to deep unweathered bedrock. While the near-surface soil-water system is relatively accessible (e.g., Jin and Brantley 2011), the deep CZ, e.i., its thickness, structure, variability and controlling factors remain poorly investigated and understood (e.g., Holbrook et al. 2019). In this case, new strategies of data collection techniques based on remote sensing, geophysical surveys (from surface waves and seismic refraction to electrical and electromagnetic imaging) and high-resolution monitoring systems (e.g., Holbrook et al. 2014; Parsekian et al. 2015; Guo and Lin 2016) gained interests for constrain CZ thickness, porosity, and structure noninvasively and to extrapolate site measurements across hillslopes and catchments where local experiments become transferable and model-ready (e.g., Brantley et al. 2006; Brantley et al. 2016). Recent CZ seismic studies (Flinchum et al. 2025; Eppinger et al. 2025) show advances in geophysics are turning previously hidden structure into measurable, testable variables for hypotheses for controls on deep CZ architecture, by focus attention on lithology, tectonic/structural inheritance, topographic stress, and climate as first-order controls on CZ architecture (e.g., Rempe and Dietrich 2014; St Clair et al. 2015; Riebe et al. 2017).

These efforts are essential for advances in transferable understanding of hydrological processes at hillslope scale and for the developments of CZ hydrological theories (e.g., Montgomery and Dietrich 2001; Salve et al. 2012; Vereckeen et al. 2015) governing subsurface water storage and fluxes and incidence to hydro-geo natural harzard. Landslides, particularly rainfall-induced shallow landslides, represent a destructive natural hazard in mountainous regions, causing significant loss of life and damage to infrastructure globally (e.g., Froude and Petley, 2018) and are in the context of climate change (e.g., Gomez et al. 2023). It is generally recognized that storm-driven pore water pressure rising, and subsurface flow paths can trigger shallow landslides (e.g., Iverson and Major, 1986; Wilson and Dietrich 1987; Montgomery et al. 1997; Bogaard and Greco, 2016; Fan et al. 2019; da Silva et al. 2022). However, the heterogeneous nature and poorly known hydro-mechanical properties of the CZ subsurface layers have made it difficult, but necessary, to represent the real CZ structure in predictive hydro-geo models (e.g., Wang et al. 2025). This can cause significant variations in simulated seepage flow and pore-water pressure development at subsurface strata boundaries (e.g., Montgomery et al. 2002; Capparelli and Versace, 2014), likely affecting the hillslope shallow stability response to rainfall predicted by the model compared to reality. Therefore, there is a need for physical understanding and consequent implementation of the CZ structure and processes that trigger shallow landslides for improving early warning system.

This thesis is carried out to examine the impact of changes in CZ configuration and characteristics on hillslope hydrology and stability in various geomorphological and climatic contexts, i.e., pyroclastic layered soils, alpine landscapes, and weathered sites, to bridge the gap between the complex, observed reality of CZ architecture and the simplified representations currently used in slope hydrological and stability modeling. By explicitly accounting for the heterogeneity of subsurface, weathered bedrock geometry, and hydro-mechanical properties, this work will advance the deterministic prediction of hillslope hydrology and stability within the CZ.

1.2 Research Questions and Goals

Driven by the need to bridge the gap between complex hydrological CZ observations and practical slope stability modeling, this thesis addresses the following key research questions:

1. How does internal CZ structure (soil layering, depth-to-weathered bedrock, and heterogeneity in hydraulic properties) control the timing and spatial distribution of infiltration, subsurface storage, saturation and runoff on hillslopes under natural rainfall regimes?
2. How can coupled hydro-mechanical modelling frameworks, validated with field and laboratory datasets, be used to produce spatially distributed hydrological variables and landslide hazard indicators that reflect CZ controls?
3. At what scales and under which boundary conditions do CZ structure become the dominant determinant of slope instability, as opposed to uniform-soil or bedrock-dominated models commonly used in slope-stability practice?

To answer the research questions above the thesis pursues the following goals by investigating different CZ scenarios across multiple geomorphological and environmental settings:

1. *Pyroclastic layered soils of Southern Italy (Sarno)*: How do stratigraphic discontinuities in layered volcanic soils influence infiltration dynamics and the triggering of shallow landslides? Specifically, how can we improve the prediction of pore-pressure build-up in pyroclastic mantles by combining laboratory parameterization with physically-based modeling? By combining in-situ monitoring, laboratory infiltration experiments, and 3D numerical modeling, this goal aims to quantify the role of hydraulic property contrasts and soil layering in redistributing subsurface water and triggering shallow landslides in pyroclastic layered soils.
2. *Alpine landscapes in North-Eastern Italian Alps (Braies):* Can the integration of transient hydrology with a Local Field Factor of Safety (LFS) approach improve the deterministic prediction of landslide initiation at the catchment scale? Does the use of a coupled hydro-mechanical framework enhance the identification of unstable areas in complex Alpine terrains compared to traditional limit-equilibrium methods? This goal focuses on implementing, testing and validating a framework that integrates a i) distributed hydrological models, with a ii) mechanical model, and a iii) slope stability model to predict the spatial and temporal initiation of multiple landslides at regional scale during severe storm events.
3. *Weathered experimental catchment in Oregon (Coos Bay):* This study examines how deep CZ structure influences subsurface hydrology and slope stability by answering: i) how does deep spatially variable weathered CZ architecture affect discharge, pore-water pressure, and saturation pattern compared with simplified soil-bedrock models? and ii) what is gained by integrating geophysical data and modeled stress fields to create a more realistic 3D representation of subsurface hydro-mechanical properties? To address these questions, the high-instrumented CB1 catchment is tested to address the influence of multiple CZ scenarios on both hydrological

measurements and landslide predictions during controlled experiments and natural storms.

1.3 Thesis structure

The research presented in this thesis is written in a paper-style format, with each chapter (excluding general introduction and conclusions) consisting of an independent scientific journal article. These are either published (the first two: chapter 2 and 3), under review (the third: chapter 4) or in the process of being submitted (the fourth: chapter 5). A short paragraph below the chapter title indicates how the research evolved from the current state of art. This paragraph also indicates the publication or review status of the chapter (i.e., published or under-review for publication)

References

Anderson, S. P., von Blanckenburg, F., and White, A. F. (2007). Physical and Chemical Controls on the Critical Zone. Elements, 3, 315-319.

Anderson, S. P., Bales, R. C., and Duffy, C. J. (2008). Critical Zone Observatories: Building a network to advance interdisciplinary study of Earth surface processes. Mineralogical Magazine, 72 (1), 7-10.

Bogaard, T. A., and Greco, R. (2015). Landslide hydrology: from hydrology to pore pressure. Water, 3 (3), 439-459.

Brantley, S. L., White, T. S., White, A. F., Sparks, D., Richter, D., Pregitzer, K., Derry, L., Chorover, J., Chadwick, O., April, R., Anderson, S., and Amundson, R. (2006). Frontiers in Exploration of the Critical Zone: Report of a workshop sponsored by the National Science Foundation (NSF), October 24-26, 2005, Newark, DE, 30 p.

Brantley, S. L., Goldhaber, M. B., and Ragnarsdottir, V. (2007). Crossing disciplines to understand the Critical Zone. Elements, 3, 307-314.

Brantley, S. L., Di Biase, R. A., Russo, T. A., Shi, Y., Lin, H., Davis, K. J., Kaye, M., Hill, L., Kaye, J., Eissenstat, D. M., Hoagland, B., Dere, A. L., Neal, A. L., Brubaker, K. M., and Arthur, D. K. (2016). Designing a suite of measurements to understand the critical zone, Earth Surface Dynamics, 4, 211-235.

Brooks, P. D., Chorover, J., Fan, Y., Godsey, S. E., Maxwell, R. M., McNamara, J. P., and Tague, C. (2015). Hydrological partitioning in the critical zone: Recent advances and opportunities for developing transferable understanding of water cycle dynamics. Water Resources Research, 51 (9), 6973-6987.

Capparelli, G. and Versace, P. (2014). Analysis of landslide triggering conditions in the Sarno area using a physically based model. Hydrology and Earth System Sciences, 18, 3225-3237.

Chorover, J., Kretzschmar, R., Garcia-Pichel, F., and Sparks, D. L. (2007). Soil Biogeochemical Processes within the Critical Zone. Elements, 3 (5), 321-326.

da Silva, A. C., Resende, I., da Costa, R. C., Uagoda, R. E. S., and Avelar, A. d. S. (2022). Geophysical for granitic joint pattern and subsurface hydrology related to slope instability. Journal of Applied Geophysics, 199, 104607.

Dawson, T. E., Hahm, J. W., and Crutchfield-Peters K. (2020). Digging deeper: what the critical zone perspective adds to the study of plant ecophysiology. New Phytologist, 226 (3), 666-671.

Eppinger, B. J., Holbrook, W. S., Flinchum, B. A., Grana, D., Richter, D. B., Hayes, J. L., Riebe, C. S., Harman, C. J., and Carr, B. J. (2025). On the role of inherited rock fabric in critical zone porosity development: Insights from seismic anisotropy measurements using surface waves. Earth Surface Processes and Landforms, 50 (9), e70132.

Fan Y. (2015). Groundwater in the Earth's critical zone: Relevance to large-scale patterns and processes. Water Resources Research, 51 (5), 3052-2069.

Fan, L., Lehmann, P., Zheng, C., and Or, D. (2019). Rainfall Intensity Temporal Patterns Affect Shallow Landslide Triggering and Hazard Evolution. Geophysical Research Letters, 47 (1), e2019GL085994.

Fisher, B. A., Rendahl, A. K., Aufdenkampe, A. K., and Yoo, L. (2017). Quantifying weathering on variable rocks, an extension of geochemical mass balance: Critical zone and landscape evolution. Earth Surface Processes and Landforms, 42 (14), 2457-2468.

Flinchum, B. A., Holbrook, W. S., Riebe, C. S., Moon, S., Harman, C., Grana, D., Carr, B. J., Hayes, J., Neely, A., Callahan, R., Richter, D. D., Eppinger, B., Uecker, R., Chiaviello, A., and Weinheimer, N. (2025). Using seismic refraction data to estimate a relationship between landscape curvature and deep critical zone structure in the South Carolina Piedmont, USA. Journal of Geophysical Research: Earth Surface, 130, e2025JF008346.

Froude, M. J., and Petley, D. N. (2018). Global fatal landslide occurrence from 2004 to 2016. Natural Hazards and Earth System Sciences, 18, 2161-2181.

Giardino, J. R., and Houser, C. (2015). Chapter 1 - Introduction to the Critical Zone. Developments in Earth Surface Processes, 19, 1-13.

Godderis, Y., and Brantley, S. L. (2014). Earthcasting the future Critical Zone: Elementa, 000019.

Gomez, D., Garcia, E. F., and Aristizabal, E. (2023). Spatial and temporal landslide distributions using global and open landslide databases. Natural Hazards, 117, 25-55.

Guo, L., and Lin, H. (2016). Critical Zone Research and Observatories: Current Status and Future Perspectives. Vadose Zone Journal, 15 (9), 1-14.

Holbrook, W. S., Riebe, C. S., Elwaseif, M. L., Hayes, J., Basler-Reeder, K. L., Harry, D., Malazian, A., Dosseto, A. C., Hartsough, P., and Hopmans, J. W. (2014). Geophysical constraints on deep weathering and water storage potential in the Southern Sierra Critical Zone Observatory. Earth Surface Processes and Landforms, 39 (3), 366-380.

Holbrook, S. W., Marcon, V., Bacon, A. R., Brantley, S. L., Carr, B. J., Flinchum, B. A., Richter, D. D., and Riebe, C. S. (2019).Links between physical and chemical weathering inferred from a 65-m-deep borehole through Earth's critical zone. Scientific Reports, 9, 4495.

Iverson, R. M., and Major, J. J. (1986). Groundwater Seepage Vectors and the Potential for Hillslope Failure and Debris Flow Mobilization. Water Resources Research, 22 (11), 1543-1548.

Jin L., and Brantley, S. L. (2011). Soil chemistry and shale weathering on a hillslope influenced by convergent hydrologic flow regime at the Susquehanna/Shale Hills Critical Zone Observatory. Applied Geochemistry, 22, S51-S56.

Kim, H., Dietrich, W. E., Thurnhoffer, B. M., Bishop, J. K. B., Fung, I. Y. (2017). Controls on solute concentration-discharge relationships revealed by simultaneous hydrochemistry observations of hillslope runoff and stream flow: The importance of critical zone structure. Water Resources Research, 53 (2), 1424-1443.

Kirkby, M. J. (2016). Water in the critical zone: soil, water and life form from profile to planet. Soil, 2, 631-645.

Lin, H. (2010). Earth's critical zone hydropedology: concepts, characteristics and advances. Hydrology and Earth System Sciences, 14 (1), 25-45.

Montgomery, D. R., Dietrich, W. E., Torres, R., Anderson, S. P., Heffner, J. T., and Loague, K. (1997). Hydrologic response of a steep, unchanneled valley to natural and applied rainfall. Water Resources Research, 33 (1), 91-109.

Montgomery, D. R., and Dietrich, W. E. (2001). Runoff generation oa steep, soil-mantled landscape. Water Resources Research, 38 (9), 1168.

Montgomery, D. R., Dietrich, W. E., and J. T. Heffner (2002). Piezometric response in shallow bedrock at CB1: Implications for runoff generation and landsliding. Water Resources Research, 38 (12), 1274.

Montgomery, D. R., Schmidt, K. M., Dietrich, W. E., and McKean, J. (2009). Instrumental record of debris flow initiation during natural rainfall: Implications for modeling slope stability. Journal of Geophysical Research, 114, F01031.

Moon, S., Higa, J. T., Formetta, G., Busti, R., Bellugi, D. G., Dietrich, W. E., Milledge, D. G., and Ebel, B. A. (under review). Deep critical zone controls on shallow landslides. PNAS.

National Research Council Committee on Basic Research Opportunities in the Earth Sciences (2001). Basic Research Opportunities in the Earth Sciences. National Academies Press, Washington DC.

Parsekian, A. D., Singha, L., Minsley, B. J., Holbrook, W. S., and Slater, L. (2015). Multiscale geophysical imaging of the critical zone. Reviews of Geophysics, 53 (1), 1-26.

Rapuc, W., Bounchez, J., Sabatier, P., Genuite K., Poulenard, J., Gaillarder, J., and Arnaud, F. (2021). Quantitative evaluation of human and climate forcing on erosion in the alpine Critical Zone over the last 2000 years. Quaternary Science Reviews, 268, 107127.

Rempe, D. M., and Dietrich, W. E. (2014). A bottom-up control on fresh-bedrock topography under landscapes. Proceedings of the National Academy of Sciences, 111 (18), 6576-6581.

Riebe, C. S., Hahm, W. J., and Brantley, S. L. (2017). Controls on deep critical zone architecture: a historical review and four testable hypotheses. Earth Surface Processes and Landforms, 42 (1), 128-156.

Roque-Malo S., Woo, D. K., and Kumar, P. (2020). Modeling the Role of Root Exudation in Critical Zone Nutrient Dynamics. Water Resources Research, 56 (8), e2019WR026606.

Salve, R., Rempe, D. M., and Dietrich, W. E. (2012). Rain, rock moisture dynamics, and the rapid response of perched groundwater in weathered, fractured argillite underlying a steep hillslope. Water Resources Research, 48, W11528.

Scott, R. L., and Biederman, J. A. (2018). Critical Zone Water Balance Over 13 Years in a Semiarid Savanna. Water Resources Research, 55 (1), 574-588.

Singha, K., and Navarre-Sitchler, A. (2021). The importance of Groundwater in Critical Zone Science. Groundwater, 60 (1), 27-34.

St. Clair, J., Moon, S., Holbrook, W. S., Perron, J. T., Riebe, C. S., Martel, S. J., Carr, B., Harman, C., Singha, K .D., and Richter, D. D. (2015). Geophysical imaging reveals topographic stress control of bedrock weathering. Science, 350 (6260), 534-538.

Vereecken, H., Huisman, J. A., Franssen, H., Brüggemann, N., Bogena, H. R., Kollet, S., Javaux, M., van der Kruk, J., and Vanderborght, J. (2015). Soil hydrology: Recent methodological advances, challenges, and perspectives. Water Resources Research, 51 (4), 2616-2633.

Wang, L., Warix, S., Callahan, R., Sullivan, P., and Singha, K. (2025). Data-Model Integration to Unravel Critical Zone Dynamics: Challenges, Successes, and Future Directions. Water, 12, e70040.

White, T., Brantley, S., Banwart, S., Chorover J., Dietrich, W., Derry, L., Lohse, K., Anderson, S., Aufdenkampe, A., Bales, R., Kumar, P., Richter, D., and McDowell, B. (2015). Chapter 2 - The role of Critical Zone Observatories in Critical Zone Science. Developments in Earth Surface Processes, 19, 15-78.

Wilson, C. J., and Dietrich, W. E. (1987). The contribution of bedrock groundwater flow to storm runoff and high pore pressure development in hollows. document title: IAHS Publication, 49-59.

Zhang, J., Wang, S., Fu, Z., Chen, H., and Wang, K. (2022). Soil thickness controls the rainfall-runoff relationship at the karst hillslope critical zone in southwest China. Journal of Hydrology, 609, 127779.

Zhang, J., Liu, C., and Xu J. (2024). Earth Critical Zone: A comprehensive exploration of the Erth’s surface processes. Earth Critical Zone, 1 (1), 100001.

Chapter 2: Exploring hydrological dynamics of layered pyroclastic soils by combining laboratory and field experiments with a numerical model

Riccardo Busti[1], Capparelli Giovanna[2], Giuseppe Formetta[1]

[1]Department of Civil, Environmental and Mechanical Engineering (DICAM), University of Trento, Trento (TN), Italy

[2]Department of Computer Science, Modelling, Electronics, and Systems Engineering (DIMES), University of Calabria, Arcavacata di Rende (CS), Calabria, Italy

This article advances understanding of hydrological processes in layered pyroclastic soils by integrating field data, laboratory experiments, and a rigorously validated 3D hydrological model to reveal infiltration mechanisms across multiple spatial and temporal scales.

This chapter has been published in *Hydrological Processes*: https://doi.org/10.1002/hyp.15257

Abstract

Rainfall infiltration plays a crucial role in the near-surface response of soils, influencing other hydrological processes (such as surface and subsurface runoff, groundwater dynamics), and thus determining hydro-geomorphological risk assessment and the water resources management policies. In this study, we investigate the infiltration processes in pyroclastic soils of the Campania region, Southern Italy, by combining measured in situ data, physical laboratory model observations and a 3D physically based hydrological model. First, we validate the numerical model against the soil pore water pressure and soil moisture measured at several points in a small-scale flume of a layered pyroclastic deposit during an infiltration test. The objective is to (i) understand and reproduce the physical processes involved in infiltration in layered volcanoclastic slope and (ii) evaluate the ability of the model to reproduce the measured data and the observed subsurface flow patterns and saturation mechanism. Second, we setup the model on the real site where soil samples were collected and simulate the 3D hydrological response of the hillslope. The aim is to understand and model the dynamics of hydrological processes captured by the field observations and explain the redistribution of water in different layers during 2 years of precipitation. For both applications, a Monte Carlo analysis has been performed to account for the hydrological parameter uncertainty. Results show the capability of the model to reproduce the observations in both applications, with mean KGE of 0.84 and 0.68 for pressure and soil moisture data in the laboratory, and 0.83 and 0.55 in the real site. Our results are significant not only because they provide insight into understanding and simulating infiltration processes in layered pyroclastic slopes but also because they may provide the basis for improving geohazard assessment systems, which are expected to increase, especially in the context of a warming climate.

2.1 Introduction

The soil rainfall infiltration is a physical process of great importance due to its implications for water infiltration, groundwater recharge, surface runoff, subsurface drainage and soil erosion, thus determining the hydro-geomorphological risk level in mountain areas (e.g., Sousa et al. 2020).

Pyroclastic soils refer to alternating layers of volcanic ash, pumice, and other volcanoclastic materials originated from various eruptive phases, that have undergone sedimentation and subsequent physical-chemical alterations (e.g., Basile et al. 2003). 5th May 2023 marked the 25th anniversary of the event occurred in 1998 and considered one of the most catastrophic in terms of economic damage and fatalities (160 deaths) in Italy, when more than 400 landslides affecting shallow pyroclastic deposits in Pizzo d'Alvano (Campania region, Southern Italy) were triggered by intense and prolonged rainfall (e.g., Cascini, 2004; Crosta and Dal Negro, 2003; Olivares and Picarelli, 2003).

Rainfall-induced landslides in granular soils are among the most destructive types of natural hazards (e.g., Emberson et al. 2020; Hungr et al. 2001) because of their sudden initiation, high speed of propagation, and increase in mobilized volume during downslope movement (e.g., Damiano et al. 2017; Formetta and Capparelli, 2019; Sorbino et al. 2010), as they can cause damage to buildings, infrastructure and endanger human lives.

This is particularly true for layered pyroclastic soils where the contrasting hydrological properties (e.g., hydraulic conductivity and mechanical features) increase the susceptibility to landslides (e.g., Cascini et al. 2008). The most recent landslide event in Ischia (Gulf of Naples, Campania, southern Italy) occurred during the night between 25th and 26th November 2022, caused 12 victims and destroyed tens of buildings. Therefore, there is a need for improving the physical understanding of the processes that influence the layered pyroclastic soil hydrological response, which in turn will result in improved early warning systems (EWS), saving lives and reduce the societal impact (Costanzo et al. 2015).

Rainfall infiltration process into heterogeneous layered soils represents a complex process, as the contrasting values of hydraulic properties (e.g., saturated hydraulic conductivity) may cause locally diverted flow (e.g., Warrick et al. 1997) or may limit water's infiltration downward from a finer soil into a coarser soil (e.g., Hübner et al. 2017; Stormont and Anderson, 1999). In this context, pyroclastic layered soils differ from traditional homogeneous soils because they originate from volcanic eruptions. During these events, air-fall materials deposit and constitute a sequence of soil layers, which exhibit a high soil porosity and heterogeneous soil structure, permeability and particle sizes (e.g., Picarelli et al. 2006; Roman Quintero et al. 2024).

In the last decades, a great advance in the comprehension of the hydrological processes occurring in the pyroclastic soils focusing on the peri-Vesuvian area, has been achieved through different research techniques, which include (i) long-lasting field monitoring, (ii) laboratory experiments on small-scale physical models and (iii) numerical simulations and (iv) their combination.

Field observations are crucial for collecting long-term hydrological data and developing accurate models of near-surface hydrology of layered pyroclastic soils (e.g., Fusco et al. 2017; Greco et al. 2023). These observations help distinguish between seasonal fluctuations and short-term responses to rainfall. Studies in southern Italy's Cervinara hillslope show that rainfall causes rapid pressure increases near the surface, with less fluctuation in deeper layers (Comegna et al. 2016; Damiano et al. 2012). Seasonal storms in the rainy period December-May can trigger landslides, whereas isolated storms in the period June-August mainly cause erosion (Cascini et al. 2014). One significant feature of pyroclastic soils is the presence of capillary barriers, particularly where coarse pumice layers are interbedded with finer ash layers. These barriers impede vertical water flow, causing water to accumulate above the coarse layers until the hydraulic gradient is sufficient to overcome the barrier (Mancarella et al. 2012; Mancarella and Simeone, 2012). This behaviour was observed over a year of recordings at Pizzo d'Alvano massif (Capparelli and Spolverino, 2022).

Laboratory models of hillslopes allow analysis of hydrological responses under controlled conditions, providing detailed data on pore water pressure, soil moisture and deformations (e.g., Picarelli et al. 2015). Experiments with layered pyroclastic soils show the impact of the pumice layer on flow regimes, delaying wetting fronts and affecting infiltration due to the capillary barrier effect (Capparelli et al. 2020; Damiano et al. 2017; Damiano and Olivares, 2010).

Deterministic hydrological models are powerful numerical tools that simulate interactions between hydrology, geology and geomorphology to understand site responses (e.g., Baum et al. 2010; Cascini et al. 2008; Formetta, Capparelli et al. 2016; Formetta, Simoni et al. 2016; Sorbino et al. 2010). These models, varying in complexity, often use the Richards equation coupled with slope stability models to assess landslide susceptibility. Studies have shown the influence of antecedent conditions on critical rainfall thresholds for landslides, for example, if the dry season is considered, the critical rainfall intensity that triggers landslides remarkably increases (De Vita et al. 2018; Napolitano et al. 2016). Capparelli and Versace (2014) suggest that saturation from deeper layers is not the only reason for instability; rather, the reduction in strength of the upper layer due to water accumulation during prolonged rainfall, combined with short intense storms, leads to hillslope failure. Other studies focused on the influence of topographical factors on landslide susceptibility pointing out critical condition for location where stratigraphic/morphological discontinuities occur, due to localized increase of pore pressure (Cascini et al. 2008; Crosta and Dal Negro, 2003; Tufano et al. 2021). Models are validated against laboratory and field data, showing their reliability in predicting hydrological variables (Damiano et al. 2017; Formetta and Capparelli, 2019; Greco et al. 2013). However, few studies model hydrological variables at both laboratory and hillslope scales (e.g., Damiano and Olivares, 2010).

The aim of this article is to advance the understanding of the hydrological processes occurring in layered pyroclastic soils by exploiting the potential of combining: (i) field measurements, (ii) laboratory experiment results and (iii) model simulations. To reach this goal, we firstly extensively validated and then applied a 3D physically based hydrological model to draw insights on the hydrological infiltration mechanisms occurring in pyroclastic soils. The model applications and conclusions rely on a validation which involves multiple-data (i.e., spatially varying pressure and soil moisture) and multiple-point (across different soil layers and at different depths) measurements, collected across extremely different spatial and temporal scales (from seconds and around one square meter of the laboratory experiments to hourly and half square kilometre of the real site test case).

We focus on two different applications, each of them with specific goals relevance:

- Application 1. Objectives: exploiting the measurement data collected in a laboratory test to understand and model patterns and behaviours of pressure and flow fields on a steep, small-scale, layered volcanoclastic slope. Relevance: verify that the numerical model is capable of: (i) reproducing the pressure and soil moisture observations using the data collected in multiple points and depths of the controlled environment and (ii) mimicking the physical processes occurring in the flume during the infiltration test, for example, capillary barrier effect, the temporal variation of the water flux vectors and the water balance.
- Application 2. Objectives are: (i) transferring the knowledge gained from Application 1 to the Tuostolo hillslope, where continuous measurements of soil moisture were available for 2 years and (ii) setting up the hydrological model and assess whether it can simulate the hydrological response of such a complex hillslope. Relevance: provide reliable insights on multiple years infiltration processes on a real pyroclastic slope, which in turn will be relevant for assessing landslide susceptible areas, improving the accuracy of EWS.

2.2 Study area and soil properties

The study area is in Sarno, Campania region, southern Italy. We analyse the Tuostolo hillslope (100-800 m elevation) of the Pizzo d'Alvano massif, where the 5th May 1998, catastrophic landslides occurred (Fig. 1-a,b). The soil stratigraphy is very heterogeneous in the first few meters below the ground surface along the hillslope cross section (e.g., Cascini et al. 2008). Carbonate rocks are covered by pyroclastic deposits composed of alternating layers of sandy-loam volcanic ash and sandy-gravelly pumice, which are the result of different Somma-Vesuvium eruptive phases and pedogenetic processes (e.g., Capparelli and Versace, 2014; Crosta and Dal Negro, 2003). The hillslope is steep, with angles above 30° and sometimes approaching the measured soil friction angle (38°), where soil stability is achieved through unsaturated pore water pressure (e.g., Capparelli et al. 2020). Rainfall-induced landslides occur in shallow, cohesionless deposits in response to infiltration, which leads to an increase in pore water pressure and thus a decrease in soil strength (e.g., Olivares and Picarelli, 2003).

To understand the dynamics of the unsaturated state and the infiltration processes of the soil mantle, a monitoring station consisting of a tensiometer, and five time-domain reflectometers (TDR) was installed in the upper ridge of the Tuostolo hillslope.

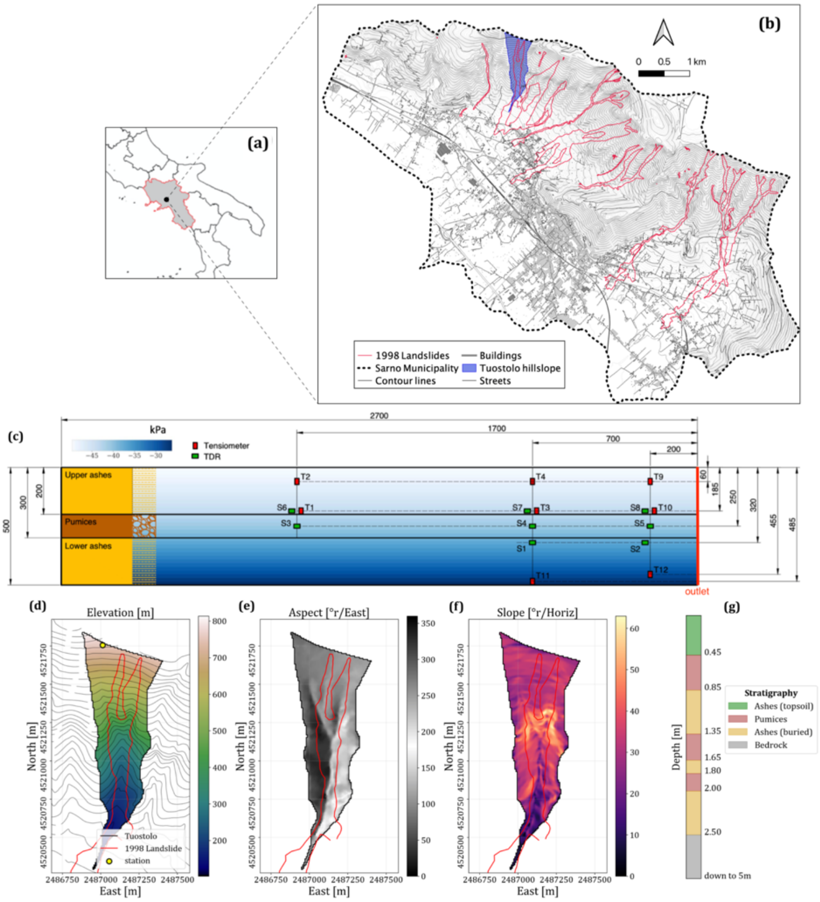

Figure 1. (a) Campania region location in South Italy (the study area is pointed with a black dot); (b) Sarno municipality showing the town, the elevation contours, the 1998 landslides (in red), the analysed Tuostolo site (in blue); (c) flume test sketch showing instrument positions and pressure initial condition. Measures are expressed

in (mm); (d) digital elevation model with elevation contour lines every 25 m and monitoring station location, the mapped 1998 landslide is highlighted in red; (e) terrain aspect; (f) surface slope; and (g) soil stratigraphy.

2.3 Methodology

We use a 3D hydrological model (Section 2.3.1) to simulate two different applications involving pyroclastic soils, at different spatial and temporal resolutions (Fig. 2). First, we reproduce a laboratory experiment to understand the physical processes occurring in a controlled, highly instrumented environment (Application 1, Section 2.3.2). Afterwards, we move to the application on the real site (Application 2, Section 2.3.3) to reproduce the hydrological processes at hillslope scale. Model accuracy is assessed in both applications by comparing the time series of measured pressure and soil moisture in different points and at different depths/soil layers. Finally, a Monte Carlo uncertainty analysis is performed to account for the variability of the hydraulic parameters and how this influences the model results (Section 2.3.4).

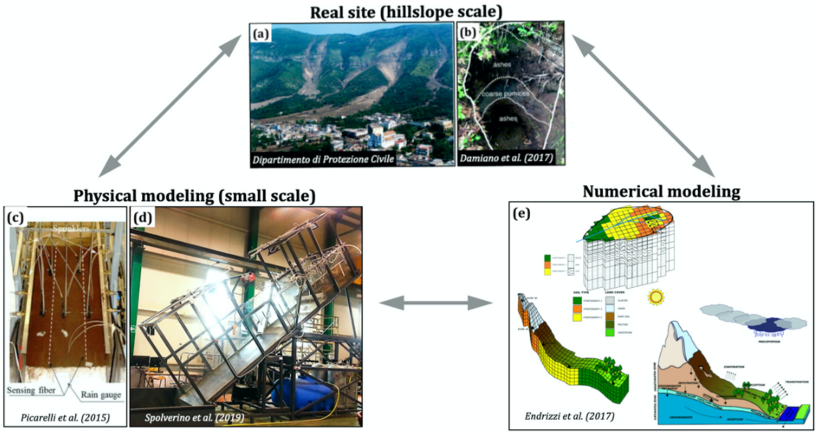

Figure 2. Interdisciplinary approach between real site (a: view of Tuostolo hillslope and Sarno town and b: example of pyroclastic soil stratigraphy), physical modelling (c: flume test and d: metallic structure) and numerical modelling (e).

2.3.1 Hydrological Modeling

The GEOtop (i.e., Bertoldi et al. 2006; Endrizzi et al. 2014; Rigon et al. 2006) hydrological model is a computer-based tool used for simulating and analysing each component of the hydrological cycle. It is designed to solve the highly non-linear coupled energy-water balance system at and below the water surface within a watershed using a vertically varying grid and a fixed integration time. The model considers both surface and subsurface components of the hydrological cycle, allowing for a comprehensive understanding of water flow and storage dynamics. The water budget is formulated through the application of the continuity equation at the surface (1.1) to address surface hillslope flow, and the 3D Richards equation (1.2) to resolve the 3D water flux within variably saturated soils:

$$\frac{\partial q}{\partial t} + c\nabla \cdot q = cq_L \tag{1.1}$$

$$\frac{\partial \theta}{\partial t} + J_w = -S_e \tag{1.2}$$

where q (L/T) is the runoff discharge per unit of area, c (1/T) is the kinematic wave celerity and q_L (L/T) is the unit volume flow exchange with soil (i.e., infiltration and exfiltration), θ (-) is the soil moisture, J_w (L/T) is the unsaturated flow according to Darcy law and S_e (1/T) is a sink term including the exchange between atmosphere and soil. The hydraulic properties of unsaturated soils follow the Mualem (1976) and Van Genuchten (1980) formulation:

$$\theta(\mathrm{h}) = \begin{cases} \theta_r + \frac{\theta_s - \theta_r}{(1+|\alpha \mathrm{h}|)^{1-1/\mathrm{n}}}, h < 0, n > 1 \\ \theta_s, h \geq 0 \end{cases} \tag{2}$$

$$k(S) = k_s\sqrt{S}\left[1 - \left(1 - S^{\frac{n}{n-1}}\right)^{1-1/n}\right]^2, S = \frac{\theta - \theta_r}{\theta_s - \theta_r} \tag{3}$$

with h (kPa) is the soil pressure, θ_r (-) and θ_s (-) are the residual and saturated soil moisture, k (mm/s) and k_s(mm/s) are the unsaturated and saturated hydraulic conductivities, S (-) is the saturation degree, α (1/kPa) is related to the inverse of the air-entry pressure, n (-) is a measure of the pore-size distribution. Eq. 2 is the soil water retention curve (SWRC) and Eq. 3 is the hydraulic conductivity function (HCF). The parameters used in our tests are described in Sections 2.3.2 and 2.3.3.

The energy balance is computed with respect to volumes where the energy content of the water and soil are considered together:

$$\frac{\partial U}{\partial t} + \nabla \cdot g = 0, \quad g = R_n + H + LE \qquad (4)$$

where U (J/m^3) is the internal energy density, g (W/m^2) is the sum of the energy fluxes between soil, vegetation and atmosphere (i.e., R_n is the net radiation, H is the sensible heat and LE is the latent heat). The net radiation is computed as sum of the net shortwave radiation modelled using Iqbal (1983) formula, and the net longwave radiation modelled using the Stefan-Boltzman equation, where the incoming radiation is function of the atmospheric emissivity computed according to Brutsaert (1975a) (as function of air temperature and water vapour pressure) and the upwelling radiation is based on the surface temperature.

The model can be used in high mountain areas with complex terrain considering environmental and topographic variability (Fiddes et al. 2015; Gubler et al. 2013) to estimate a variety of processes including soil water (Bertoldi et al. 2014) and soil temperature distribution (Bertoldi et al. 2010). The radiation budget includes the shadowing of direct solar radiation by surrounding mountains and the effect of topography on diffuse radiation (Endrizzi et al. 2014). The turbulent fluxes of sensible and latent heat are calculated with the flux-gradient relationship (Brutsaert, 1975b; Garratt, 1992) as function of the surface temperature and specific soil moisture between soil and atmosphere, respectively.

The actual evapotranspiration ET (L/T) is computed as sum of three different components (Rigon et al. 2006):

$$ET = (1 - c_f)E + E_v + c_f T \qquad (5)$$

where E is the evaporation from bare soil (Feddes et al. 2001), E_v is the evaporation from the wet vegetation (Deardorff, 1978), T is the transpiration (Best, 1998; Wigmosta et al. 1994), and c_f is the canopy fraction. The model uses a double layer structure to represent the fluxes from the vegetation to the ground surface and vice versa (Endrizzi and Marsh, 2010).

Model input maps include vegetation cover, soil properties and topography, to capture the spatial heterogeneity of the landscape.

Surface parameters related to energy fluxes consist in a single number for each pixel, while subsurface thermodynamic and hydraulic parameters can vary with depth and horizontal extent. Meteorological input data are assigned from weather stations or interpolated from largerscale climate datasets. Model outputs include time varying maps for each soil layer of pore pressure and soil moisture, and maps of water table depth, actual evapotranspiration and surface water. In addition to that, the model can print the time series of pore pressure, soil moisture, temperature for selected points and the discharge at the hillslope outlet.

2.3.2 Application 1

The first application aims to simulate a physical model of the typical Sarno slope (Fig. 1-c) built in the experimental flume test presented in Capparelli et al. (2020) (Fig. S1). Soil samples from buried ashes and pumices (Fig. 1-g) were collected to build the layered flume. The small-scale slope is a 38° layered deposit composed of three soil layers: a 10-cm-thick pumice soil is interbedded between two 20-cm-thick layers of volcanic ash (total depth is 50 cm). The deposit is 270 cm long and 60 cm wide. The initial condition is a dry soil profile with a near hydrostatic pressure distribution. Water can drain out the system downslope with both surface and subsurface flow mechanisms through a perforated panel with gutters. On the other sides (lateral and bottom), the model is confined to achieve impermeable boundaries. The infiltration test consists of a sprinkling experiment with piecewise constant rainfall intensity (R) varying on time:

$$R(t) = \begin{cases} 32\, mm/h, & 0 \leq t \ \leq 151\, min \\ 9\, mm/h, & 151\, min \ < t \ \leq 257\, min \\ 0\, mm/h, & t \ > 257\, min \end{cases}$$

The system is highly instrumented: a high density of small instruments (eight tensiometers and eight TDRs) collected the measurements in time of the main physical quantities (pressure and soil moisture) amidst all soil layers and along the critical areas such as at the surface, the interfaces, the bottom and near the outlet (Fig. 1-c). Two rows of tensiometers are positioned in the upper ash layer: a first series of three tensiometers (T9, T4 and T2) is located 6 cm below the topsoil surface to catch the shallowest layers response, and the second series of three instruments (T10, T3 and T1) is placed at a depth of 18.5 cm directly above the upper ash-pumice interface, each from downstream to upstream. In addition, three TDRs (S8, S7 and S6) are positioned in the same location as the latter tensiometers. In the pumice plane, three TDRs (S5, S4 and S3) are in the middle of the soil at a depth of 25 cm. At the bottom of the small-scale model, one tensiometer (T12) is placed downstream at a depth of 45.5 cm, while the other (T11) is in the middle of the channel at a depth of 48.5 cm. We set up the GEOtop model using a digital elevation model (DEM) with horizontal resolution of 50 mm and vertical grid resolution of 20 mm. A no-flux boundary condition is applied to all lateral sides and at the bottom, except for the downstream outlet where the water can flow out of the system.

Hydraulic parameters mentioned above (Eq. 1) were estimated by fitting the SWRC using tensiometers and TDR measurements. Upper and lower ash parameters are assumed to be the same since they are constructed from the same soil material (Capparelli et al. 2020). The saturated hydraulic conductivity for the ashes is assigned following the experiment results described in Sorbino and Foresta (2002) and Bilotta et al. (2005), where it was estimated in laboratory by performing suction controlled oedometer tests on the undisturbed Tuostolo specimens. For the pumice layer, we apply the hydraulic parameters set provided in De Vita et al. (2013) (Section 2.3.3). The parameters are detailed in Tab. 1, with the corresponding SWRC and HCF sketched in Fig. S2.

2.3.3 Application 2

In this application, the GEOtop model is set up on the Tuostolo hillslope (Fig. 1-d,f). The hillslope, spanning 0.35 km^2, exhibits a north-west aspect orientation and an elevation range from 110 to 814 m. Characterized by slopes averaging between 30° and 38°, with a maximum slope of 62° at 470 m elevation, the area is covered by deciduous forest vegetation. The stratigraphy used in the model is presented in Fig. 1-g. Following Capparelli and Spolverino (2022), we consider an alternating scheme ash-pumice soil layers with progressive depths of 0.45, 0.85, 1.35, 1.65, 1.80, 2.00 and 2.50 m from the surface. The vertical discretization is 50 mm, while the horizontal one corresponds to the available DEM spatial resolution (7 m). No flow lateral boundary conditions are assumed, and water can flow out from the downstream outlet of the reach. A free drainage lower boundary condition is set at the bottom of the 5 m bedrock thickness, as in Napolitano et al. (2016). We used a 3 m water table depth as the initial condition (consistent with other studies, e.g., Tufano et al. 2021) and we use a 3-month period for model spin-up.

	k_s (mm/h)	θ_r (-)	θ_s (-)	α (1/kPa)	n (-)
Lab					
Ashes (upper and lower)	72	0	0.4	0.26	1.29
Pumice	36000	0	0.56	4.2	1.43
Real site					
Ashes (topsoil)	1800	0	0.4	0.36	1.42
Pumices	36000	0	0.56	4.2	1.42
Ashes (buried)	36	0	0.37	0.17	1.4
Bedrock	3	0	0.6	0.37	2

Table 1. Hydraulic parameters used.

The model is executed from 1 October 2007 to 1 October 2009, during which data of precipitation and air temperature have been recorded at hourly time step. The mean precipitation rate is 0.17 mm/h and the highest recorded precipitation peak of 21.4 mm/h occurred at 11:00 PM on 3 January 2009; the cumulative observed precipitation is 2548 mm. The modelled pressure and soil moisture time series are compared with the available observations: one tensiometer located in the topsoil at 0.3 m depth and six TDRs, three located in the topsoil (at 0.1, 0.2 and 0.3 m depth), two located in the pumice layer (at 0.6 and 0.7 m depth), and one located in the buried ashes (at 0.9 m depth).

The SWRC parameters for the ashes (topsoil and buried) were estimated by fitting the SWRC using tensiometers and TDR measurements in the respective layers. The saturated hydraulic conductivity for the ashes (topsoil) is assigned based on the field data analysis presented in Capparelli et al. (2022). The parameters for the ashes (buried) and pumices are assigned according to the experiments described by De Vita et al. (2013) who analysed soils samples in the same study area. Saturated hydraulic conductivities for both layers were estimated through Compact Constant Head Permeameters, while the pumice SWRC parameters were determined using “Temple Cell” equipment. The parameters are detailed in Tab. 1, with the corresponding SWRC and HCF sketched in Fig. S2. For the bedrock layer, we prescribed the Van Genuchten parameters as presented in Capparelli and Versace (2014).

2.3.4 Model performance quantification and uncertainty analysis

The Kling-Gupta efficiency coefficient (KGE, Gupta et al. 2009) is used to quantify the model performance in simulating the spatial and temporal pressure and soil moisture trends in different soil layers. KGE provides a diagnostically interesting decomposition of the Nash-Sutcliffe efficiency, which facilitates the analysis of the relative importance of its different components, namely correlation (r), bias (b) and ratio of variances (a) between measured (M) and simulated (S) values:

$$KGE = 1 - \sqrt{(r-1)^2 + (a-1)^2 + (b-1)^2}, \tag{6}$$
$$r = \frac{cov_{M,S}}{\sigma_M \cdot \sigma_S}, \quad a = \frac{\sigma_S}{\sigma_M}, \quad b = \frac{\mu_S}{\mu_M}$$

where cov denotes the covariance, σ is the standard deviation and μ is the arithmetic mean. KGE values range from (-∞ to 1]: negative and small values indicate poor correlation, 1 indicates perfect correlation.

To evaluate the uncertainty of the hydraulic parameters (Tab. 1), we perform a Monte Carlo simulation analysis based on 500 parameter sets drawn from a lognormal distribution (e.g., Formetta, Capparelli et al. 2016; Formetta, Simoni et al. 2016; Smith and Hebbert, 1979). Accordingly, we assumed θ_r, θ_s, k_s, α and n, as random variables with standard deviation equal to a 10% of the mean values (Tab. 1), for both ashes and pumices, consistently with other studies which used the same method (e.g., Arnone et al. 2016). In this way, we account for the possible uncertainty in the hydrological parameter's estimation.

2.4 Results

2.4.1 Application 1

The model is capable to mimic the evolution of pressure and soil moisture (specifically time of rise and peak values) at all monitored points (Fig. 3), with a mean KGE of 0.84 for the tensiometers and 0.68 for the TDRs. Bold curves in Fig. 3 correspond to the simulation performed with the parameters listed in Tab. 1, while the shaded coloured area is the 95% prediction interval based on the Monte Carlo analysis. The discrepancy between the pressure and soil moisture KGEs can be partially explained by two main reasons. From the model's perspective, uncertainties arise from the SWRC parameters, which may exhibit local differences compared to the undisturbed specimens from which they were estimated, and from the numerical scheme adopted to solve the water balance and handle the hydraulic conductivity at the interface between two highly contrasting soil textures. From the data perspective by the different measurement techniques used for tensiometers and TRDs: while the former measure soil pressure directly at the porous ceramic cap, the latter measure soil moisture in the surrounding soil in an implicit way (e.g., Spolverino et al. 2019) based on measuring the electromagnetic wave time over the probe, which depends on the dielectric constant calculated as a function of the average soil moisture along the device. Thus, unless the instrument is sufficiently small, the TDR readings may also be affected by higher uncertainty, especially at contrasting soil layer interfaces. The tensiometers placed at 6 cm depth (i.e., T2, T4 and T9) in the upper ashes show an immediate increase in pressure after 15 min from the start of the rainfall.

The pressure increases from the extremely dry initial condition of -50 kPa to approximately -10 kPa in the first 30 min of the experiment. In the following hours, the pressure continues to rise to nearly 0 kPa without reaching full saturation at the end of the highest rainfall intensity. During the low intensity rainfall, the pressure sets around -2 kPa after an initial small decrease. At the end of the experiment, both simulated and observed curves show similar pressure values and a slight drainage (decrease in pressure) when rainfall is stopped. The tensiometers located at 18.5 cm depth (i.e., T1, T3 and T10), above the upper ash-pumice interface, show a nearly perfect overlap between measured and simulated values with a mean KGE of 0.90. The pressure dynamics is well captured by the model, with the tensiometer T1 rising being slightly delayed in the first phase of the experiment (32 mm/h rainfall intensity). Pressure rises from initial dry state of -45 kPa, to a wet state close to saturation. During low rainfall intensity, these tensiometers show the same behaviour as the previous set. Last, in the lower ash tensiometers (i.e., T11 and T12), the simulated pressure increases after 4 h, consistently with the records, from -30 to -10 kPa, with an underestimation for the tensiometer in the centre of the flume and at the outlet (i.e., T11 and T12).

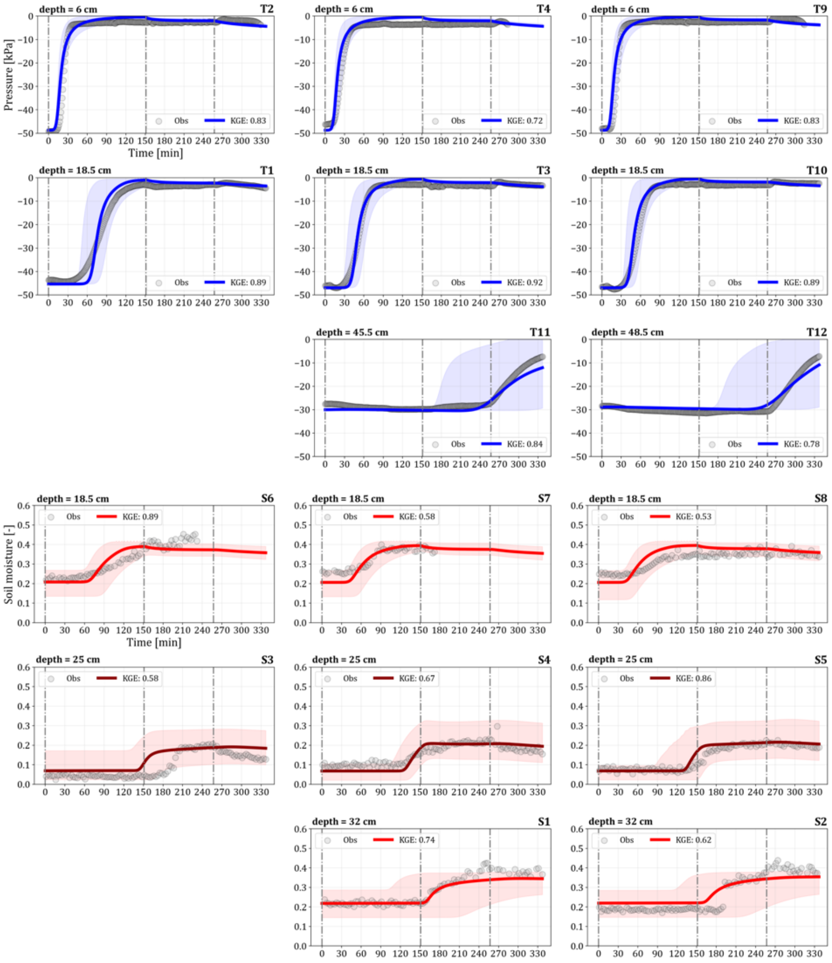

Figure 3. Application 1 results. Comparison between pressure measurements (grey dots) and simulated values (blue lines) for different tensiometers located in the upper and lower ashes, with relative Kling-Gupta efficiency (KGE). Comparison between soil moisture measurements (grey dots) and simulated values (red lines), with relative KGE. Red lines correspond to ashy layers, while dark red lines correspond to the pumice layer. The red and blue shaded coloured areas are the 95% prediction interval of the Monte Carlo analysis. The dashed vertical lines represent the moments when rainfall intensity changes.

The shallowest TDRs (i.e., S6, S7 and S8) response follows that of the tensiometers placed in the same position: we observe an increase in soil moisture at the upper interface in correspondence of the rising pressure after 60 min in T1 and 30 min in T3 and T10. The model predicts an initial drier condition of 0.20, which is more evident in S7 and S8, with respect to the observed soil moisture around 0.25. The soil moisture in the topsoil nearly reaches the saturation value θ_S=0.40 at the end of the 32 mm/h intensity rainfall. The modelled soil moisture levels in the pumice layer (i.e., S3, S4 and S5) reproduce the observed pattern, with one exception for the initial condition of the last two instruments and an anticipated rising for S3. The initial soil moisture is near the residual soil moisture θ_r=0, and the wetting phase begins around 125 min until the coarse layer reaches a peak value of 0.20, far below the soil moisture at saturation θ_S=0.56, implying that water is either stored in the finer upper layer or flows into the bottom layer. In the deepest TDRs (i.e., S1 and S2), the pattern is well captured for the first one, and for the second one, the increase in soil moisture exhibits a time discrepancy of 30 min when compared with observations. Additionally, the model predicts lower soil moisture values (0.35) at the end of sprinkling experiment compared with the data.

The pore water pressure prediction interval (Fig. 3) is restrained to around ±5kPa in magnitude and few minutes in time when considering the tensiometer at 6 cm depth (i.e., T2, T4 and T9) and to around ±10 kPa and few minutes for the tensiometer close to the interface (i.e., T3 and T10), with the exception of T1 for which the error can be larger (up to ±20 kPa and 30 min). Conversely, when we consider the bottom tensiometers (i.e., T11 and T12), the error can be quite large: the pressure rising in the lower ashes can be either anticipated or delayed by over 1 h. The uncertainty in the TDR measurements is evident in both the timing and magnitude of soil moisture (±0.10) across all layers. Deeper devices experience more significant errors, leading to a 30 min anticipation or delay and an overestimation of soil moisture ($\theta > 0.30$) in the pumice layer, as well as a 60 min delay in the lower ashes.

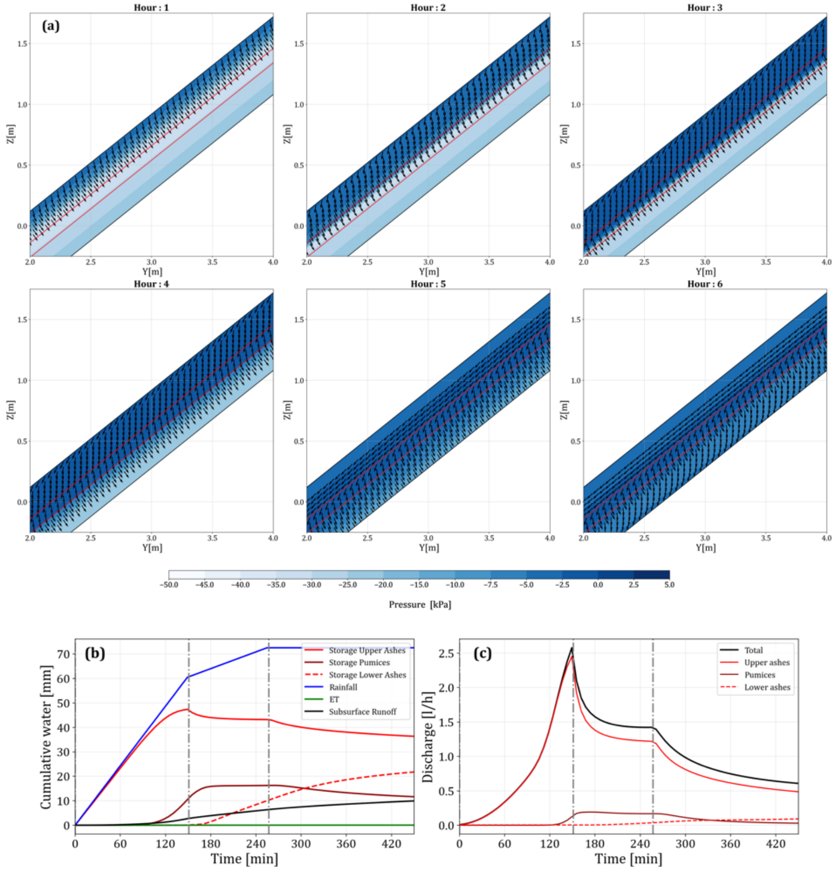

Figure 4. Application 1 results. (a) Normalized flux vectors and pressure distribution for a centered cross section at different hours. Red lines correspond to the ash-pumice interfaces. (b) Water balance for the flume and (c) lateral subsurface runoff subdivision across the three layers. The dashed vertical lines in (b, c) represent the moments when rainfall intensity changes.

The objective of this first application was not only to replicate the laboratory observations but also to verify that the model can reproduce the infiltration processes regarding subsurface water flow in the volcanoclastic layered deposit.

Fig. 4-a shows the orientation of the normalized flux vectors (with respect to the flux magnitude) and the pressure evolution with the propagation of the wetting front at different time steps for a cross section located at the centre of the flume. At the beginning of the experiment, the fluxes are slope normal in correspondence with the wetting front, as seen in Lu et al. 2011 for a homogeneous slope: the

main contribution to the water flow direction is capillary. After 2 h, the wetting front reaches the first interface. The pressure in the topsoil is constant and the vectors are moving from a normal to a vertical direction thanks to the increasing effect of the gravity. After 3 h, the wetting front arrives at the bottom of the pumice layer. The accumulation of water at the interface is responsible for the rise of the water level in the upper ash, however, saturation is not reached. The fluxes are gaining a non-negligible horizontal component, which is more evident close to the first interface due to a redirection of flow downstream in the channel. After 4 h, infiltration process also develops in the lowest layer (orthogonal fluxes). After 5 h, the water level decreases in the upper ashes and the flux orientation are almost slope parallel, while in the pumice and lower ashes, infiltration is still ongoing. At the last time step, after 6 h, the flux directions in the topsoil are slope parallel, that is, the soil is draining, while the accumulated water in the lower ashes is flowing downslope along the impermeable bottom.

Fig. 4-b illustrates the water balance for the flume test in terms of the specific cumulated volume from the start of the experiment. Most of the infiltration water is retained in the first layer of the soil during the initial phase of the experiment, reaching a maximum level of 47 mm at the end of the high-intensity rainfall. Subsequently, storage in the pumices begins to increase after 90 min. During low intensity rainfall, the storage in the upper ashes layer gradually decreases to 43 mm due to lateral runoff and infiltration towards the pumice layer itself, reaching a plateau of 16 mm. Only after 3 h from the beginning of the experiment, the storage in the lower ashes starts to increase reaching a maximum of 22 mm. The evaporation from the bare soil surface constitutes only a small fraction of the water balance.

The cumulated lateral subsurface runoff, computed at the downstream face of the flume, considers contributions from all soil layers (Fig. 4-c). The upper ashes make the most significant contribution to subsurface runoff. The peak discharge of 2.5 L/h in the uppermost soil is observed at the end of the high-intensity rainfall, decreasing up to 1.44 L/h in the second phase and further diminishing in the last drainage phase when rainfall ceases. The pumice contributes only 12% to the subsurface water flow, with a maximum computed discharge of 0.19 L/h after 150 min. Runoff from the lower ashes develops at the base of the flume only after water begins to flow along the bottom.

2.4.2 Application 2

Fig. 5 shows the comparison between observed and modelled time series of the hydrological variables of the real site. The model mimics the pressure observed by the tensiometer at 0.3m depth (i.e., TENSIO3) quite well, with a KGE of 0.83. During the rainy season, pressure values are consistently negative, around -10 kPa, with fluctuations in accordance with storm peaks. During the dry season, pressure decreases to its lowest values. Owing to the absence of precipitation and the prevailing evapotranspiration, the soil becomes dry (pressure ~-50 kPa). We overestimate pressure values in late May-June 2008 and 2009 during dry weeks with no precipitation events.

The topmost TDR, named TDR1, is located at a depth of 0.1 m in the upper ashes. The soil moisture dynamics is consistent with the observed trend in both simulated years. During summer, we observe a constant decrease in soil moisture, implying that the topsoil is draining and evaporating; in contrast, in fall, winter, and spring, soil moisture fluctuations appear in correspondence of the rainstorm events. The topsoil never reaches saturation: the maximum soil moisture values of ~0.3 are below the saturated soil moisture of 0.4. TDR2 and TDR3 show similar behaviour as the previous one, with the same pattern but slightly lower peak values. At these depths, agreement with observations is higher, even for the drier periods, with an overall KGE of 0.80 for the first probe and 0.71 for the second one. TDR6 and TDR7 give an insight into the upper pumice layer. The average soil moisture of 0.07 is far below the saturation value of 0.56, that is, the pumice layer remains very dry during the simulation.

The fluctuations in the coarse layer are less pronounced than in the upper finer layer. In December 2008-January 2009, the model simulates two peaks around 0.2, but even in this case, the soil is only 33% saturated. In general, the pumice layer is less saturated than the ashy topsoil, meaning that most of the water percolating in the soil is stored in the top layer or drains to the deeper horizons. The temporal pattern is well captured by the model, but during storms, it simulates slightly higher peaks in correspondence of more flat records. The TDR placed in the lower ashes (i.e., TDR9) at 0.9 m depth exhibits small changes in

soil moisture values around 0.25. During the wet season, the model predicts fluctuations during the most intense storms, differently from the uppermost devices (TDR1, TDR2 and TDR3) where the response to precipitation events is quicker and pronounced. During the wet season, we do not observe significant fluctuations in the buried ashes as compared to the upper ashes. At greater depths, the behaviour of the finer soil is likely to be influenced by a seasonal trend rather than a single rainstorm.
The pressure prediction interval in Fig. 5 is wider during the dry season in the descending phase when the pressure decreases, while the TDR one shows a consistent overestimation (underestimation) of the soil moisture during all the years in all layers. Small changes in the SWRC parameter values can either increase (decrease) the soil moisture by over 50%. As observed in the first application, larger differences in the model outputs occur in the deeper layers.

Fig. 6 displays the pressure maps above each soil interface at the five different time steps annotated in Fig. 5. The first row shows the pressure layers on 9th January 2008. At this time, a vertical and horizontal difference in pressure distribution is remarkable: rainfall from the previous months accumulated in the middle layers and especially along the concave areas. In contrast, the topsoil shows an almost uniform pressure distribution along the hillslope, determined by the precipitation of the day. During the summer (2nd July 2008), the uppermost and deepest layers show lower values of pressure in contrast to the middle layers. Most of the water is stored in the intervening horizons, while the uppermost soil hydrological processes are dominated by evapotranspiration. During the prolonged storms of 29th November 2008, the hillslope shows a uniform pressure distribution both along the profile and in the plain. The predicted pressure reaches its highest values between -5 and -2.5 kPa, but no positive values are observed. In spring, on 28th April 2009, the pressure field at different depths is similar to that observed January: in the upper layers, the waterfront infiltrates and the water is stored in concave areas and channels, while in the deeper layers, the water flows downhill or infiltrates towards the bedrock. The last time level, dated 6th August 2009, shows the most critical situation in terms of water stress during the summer due to the prolonged dry period.

Fig. S3 shows the daily actual evapotranspiration flux. Results show the typical seasonal trend with the maximum evapotranspirated water of around 4 mm/day during the summer and the minimum during the winter.

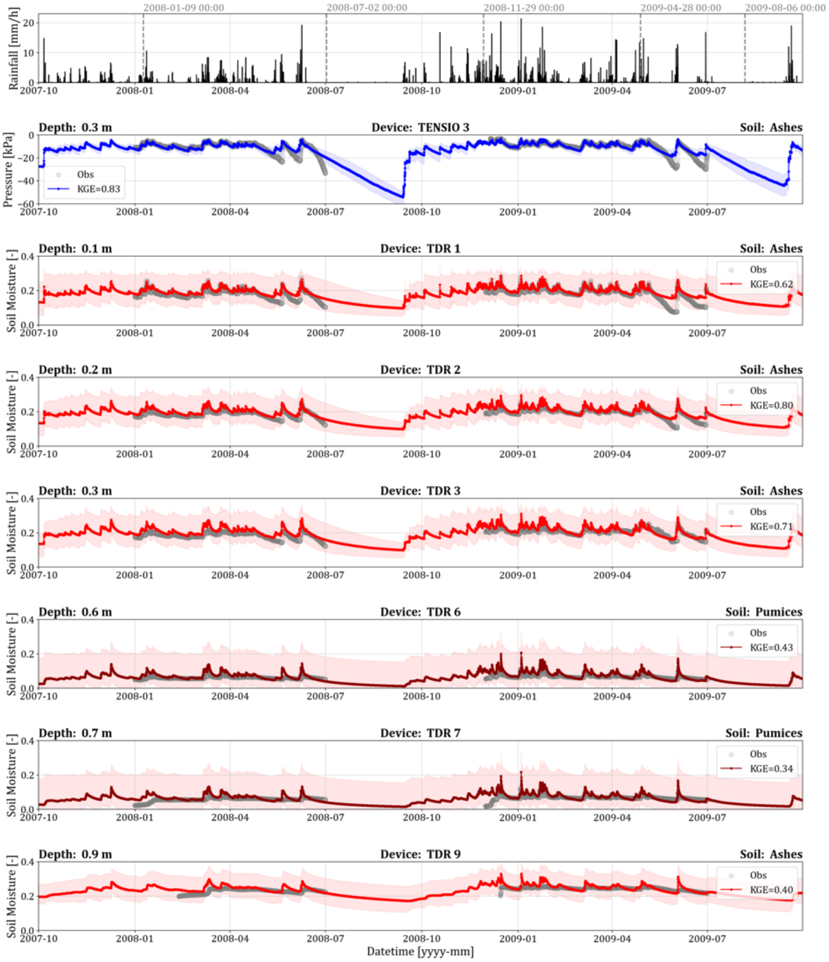

Figure 5. Application 2 results. Starting from the top, observed rainfall, the vertical grey dashed lines refer the dates at which the pressure maps are presented. Comparison between observed (grey dots) and modeled (blue line) pressure in the topsoil tensiometer, with relative Kling-Gupta efficiency (KGE). Comparison between observed (grey dots) and simulated (red lines) soil moisture for at different depths and layers, with relative KGE. Red lines correspond to ashy layers, while dark red lines correspond to the pumice layer. The red and blue shaded coloured areas are the 95% prediction interval of the Monte Carlo analysis.

2.5 Discussion

2.5.1 Hydrological responses of layered pyroclastic soils

The two applications provide in-depth insights into hydrological processes in unsaturated layered pyroclastic soils, emphasizing the importance of considering multiple scales and multi-data point measurements for a comprehensive understanding.

Previous research by Olivares and Damiano (2007), Damiano and Olivares (2010) and Spolverino et al. (2019) conducted flume tests on homogeneous fine ash slopes during transient rainfall, revealing the presence of a water table at the bottom. In contrast, studies by Damiano and Olivares (2010), Damiano et al. (2017) and Damiano (2019) investigated small-scale layered slopes with a layer of coarse pumice between two fine ash soils. In our study, we build upon this work by extending the model validation/assessment to include measured soil moisture time-series across all soil layers, with a specific focus on the intervening pumice layer's role in regulating water storage, infiltration dynamics and soil response to precipitation across different spatial and temporal scales.

Pumices, characterized by high porosity and permeability, exert significant capillary forces due to their irregular surface structure and interconnected pore spaces. When dry, these pumice layers hinder water infiltration into underlying layers (e.g., Capparelli and Spolverino, 2022; Mancarella et al. 2012; Mancarella and Simeone, 2012), resulting in water accumulation within the finer ash layer above, affecting soil cover stability and promoting lateral flow along the upper interface. Despite the pumice layer exhibiting a saturated hydraulic conductivity two orders of magnitude higher than ash layers, the wetting front progression within pumices is slower compared to ashes (Fig. 3 and 4). This phenomenon can be explained through hydraulic conductivity curves, indicating that at pressure values near saturation, pumice demonstrates greater unsaturated hydraulic conductivity than ashes. However, once a specific pressure threshold is reached (-2.5 kPa), ash conductivity surpasses that of pumices by orders of magnitude (Fig. S2-b). Once a sufficiently high gradient is established across the interface, the vertical water flow proceeds to deeper depths. This situation depends on two factors: the initial soil moisture condition and the duration/intensity of the storm.

A sensitivity analysis using GEOtop was conducted to assess the impact of variable duration-intensity rainfalls, revealing distinct responses. We considered two opposite scenarios: (i) a high intensity/ short duration rainfall, that is, 100 mm/h lasting for 30 min, and (ii) a medium-low intensity/long duration rainfall, that is, 30 mm/h lasting for 5 h. Results are presented in Fig. S4. During the first test (Fig. S4-a,b), the dry pumices confine the infiltrated water to the upper ashes, resulting in subsurface parallel flow along the upper interface due to the established enhanced slope parallel hydraulic gradient. After the event, once the capillary barrier is breached, water begins to infiltrate into the pumice layer. In contrast, for the second rainfall test (Fig. S4-c,d), the infiltrated water can reach the deeper layers. The water accumulated in the pumices and lower ashes significantly contributes to the total discharge. The storage in the bottom layer is high and comparable with that in the first layer. In this scenario, the uniform pressure condition along the soil depth and the potential development of a water table at the base of the flume are likely responsible for the instability of the entire flume.

In the real site application, the prolonged dry or wet periods influence the initial conditions from which the short-term response of the soil cover evolves during individual events (e.g., Comegna et al. 2016; Fusco et al. 2017). During a rainstorm at the beginning of the rainy season (September-October), when the soil profile is dry, the intervening pumice capillary barrier effect prevents infiltration from penetrating deeper layers, resulting in water accumulation and lateral flow in the upper layers. In this case, the cause of the landslide trigger mechanism is the reduction of strength in the shallowest layers as highlighted by Capparelli and Versace (2014). During winter and spring seasons (November-June), when the pressure profile is very smooth and close to saturation due to the frequent rainstorms, the barrier established by the pumices disappears and infiltration prevails over lateral flow. Therefore, rain-triggered landslides in Campanian pyroclastic soils occur mainly at the end of winter or early spring (i.e., Sarno 5th May 1998, Cervinara 15th December 1999), when the soil profile is wet and close to saturation (Fig. 6; November-April). The arid hydrological condition prevailing at the end of summer strongly inhibits slope instability under most precipitation conditions (e.g., Napolitano et al. 2016).

Another factor influencing slope instability is the site morphology. The 3-D GEOtop hydrological model allows treatment of complex surface and bedrock topographies, with a particular focus on convergent sites where headwaters are formed by the accumulation of groundwater (subsurface flow and seepage) and surface water in channels, or divergent sites where water flow spreads. Water can accumulate in colluvial depressions, raising the water table and increasing pressure head (Fig. 6; buried layers). This intricate interaction of terrain features and water distribution across multiple dimensions can significantly impact the stability of slopes, especially in scenarios involving multiple soil layers, as more layers are involved in the stability dynamics than in planar or simpler morphologies. (e.g., Formetta and Capparelli, 2019; Formetta, Capparelli et al. 2016; Formetta, Simoni et al. 2016).

Consistently with the approach used in previous studies (e.g., Arnone et al. 2016; Dai and Lee, 2002; Formetta, Capparelli et al. 2016; Formetta, Simoni et al. 2016), we explored the influence of model parameters uncertainty on hydrological predictions by describing their distributions using mean values and standard deviations, computed as percentage of the mean. Results show that in some cases, model predictions highly depend on these values, and therefore, proper quantification of parameters, such as mean values and standard deviation, is crucial. In particular cases (i.e., for the pumices and bottom ashes in Fig. 3 and 5), accounting for a variance of only 10% of the mean parameter values may result in very spread model predictions. For our test site, this can be partially attributed to (i) the non-linearity of the SWRC and (ii) the stratified setting of soil layers, which control the retention behaviour and the temporal delay in the wetting front propagation.

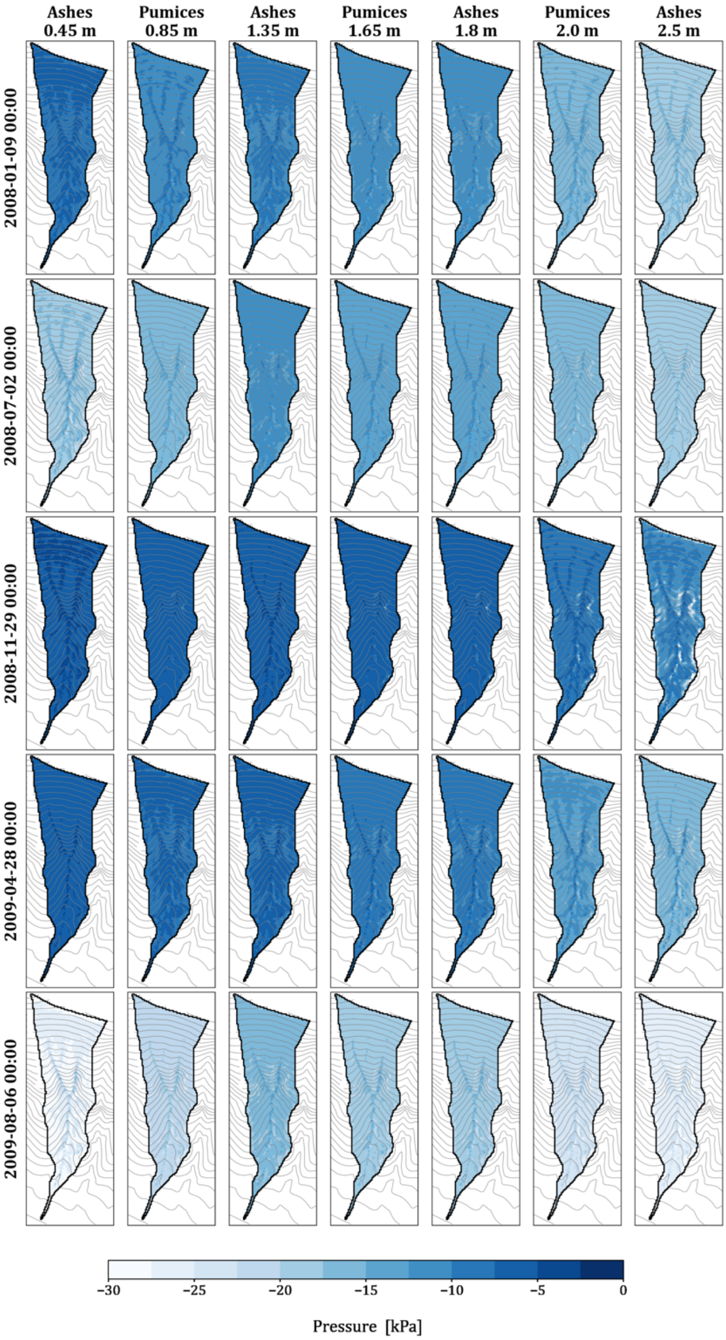

Figure 6. Application 2 results. Pressure layer maps above each soil interface. Maps are shown moving to the right with increasing depth and moving down with increasing time.

2.5.2 Limitations

For the Application 1, the monitoring network allows an exhaustive comprehension of the hydrological response to rainfall infiltration on the layered slope, being the tensiometers and TDRs buried at different depths in different positions along the slope. However, no tensiometers were installed in the pumices because of technical issues in measuring soil water pressure. As pointed out in Capparelli and Spolverino (2020), it was not possible to establish the necessary hydraulic contact between the coarse gravelled soil and the tensiometer cap. This results as a limiting factor to understand the pressure evolution occurring in the pumice layer.

For the Application 2, only one monitoring station was active near the ridge of the Tuostolo hillslope and has been used to verify the hydrological model accuracy. Although 2 years' worth of hourly records of pore water pressure and soil moisture at various depths are present, the inclusion of additional monitoring stations across the hillslope could have improved understanding of hydrological processes at the hillslope scale, beyond assessing the robustness of the numerical model. Furthermore, the hypothesis used in the model of parallel layers with different soil properties for the entire analysed hillslope could be relaxed if spatial measurements of soil layer thicknesses were available in multiple points. Despite this limitation, the topographic gradient is shown playing a major role in water accumulation ad subsurface flow redistribution.

Due to the lack of subsurface flux measurements in the laboratory application, discharge records at the actual site, and evapotranspiration data, predicting the water balance becomes challenging. To address this, we conducted simulations of various rainfall scenarios to understand potential responses of all the pyroclastic layers in terms of water storage dynamics and subsurface runoff generation.

2.6 Conclusions

In this study, we reproduced the hydrological behaviour of layered pyroclastic soils through numerical simulations. Differently from previous studies, we validated a 3D hydrological model using both pressure and soil moisture measurements in multiple locations and depths for two applications, highly different for spatial and temporal scales.

In the first application, we simulated a laboratory physical model of a steep layered slope made of soil samples recovered from the Tuostolo site. In the second test, we simulated the real hillslope during 2 years of recorded precipitation. In both applications, a congruence with measured data was found for all instruments and all hydrological variables. The Tuostolo hillslope results show that it is possible extend the modelling analysis at nearby non-instrumented sites, where (i) the assumption of similar stratigraphy and composition of the volcanic material is valid or (ii) at site estimations of soil parameters are available. The modelling framework allowed not only to make predictions of soil moisture and pressure values but also to account for model parameters uncertainty through Monte Carlo simulations.

In the flume test, we demonstrated the physical role of the intervening coarse layer: dry pumice initially impedes infiltration, inducing a lateral flow diversion and accumulating water in the upper ash. Once a sufficiently high hydraulic gradient is established across the upper interface, the wetting front can propagate to deeper depths. This effect depends on the intensity and duration of applied rainfall. Flow pattern was reconstructed by analysing the flux vectors high temporal resolution all over the domain. In the real site test, we demonstrated the ability to simulate the observed seasonal variations in pressure and soil moisture response over extended rainfall periods and individual storms across multiple locations, including both shallow and deep depths, despite the presence of contrasting soil layers.

Pressure dynamic in the uppermost layer depends on individual storms, while the response in the deepest layers is less pronounced and depends on the antecedent weekly-monthly precipitation history. The spatial distribution of pressure is heavily influenced by hillslope topography, that is, water accumulates in hollows that are susceptible to landslide events during winter and spring, when soil is wetter and uniform pressure profile develops along the soil depth. This has been presented showing dynamic in time 3D evolution of the pressure field over the hillslope.

The importance of this research lies not only in numerically simulating soil water flow dynamics through pyroclastic soils but also in transferring the concepts learned from small scale to large scale within a consistent, adaptable and physically based framework. This can be useful for further understanding complex hydrological processes and natural hazard assessments like EWS for landslides. For example, result of such 3D water flow models could be combined with geophysical models to evaluate hillslope mechanical stability.

Acknowledgments

We thank Doctor Eng. G. Spolverino for sharing all the hydrological records. Giuseppe Formetta is partially supported by the PRINN COACH-WAT (CODE 2022FXJ3NN CUP E53D23004390001). Open access publishing facilitated by Università degli Studi di Trento, as part of the Wiley - CRUI-CARE agreement.

Data availability statement

The software used in this paper is open-source and available at https://github.com/geotopmodel/geotop. The simulation results are available for both cases studied on Zenodo at https://zenodo.org/record/8424961 or upon reasonable request to the corresponding author.

References

Arnone, E., Dialynas, Y. G., Noto, L. V., and Bras, R. L. (2016). Accounting for soil parameter uncertainty in a physically based and distributed approach for rainfall-triggered landslides. Hydrological Processes, 30 (6), 927-944.

Basile, A., Mele, G., and Terribile, F. (2003). Soil hydraulic behaviour of a selected benchmark soil involved in the landslide of Sarno 1998. Geoderma, 117, 331-346.

Baum, R. L., Godt, J. W., and Savage, W. Z. (2010). Estimating the timing and location of shallow rainfall-induced landslides using a model for transient, unsaturated infiltration. Journal of Geophysical Research, 115, F03013.

Bertoldi, G., Della Chiesa, S., Notarnicola, C., Pasolli, L., Niedrist, G., and Tappeiner, U. (2014). Estimation of soil moisture patterns in mountain grasslands by means of SAR RADARSAT2 images and hydrological modeling. Journal of Hydrology, 516, 245-257.

Bertoldi, G., Notarnicola, C., Leitinger, G., Endrizzi, S., Zebisch, M., Della Chiesa, S., and Tappeiner, U. (2010). Topographical and ecohydrological controls on land surface temperature in an alpine catchment. Ecohydrology, 3, 189-204.

Bertoldi, G., Rigon, R., and Over, T. M. (2006). Impact of watershed geomorphic characteristics on the energy and water budgets. Journal of Hydrometeorology, 7 (3), 389-403.

Best, M. J. (1998). A model to predict surface temperatures. BoundaryLayer Meteorology, 88 (2), 279-306.

Bilotta, E., Cascini, L., Foresta, V., and Sorbino, G. (2005). Geotechnical characterisation of pyroclastic soils involved in huge flowslides. Geotechnical and Geological Engineering, 23, 365-402.

Brutsaert, W. (1975a). On a derivable formula for long-wave radiation from clear skies. Water Resources Research, 11, 742-744.

Brutsaert, W. (1975b). A theory for local evaporation (or heat transfer) from rough and smooth surfaces at ground level. Water Resources Research, 11, 543-550.

Capparelli, G., Damiano, E., Greco, R., Olivares, L., and Spolverino, G. (2020). Physical modelling investigation of rainfall infiltration in steep layered volcanoclastic slope. Journal of Hydrology, 580, 124199.

Capparelli, G., and Spolverino, G. (2020). An empirical approach for modeling hysteresis behavior of pyroclastic soils. Hydrology, 7, 14.

Capparelli, G., and Spolverino, G. (2022). Hydrological monitoring of a slope covered by stratified pyroclastic deposits and analysis of infiltration processes. Hydrological Processes, 36 (6), e14634.

Capparelli, G., and Versace, P. (2014). Analysis of landslide triggering conditions in the Sarno area using a physically based model. Hydrology and Earth System Sciences, 18, 3225-3237.

Cascini, L. (2004). The flowslide of May 1998 in the Campania region, Italy: Scientific emergency management. Rivista italiana di geotecnica, 2, 11-44.

Cascini, L., Cuomo, S., and Guida, D. (2008). Typical source areas of May 1998 flow-like mass movements in the Campania region, Southern Italy. Engineering Geology, 96, 107-125.

Cascini, L., Sorbino, G., Cuomo, S., and Ferlisi, S. (2014). Seasonal effects of rainfall on the shallow pyroclastic deposits of the Campania region (southern Italy). Landslides, 11, 779-792.

Comegna, L., Damiano, E., Greco, R., Guida, A., Olivares, L., and Picarelli, L. (2016). Field hydrological monitoring of a sloping shallow pyroclastic deposit. Canadian Geotechnical Journal, 53, 1125-1137.

Costanzo, S., Di Massa, G., Costanzo, A., Morrone, L., Raffo, A., Spadafora, A., Borgia, A., Formetta, G., Capparelli, G., and Versace, P. (2015). Low-cost radars integrated into a landslide early warning system. Advances in Intelligent Systems and Computing, 354, 11-19.

Crosta, G. B., and Dal Negro, P. (2003). Observations and modelling of soil slip-debris flow initiation processes in pyroclastic deposits: The Sarno 1998 event. Natural Hazards and Earth System Sciences, 3, 53-69.

Dai, F. C., and Lee, C. F. (2002). Landslide characteristics and slope instability modeling using GIS, Lantau Island, Hong Kong. Geomorphology, 42 (34), 213-228.

Damiano, E. (2019). Effects of layering on triggering mechanisms of rainfall-induced landslides in unsaturated pyroclastic granular soils. Canadian Geotechnical Journal, 56, 1278-1290.

Damiano, E., Greco, R., Guida, A., Olivares, L., and Picarelli, L. (2017). Investigation on rainwater infiltration into layered shallow covers in pyroclastic soils and its effect on slope stability. Engineering Geology, 220, 208-218.

Damiano, E., and Olivares, L. (2010). The role of infiltration processes in steep slope stability of pyroclastic granular soils: Laboratory and numerical investigation. Natural Hazards, 52, 329-350.

Damiano, E., Olivares, L., and Picarelli, L. (2012). Steep-slope monitoring in unsaturated pyroclastic soils. Engineering Geology, 137-138, 1-12.

De Vita, P., Fusco, F., Tufano, R., and Cusano, D. (2018). Seasonal and event-based hydrological and slope stability modeling of pyroclastic fall deposits covering slopes in Campania (southern Italy). Water, 10, 1140.

De Vita, P., Napolitano, N., Godt, J., and Baum, R. (2013). Deterministic estimation of hydrological thresholds for shallow landslide initiation and slope stability models: Case study from the Somma-Vesuvius area of southern Italy. Landslides, 10, 713-728.

Deardorff, J. W. (1978). Efficient prediction of ground surface temperature and moisture, with inclusion of a layer of vegetation. Journal of Geophysical Research, 83 (C4), 1889-1903.

Emberson, R., Kirschbaum, D., and Stanley, T. (2020). New global characterisation of landslide exposure. Natural Hazards and Earth System Sciences, 20, 3413-3424.

Endrizzi, S., Gruber, S., Dall'Amico, M., and Rigon, R. (2014). GEOtop 2.0: Simulating the combined energy and water balance at and below the land surface accounting for soil freezing, snow cover and terrain effects. Geoscientific Model Development, 7, 2831-2857.

Endrizzi, S., Matteo Dall'Amico, M., Stephan Gruber, S., and Riccardo Rigon, R. (2017). GEOtop Users Manual. https://geotopmodel.github.io/geotop/materials/geotop_manuale.pdf

Endrizzi, S., and Marsh, P. (2010). Observations and modeling of turbulent fluxes during melt at the shrub-tundra transition zone 1: Point scale variations. Hydrology Research, 41, 471-491.

Feddes, R. A., Hoff, H., Bruen, M., Dawson, T., de Rosnay, P., Dirmeyer, P., and Pitman, A. J. (2001). Modeling root water uptake in hydrological and climate models. Bulletin of the American Meteorological Society, 82 (12), 2797-2809.

Fiddes, J., Endrizzi, S., and Gruber, S. (2015). Large-area land surface simulations in heterogeneous terrain driven by global datasets: Application to mountain permafrost. The Cryosphere, 9, 411-426.

Formetta, G., and Capparelli, G. (2019). Quantifying the three-dimensional effects of anisotropic soil horizons on hillslope hydrology and stability. Journal of Hydrology, 570, 329-342.

Formetta, G., Capparelli, G., and Versace, P. (2016). Evaluating performance of simplified physically based models for shallow landslide susceptibility. Hydrology and Earth System Sciences, 20, 4585-4603.

Formetta, G., Simoni, S., Godt, J. W., Lu, N., and Rigon, R. (2016). Geomorphological control on variably saturated hillslope hydrology and slope instability. Water Resources Research, 52, 4590-4607.

Fusco, F., Alloca, V., and De Vita, P. (2017). Hydro-geomorphological modelling of ash-fall pyroclastic soils for debris flow initiation and groundwater recharge in Campania (southern Italy). Catena, 158, 235-249.

Garratt, J. R. (1992). The atmospheric boundary layer (p. 316). Cambridge University Press.

Greco, R., Comegna, L., Damiano, E., Guida, A., Olivares, L., and Picarelli, L. (2013). Hydrological modelling of a slope covered with shallow pyroclastic deposits from field monitoring data. Hydrology and Earth System Sciences, 17, 4001-4013.

Greco, R., Marino, P., and Bogaard, T. A. (2023). Recent advancements of landslide hydrology. Wiley Interdisciplinary Reviews Water, 10 (6), e1675.

Gubler, S., Endrizzi, S., Gruber, S., and Purves, R. S. (2013). Sensitivities and uncertainties of modeled ground temperatures in mountain environments. Geoscientific Model Development, 6 (4), 1319-1336.

Gupta, H. V., Kling, H., Yilmaz, K. K., and Martinez, G. F. (2009). Decomposition of the mean squared error and NSE performance criteria: Implications for improving hydrological modelling. Journal of Hydrology, 377 (1-2), 80-91.

Hübner, R., Günther, T., Heller, K., Noell, U., and Kleber, A. (2017). Impacts of a capillary barrier on infiltration and subsurface stormflow in layered slope deposits monitored with 3-D ERT and hydrometric measurements. Hydrology and Earth System Sciences, 21 (10), 5181-5199.

Hungr, O., Evans, S., and G., Bovis, M. (2001). Review of the classification of landslides of the flow type. Environmental and Engineering Geoscience, 7, 221-238.

Iqbal, M. (1983). An introduction to solar radiation. Academic Press, 390, 1-390.

Lu, N., Kaya, B. S., and Godt, J. W. (2011). Direction of unsaturated flow in a homogeneous and isotropic hillslope. Water Resources Research, 47, W02519.

Mancarella, D., Doglioni, A., and Simeone, V. (2012). On capillary barrier effects and debris slide triggering in unsaturated layered covers. Engineering Geology, 147-148, 14-27.

Mancarella, D., and Simeone, V. (2012). Capillary barrier effects in unsaturated layered soils, with special reference to the pyroclastic veneer of the Pizzo d'Alvano, Campania, Italy. Bulletin of Engineering Geology and the Environment, 71, 791-801.

Mualem, Y. (1976). A new model predicting the hydraulic conductivity of unsaturated porous media. Water Resources Research, 12, 513-522.

Napolitano, E., Fusco, F., Baum, R. L., Godt, J. W., and De Vita, P. (2016). Effect of antecedent-hydrological conditions on rainfall triggering of debris flows in ash-fall pyroclastic mantled slopes of Campania (southern Italy). Landslides, 13, 967-983.

Olivares, L., and Damiano, E. (2007). Postfailure mechanics of landslides: Laboratory investigation of flowslides in Py-roclastic soils. Journal of Geotechnical and Geoenviromental Engineering, 133, 51-62.

Olivares, L., and Picarelli, L. (2003). Shallow flowslides triggered by intense rainfalls on natural slopes covered by loose unsaturated pyroclastic soils. Geotechnique, 53 (2), 283-287.

Picarelli, L., Damiano, E., Greco, R., Minardo, A., Olivares, L., and Zeni, L. (2015). Performance of slope behavior indicators in unsaturated pyroclastic soils. Journal of Mountain Science, 12 (6), 1434-1447.

Picarelli, L., Evangelista, A., Rolandi, G., Paone, A., Nicotera, M. V., Olivares, L., and Rolandi, M. (2006). Mechanical properties of pyroclastic soils in campania region. In proceedings of the 2nd international workshop on characterisation and engineering properties of natural soils, Singapore.

Rigon, R., Bertoldi, G., and Over, T. M. (2006). GEOtop: A distributed hydrological model with coupled water and energy budgets. Journal of Hydrometeorology, 7 (3), 371-388.

Roman Quintero, D. C., Damiano, E., Olivares, L., and Greco, R. (2024). Mechanical and hydraulic properties of unsaturated layered pyroclastic ashes in landslide-prone areas of Campania (Italy). Bulletin of Engineering Geology and the Environment, 83 (7), 291.

Smith, R. E., and Hebbert, R. H. B. (1979). A Monte Carlo analysis of the hydrologic effects of spatial variability of infiltration. Water Resources Research, 15, 419-429.

Sorbino, G., and Foresta, V. (2002). Unsaturated hydraulic characteristics of pyroclastic soils. Proceeding of the 3rd international conference on unsaturated soils, Recife, Balkema, Rotter-dam. 1, 405-410.

Sorbino, G., Sica, C., and Cascini, L. (2010). Susceptibility analysis of shallow landslides source areas using physically based models. Natural Hazards, 53, 313-332.

Sousa, L., Vargas, E., Jr., Sousa, R., and Chaminè, H. I. (2020). Hydrological risks in natural hazards focused on the role of the water: Studies on land-slides. In Advances in natural hazards and hydrological risks: Meeting the challenge. Advances in science, technology innovation (pp. 4347). Springer.

Spolverino, G., Capparelli, G., and Versace, P. (2019). An instrumented flume for infiltration process modeling, Landslide Triggering and Propagation. Geosciences, 9, 108.

Stormont, J. C., and Anderson, C. E. (1999). Capillary barrier effect from underlying coarser soil layer. Journal of Geotechnical and Geoenvironmental Engineering, 125 (8), 641-648.

Tufano, R., Formetta, G., Calcaterra, D., and De Vita, P. (2021). Hydrological control of soil thickness spatial variability on the initiation of rainfallinduced shallow landslides using a three-dimensional model. Landslides, 18, 3367-3380.

Van Genuchten, M. T. (1980). A closed-form equation for predicting the hydraulic conductivity of unsaturated soils. Soil Science Society of America Journal, 44, 892-898.

Warrick, A. W., Wierenga, P. J., and Pan, L. (1997). Downward water flow through sloping layers in the vadose zone: Analytical solutions for diversions. Journal of Hydrology, 192 (1-4), 321-337.

Wigmosta, M. S., Vail, L. W., and Lettenmaier, D. P. (1994). A distributed hydrology-Vegetation model for complex terrain. Water Resources Research, 30 (6), 1665-1679.

Chapter 3: Predicting Large-Scale Landslide Initiation Based on the Local Field Factor of Safety: An Application to the Braies Catchment in Northern Italy

Riccardo Busti[1], Giuseppe Formetta[1], Ning Lu[2]

[1]Department of Civil, Environmental and Mechanical Engineering (DICAM), University of Trento, Trento (TN), Italy

[2]Department of Civil and Environmental Engineering, Colorado School of Mines, Golden, CO 80401

This article advances understanding landslide prediction in the Alto-Adige region, IT, by coupling physically-based hydrological simulations with a slope stability model based on LFS criteria.

This chapter has been published in *ASCE,*

Journal of Geotechnical and Geoenvironmental Engineering: https://doi.org/10.1061/JGGEFK.GTENG-13888

Abstract

Landslides pose a significant hazard to citizens, infrastructures, especially in mountainous landscapes. The deterministic prediction of landslide susceptibility requires an incorporated approach between multiple disciplines such as geology, geomorphology, and hydrology. This study uses a hydromechanical framework aimed at predicting large scale shallow landslide initiation by calculating the local field factor of safety (LFS) as an indicator of slope instability. The framework integrates (1) a finite element method (FEM) solver for a coupled hydromechanical landslide model within a Java object-oriented modeling system, and (2) a third-party hydrologic model, enabling detailed multidimensional simulations of slope stability under transient rainfall conditions in large-scale hillslopes. The hydro-mechanical framework is validated through a benchmark test on a homogeneous, constant-slope hillslope and then are further applied to a large-scale real-world scenario in the Braies Alpine Catchment, Alto Adige, Northern Italy. The first application successfully predicted the triggering of a shallow landslide under sustained rainfall, while the second application accurately identified the initiation of multiple landslides during an intense summer storm. The results demonstrate the framework's capability to predict landslide initiation with high precision, even in complex slope environments, providing a cost-effective tool for landslide risk assessment.

3.1 Introduction

Landslides or hillslope instabilities present a devastating hazard to individuals, properties, and infrastructure, manifesting across diverse spatial and temporal scales in mountainous regions worldwide (e.g., Hungr et al. 2005; Froude and Petley 2018; Haque et al. 2019; Tyagi et al. 2022). Rainfall-triggered shallow landslides can cause significant destruction due to their rapid initiation and progression, often evolving into debris or earth flows that swiftly transport loose soil and rocks down steep slopes (e.g., Iverson and Reid 1997; Formetta and Capparelli 2019). These types of landslides pose a significant threat to human life, as well as to social and economic activities (e.g., Sorbino et al. 2009), largely due to the absence of warning signs in prefailure stage (e.g., Borrelli et al. 2018) and monitoring systems in areas with sparse measurement data (e.g., Patton et al. 2023). Landslide occurrence is increasing due to climate alteration, which enhances the frequency and intensity of heavy rainfall events, and land use changes (e.g., Gariano and Guzzetti 2016; Ciabatta et al. 2016; Alvioli et al. 2018; Petrovic et al. 2018), particularly in the Alpine region (e.g., Crozier 2010; Stoffel et al. 2014; Schlögel et al. 2020). Over the past two decades, the Alto Adige province has experienced over a thousand landslides between 2007 and 2021 (ISPRA 2021).

Forecasting susceptibility of slope instability demands an interdisciplinary approach that integrates geology, geomorphology, hydrology, and climatology, as these events are shaped by the interplay of multiple local factors. These factors can be quasi-static, such as slope gradient, geological composition, and geotechnical properties of the soil, or dynamic, such as the water table position, soil saturation level, root cohesion, and human activities (e.g., Wu and Sidle 1995; Rosso et al. 2006; Bozzolan et al. 2020; Morar et al. 2021). According to Piacentini et al. (2012): shallow landslides in the Alto Adige region are found in on slopes where highly permeable soils cover less permeable underlying layers. The failure surface usually develops along the boundary between the soil mantle and bedrock, following a path nearly parallel to the surface. It is essential to identify and understand the causes leading to landslide activation to accurately predict these destructive events, improve early warning systems, and design effective mitigation strategies (e.g., Calvello 2017).

Recently, there has been increasing attention on improving the understanding and measurement of hydrologic processes in landslide research using modeling methods (e.g., Greco et al. 2023). In this context, deterministic models support the physically based analysis of the hydrologic response of the site leading to landslide initiation. These models usually integrate the solution of a rainfall infiltration solver with the limit equilibrium methods (LEM). LEM are analytical techniques that analyze the equilibrium of forces and moments acting on a potential failure surface to assess hillslope stability (e.g., Fredlund and Krahn 1977). Within these methods, the infinite slope model is a simplified version useful for assessing shallow landslides in homogeneous materials where the slope is extensive compared to its thickness.

For large-scale slope instability predictions, infinite slope model has been widely used in literature combined with a steady state infiltration solution (e.g., Montgomery and Dietrich 1995), with transient 1-D solution (e.g., Godt et al. 2008), or with 2-D solution for a hillslope section (e.g., Capparelli and Versace 2014), and with 3-D solutions for watersheds (e.g., Simoni et al. 2008; Tufano et al. 2021; Formetta et al. 2016b). These methods have been effectively applied in recent decades to assess landslide occurrence in the North-Eastern Italian Alps (e.g., Borga et al. 1998; Lanni et al. 2012; Sanzeni et al. 2019; Paronuzzi and Bolla 2023). LEM offer simplicity, flexibility, cost-effectiveness, and wide acceptance, making them standard practice in geotechnical engineering for rapid preliminary slope stability assessments with minimal data requirements. However, LEM are based on (1) simplified force assumptions, (2) neglect deformation behavior, and (3) are limited by predefined failure surfaces, potentially leading to significant variability in results.

To address these limitations, Lu et al. (2012) introduced the concept of the scalar field of local factor of safety (LFS), a scalar quantity used to evaluate slope stability at each point in the hillslope, based solely on the stress field solution without the need for a predefined rupture surface (see section “Landslide Model” for details). Recent applications of this method (e.g., Lu and Godt 2013; Shao et al. 2015; Chen et al. 2018) have illustrated its accuracy and effectiveness in identifying potential failure surfaces of simplified hillslopes under transient rainfall conditions. Furthermore, the LFS has been used to estimate the effect of bedrock topography (Moradi et al. 2018) on slope stability for a benchmark slope, as well as to perform uncertainty propagation and sensitivity analysis of mechanical parameters (Abbasov et al. 2024). Yang et al. (2022) applied the LFS in combination with failure probability model to a real hillslope in China to examine landslide size, location, and timing under different rainfall patterns. The LFS method has already been tested into the SLOPE-CUBE module, which is part of the HYDRUS 2D-3D commercial software (Lu et al. 2019; Chen et al. 2018). Finally, recently developed multidimensional slope stability models (e.g., Mathews et al. 2024) account for the spatial variability of slope geometry, material properties, vegetation characteristics and hydrologic conditions, providing a more realistic representation of potential landslide source areas.

In this study, hillslope stability analysis is performed following the modeling framework (Fig. 7) proposed by Lu et al. (2012), which integrates hydrologic, mechanical, and landslide components. The framework addresses key limitations in existing approaches, particularly the common reliance on simplified 1D/2D hydrologic modeling and LEM simplifications. Specifically, our study seeks to improve the physical realism and spatial accuracy of slope failure predictions by coupling a 3D solution of the Richards equation with an effective stress analysis and the computation of the LFS as stability indicator. The modeling framework is structured into three parts: (1) a hydrologic model, based on any infiltration solver for variably saturated porous media to simulate the pressure field, soil weight, and suction stress; (2) a mechanical model that uses the finite element method (FEM) to solve for stress and displacement states in the ground; and (3) the landslide model that computes the LFS. The coupled approach (1)-(2)-LEM is commonly used to perform landslide analysis (e.g., Griffiths and Lane 1999; Borja and White 2010). The mechanical and landslide components are implemented in a Java objective-oriented modeling system (Fig. 3.1), while the hydrological model used is the open-source 3D GEOtop model.

This work advances previous efforts by enabling a basin-scale, physically based analysis of landslide processes in heterogeneous Alpine terrain, where complex topography, layered geology, and limited in-situ data present major modeling challenges. The proposed framework is validated against a benchmark test case and applied to a real-world scenario involving multiple rainfall-induced landslides in the Alto Adige region. Notably, this study represents a first application of the LFS to a regional-scale setting at northeastern Italian Alps, offering a new pathway for evaluating landslide triggering condition of Alpine hillslopes.

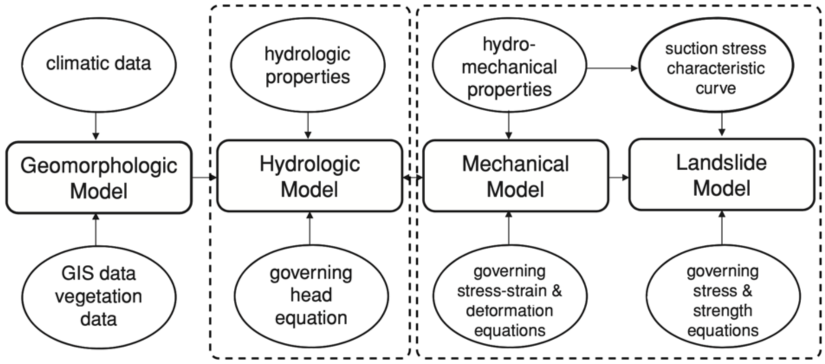

Figure 7. Hydromechanical framework for stability analysis of variably saturated hillslopes: geomorphologic model; hydrologic model; and mechanical and landslide models. The framework is independent of the hydrological model usde. The java-based mechanical and landslide model is presented in this paper.(Modified from Lu and Godt 2013.)

3.2 Study area

The study area is part of Val Pusteria, in the Province of Bolzano, Alto Adige, North-Eastern Italy (Fig. 8-a). Specifically, our focus is on the landslides that occurred on the night between August 5th-6th, 2017, in the rio Braies catchment, which is part of the Natural Park of Fanes-Sennes-Braies in the Dolomites. The analyzed catchment (Fig. 8-c) includes Valle di Braies (on the west side), where the rio Braies springs from the homonymous lake, and Val di Stolla (on the east side), which is crossed by the rio Stolla. The two streams merge in the town of Ferrara. The study area features a typical dolomitic mountainous landscape with elevations ranging between 1,000 and 3,000 m above sea level (a.s.l)., and narrow steep valleys. Higher altitudes are characterized by a scattered series of individual buildings, while small, urbanized areas (Ferrara and San Vito di Braies) and agricultural cultivations are developed in the valleys and piedmont sectors. The hillslopes exhibit the typical alpine landscape, with a succession of dense woods, sparse vegetation, shrubs, slope debris, and bare rock, with increasing elevation. Sediments consist predominantly of slope debris, alluvial or debris flow fans, and glacier material deposited on volcanic rocks (Irmler et al. 2006).

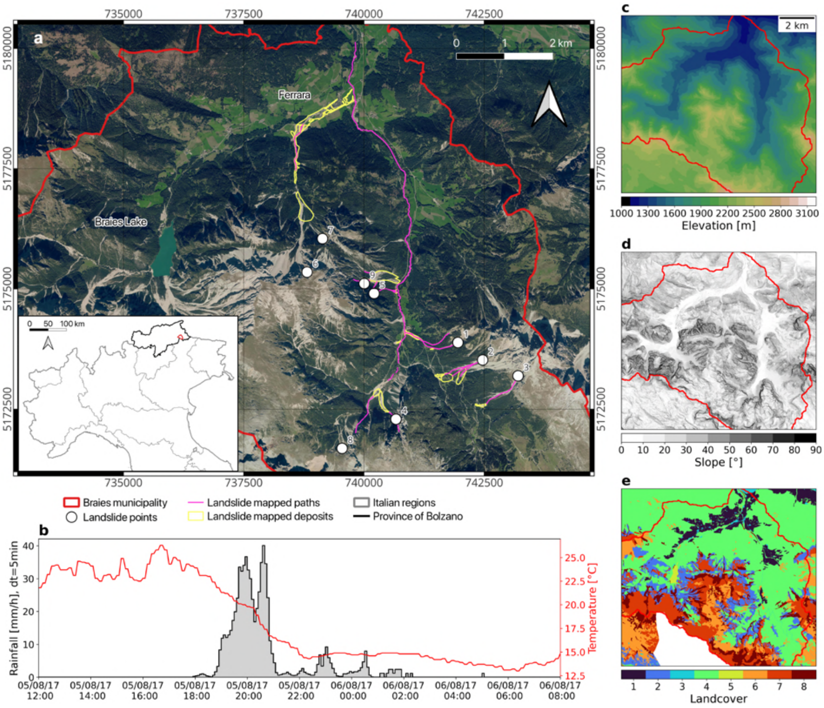

Figure 8. (a) Orthophoto of the Braies municipality, with an inset showing its location within the Province of Bolzano, northern Italy. Mapped August 5th-6th, 2017 landslide features include points, scars or deposits, and flow paths. (b) Time series of rainfall (shaded area) and temperature (black line) used in the hydrological analysis; (c) digital elevation model; (d) slope map; and (e) land cover classification map, where categories are: 1 = agricultural land, 2 = shrubs, 3 = urban area, 4 = forest, 5 = water bodies, 6 = meadow, 7 = rock, and 8 = debris zones. Panels (a and c-e) show the elaboration of topographic maps (WEBGIS Bolzano 2025) and landslide geospatial features (Ufficio Centro Funzionale Provinciale, personal communication, May 8, 2025).

3.3 Modeling Framework

The proposed framework combines three coupled components: (1) the hydrologic model solving the three-dimensional pressure field within the catchment, (2) the mechanical model solving the state of displacement and stress for a multilayer elastic hillslope, and (3) the landslide model predicting the slope stability by computing the LFS in each point of the domain, using the suction stress-based unified effective stress.

3.3.1 Hydrologic Model

The GEOtop 3-D hydrologic model (Bertoldi et al. 2006; Rigon et al. 2006) is a physically-based, spatially distributed computational tool designed to simulate the hydrologic cycle by solving the coupled water-energy balance system within a catchment. The model integrates a three-dimensional grid discretization of the landscape with spatially distributed meteorological forcing, land cover, and soil data. This enables a comprehensive, physically based understanding of hydrologic processes, including discharge generation, soil moisture dynamics, snow melting and freezing, and terrain effects, which is particularly important for mountainous and complex terrains (Endrizzi et al. 2014). The model has been effectively applied in diverse scenarios, including agricultural catchments (Formetta et al. 2016), pyroclastic layered hillslopes (Formetta et al. 2019; Tufano et al. 2021; Busti et al. 2024), and experimental weathered catchments (Formetta et al. (submitted); Moon et al. (under review)) to estimate water balances and assess landslide initiation.

The water budget equations in GEOtop are based on the De-Saint Venant equation for modeling overland runoff and channel flow, and the Richards equation (Eq. 1) for simulating variably saturated groundwater dynamics. Subsurface hydraulic properties, especially for unsaturated flow in porous media, are described using the Van Genuchten equation (1980) in conjunction with the Mualem parameterization (1976). These equations characterize the Soil Water Retention Curve (SWRC, Eq. 2) and the Hydraulic Conductivity Function (HCF, Eq. 3):

$$\frac{\partial \theta}{\partial \mathrm{t}} - \mathrm{k}\nabla \cdot (h + z) = S_w \tag{1}$$

$$\theta = \begin{cases} \theta_r + \frac{\theta_s - \theta_r}{(1+|\alpha h|^n)^m}, & h < 0, m = 1 - 1/n \\ \theta_s, & h \geq 0 \end{cases} \tag{2}$$

$$k = k_s \sqrt{S} \left[1 - \left(1 - S^{\frac{1}{m}} \right)^m \right]^2, \quad S = \frac{\theta - \theta_r}{\theta_s - \theta_r} \tag{3}$$

where h [kPa] is the pore water pressure, θ_r [dimensionless] and θ_s [dimensionless] are the residual and saturated water content, k [mm/s] and k_s[mm/s] are the unsaturated and saturated hydraulic conductivities, S [dimensionless] is the saturation degree, α [1/kPa] and n [dimensionless] depend on the air-entry pressure and pore-size distribution. S_w [1/s] is a mass sink term.

The energy budget in the hydrologic model GEOtop calculates the variation in the volumetric internal energy of the soil by incorporating turbulent fluxes across the soil-atmosphere interface. These include thermal fluxes, sensible heat flux, evapotranspiration, net radiation, and energy input from precipitation (Bertoldi et al. 2006; Rigon et al. 2006). The model explicitly accounts for snowmelt, sublimation, and energy exchanges during phase changes within the snowpack, considering both saturated and unsaturated soil conditions, as well as freezing and thawing processes (Dall'Amico et al. 2011; Endrizzi et al. 2014; Gubler et al. 2013). A multilayer representation of snow cover is fully integrated into the surface energy balance and the heat equation, ensuring a detailed simulation of snow dynamics (Endrizzi et al. 2014). To simulate energy and water flux exchanges between vegetation and the ground surface, the model employs a double-layer structure with canopy (Endrizzi and Marsh 2010). Evapotranspiration is calculated as the sum of three components: evaporation from bare soil, evaporation from wet vegetation, and transpiration from plants (Rigon et al. 2006).

3.3.2 Mechanical Model

The mechanical model solves the 2-D ground stresses and displacements by incorporating the field of moist unit weight as the gravity term and suction stress as part of the effective stress (e.g., Lu and Godt 2013). It operates under linear elasticity while extending functionality to account for gravity effects, their time-dependent nature due to variable unit weight, and the inclusion of suction stress in effective stress and displacement computations (e.g., Lu et al. 2019). For static force equilibrium, the momentum balance is satisfied in both horizontal and vertical directions, resulting in system of equations that describe the two-dimensional gravity-induced stress field in a slope (e.g., Lu and Godt 2013):

$$\nabla \cdot \boldsymbol{\sigma} + \boldsymbol{b} = 0, \boldsymbol{\sigma} = \begin{bmatrix} \sigma_x & \tau_{xy} \\ \tau_{xy} & \sigma_y \end{bmatrix}, \boldsymbol{b} = \begin{bmatrix} 0 \\ -\gamma g \end{bmatrix} \tag{4}$$

where $\boldsymbol{\sigma}$ [kPa] is the stress tensor with three independent stress variables in two-dimensional space, i.e, σ_x is the normal total stress in the horizontal direction x, σ_y is the normal total stress in the vertical direction y, and τ_{xy} is the shear stress, $\boldsymbol{b}$ is the unit vector of body forces with two components, g $[m/s^2]$ is gravity, γ $[kN/m^3]$ is the field of moist unit weight computed as:

$$\gamma = \gamma_w \frac{G_s + eS}{1+e} \tag{5}$$

in which formulation G_s [dimensionless] is the specific gravity, γ_w $[kN/m^3]$ is the specific weight of water, and e [dimensionless] is the void ratio. The saturation degree S [dimensionless] is solution of the hydrologic model. The linear elastic theory describes the deformation of soils, i.e., relationship between the stress field and displacement field (e.g., Reddy 1985):

$$\boldsymbol{\sigma} = \boldsymbol{D\varepsilon} = \boldsymbol{DBu},$$

$$\boldsymbol{\sigma} = \begin{bmatrix} \sigma_x(x,y) \\ \sigma_y(x,y) \\ \tau_{xy}(x,y) \end{bmatrix}, \boldsymbol{\varepsilon} = \begin{bmatrix} \varepsilon_x(x,y) \\ \varepsilon_y(x,y) \\ \varepsilon_{xy}(x,y) \end{bmatrix}, \; \boldsymbol{B} = \begin{bmatrix} \frac{\partial}{\partial x} & 0 \\ 0 & \frac{\partial}{\partial y} \\ \frac{\partial}{\partial x} & \frac{\partial}{\partial y} \end{bmatrix}, \; \boldsymbol{u} = \begin{bmatrix} u(x,y) \\ v(x,y) \end{bmatrix} \tag{6}$$

where $\boldsymbol{D}$ [kPa] is the stiffness matrix, $\boldsymbol{\varepsilon}$ [dimensionless] is the strain vector, $\boldsymbol{B}$ $[m^{-1}]$ is the strain matrix and $\boldsymbol{u}$[m] is the displacement vector, i.e., u is the displacement in horizontal direction and v is the displacement in vertical direction. The plane strain condition assumes that there is no deformation or strain in the direction perpendicular to the 2-D plane being analyzed (i.e., $\varepsilon_z = 0$). The assumption is appropriate for problems where the out-of-plane dimension is significantly larger than the in-plane dimensions, such as in long slopes or embankments. Under this condition, stresses can still exist in the out-of-plane direction (i.e., σ_z), but they are determined indirectly based on the in-plane stresses and material properties. The plane strain condition is commonly used in geotechnical and geological engineering for analyzing stress and deformation in structures like hillslopes, dams, and tunnels. In this case, the matrix $\boldsymbol{D}$, which depends only on the Elastic Module E [kPa] and the Poisson ratio ν [dimensionless], assumes the following form (e.g., Reddy 1985):

$$\boldsymbol{D} = \begin{bmatrix} \frac{(1-\nu)E}{(1+\nu)(1-2\nu)} & \frac{\nu E}{(1+\nu)(1-2\nu)} & 0 \\ \frac{\nu E}{(1+\nu)(1-2\nu)} & \frac{(1-\nu)E}{(1+\nu)(1-2\nu)} & 0 \\ 0 & 0 & \frac{E}{2(1+\nu)} \end{bmatrix} \tag{7}$$

The numerical solution of the system (3) is achieved through the Finite Element Method (FEM). In the FEM formulation (Reddy 1985), the hillslope is discretized into smaller finite elements. Within each element, the displacement solution is approximated using shape functions, which describe how displacements change. The momentum equations (3) for each element are then assembled into a global system of equations that represents the entire problem. The global system of equations is solved numerically to find approximate solutions at the mesh nodes. Boundary conditions, which include constraints and external forces, are applied to reflect the real-case scenario. FEM is essential for analyzing localized strain and stress in hillslopes, capturing different geometries and/or material heterogeneity (e.g., Griffiths and Lane 1999), and failure initiation mechanisms like toe stress concentration (Eberhardt et al. 2004) or strain localization (Borja and White 2010). The detailed description of the implemented FEM is in Lu et al. (2019).

3.3.3 Landslide Model

Slope stability analysis has been traditionally performed with limit equilibrium methods (e.g., Fellenius, 1936; Bishop, 1955, Morgensten and Price, 1965; Janbu 1973) Those methods greatly simplify slope stability analysis with three propounding assumptions: 1) a priori assumption of the failure surface geometry, 2) failure occurs simultaneously at every point along the failure surface, and 3) simplification or neglection of part of the internal forces. Because the classical use of the factor of safety seeks the single and minimum for the entire slope, it cannot describe where the failure begins or how the failure evolves in space and time. Furthermore, most conventional slope stability methods adopt simplifications or ignore the effects of pore-water pressure above the water table (e.g., Lu and Godt 2013).

To overcome the previous limitations, the hillslope stability is assessed using the concept of scalar field of local factor of safety (LFS) presented in Lu et al. (2012). LFS is a scalar quantity that is indicative of the stability of each point in the domain. When LFS>1 means the slope is stable, while LFS\le1 the slope is unstable. This approach is particularly well-suited for FEM, as it enables the calculation of displacement and stress throughout the entire hillslope, facilitating the determination of a factor of safety at each element (e.g., Iverson and Reid 1992). Assuming the validity of Mohr-Coulomb failure criterion, the LFS is defined as the ratio between the current shear stress τ and the shear strength τ^*(Lu et al. 2012) as an indicator of how far the hillslope stress is from the failure (Fig. 9). The LFS can be computed graphically by similarity of triangles ACD and ABE (Fig. 9):

$$LFS = \frac{\tau^*}{\tau} = \frac{AE}{AD} = \frac{BE}{CD} = \frac{BG}{CH} \tag{8}$$

By substituting the stress quantities, the definition of the LFS becomes:

$$LFS = \frac{2cos\phi}{q'}(c + p'tan\phi) \tag{9}$$

where ϕ [°] is the friction angle, *c* [kPa] is the cohesion, p',q' [kPa] are the mean and deviatoric effective stresses defined as:

$$p' = \sigma_I' = \frac{\sigma_1' + \sigma_3'}{2} = \frac{\sigma_1 + \sigma_3}{2} - \sigma^s, \qquad q' = 2\sigma_{II}' = \sigma_1' - \sigma_3' = \sigma_1 - \sigma_3 \tag{10}$$

where σ'_1, σ'_3 [kPa] are the major and minor principal stress, that can be computed with the Circle of Mohr using the solution of the field stress:

$$\sigma_{1,3} = \frac{\sigma_x + \sigma_y}{2} \pm \sqrt{\left(\frac{\sigma_x - \sigma_y}{2}\right)^2 + \tau_{xy}^2} \tag{11}$$

To evaluate the effect of unsaturated conditions on soil strength, we compute the suction stress (i.e., σ_S [kPa]) characteristic curves (SSCC), as function of the hydraulic properties of the hillslope material (Lu and Likos 2006):

$$\sigma^s = \begin{cases} Sh & h < 0 \\ h & h \geq 0 \end{cases} \tag{12}$$

For positive pore water pressure, the suction stress equals the pore water pressure h, whereas for negative pressure, it follows the pattern defined by SWRC. Eq. 12 provides a unified description of flow and stress in unsaturated soils using a single set of hydromechanical parameters, without requiring a separate shear strength criterion beyond the Mohr-Coulomb failure criterion. This formulation has been extensively validated for various soils under soil suction <1500 kPa (Lu et al. 2010; Lu and Godt, 2013). The SSCC is finally introduced in the Terzaghi's effective stress formulation $\boldsymbol{\sigma}' = \boldsymbol{\sigma} - \sigma^s$ since is both valid for saturated and unsaturated conditions. Slope stability is evaluated at each time step and at every point along the hillslope by: receiving the pressure field output from GEOtop, updating the soil weight and suction stress accordingly, and computing the LFS. These variables directly affect soil strength, which decreases as pore pressure increases and suction stress rises.

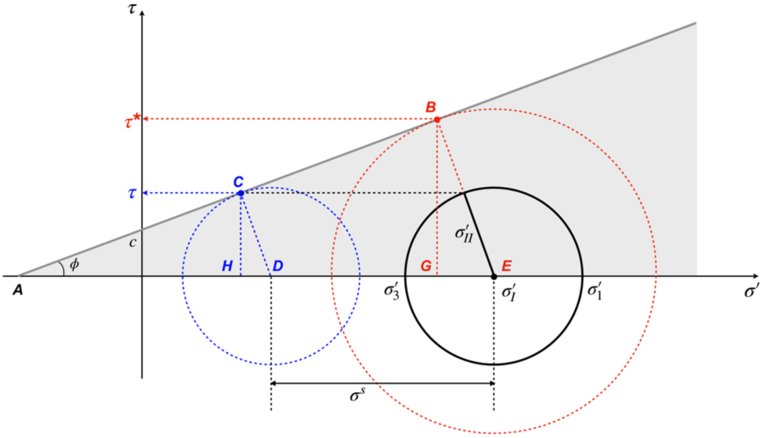

Figure 9. Conceptual model illustrating the local factor of safety (LFS), adapted from Lu et al. (2012). The current stress state (bold line) has a shear stress (dashed line) and a shear strength (dotted line). The gray area is the region of stability individuated by the Coulomb-Mohr criterion. The ratio between these two quantities, τ^*/τ represents the proximity to failure. A reduction in suction stress (due to an increase in positive pore pressure) causes the Mohr circle to shift leftward, decreasing the LFS. When the condition LFS ≤ 1 is satisfied, failure occurs.

3.4 Applications

3.4.1 Benchmark Test on a Slope Instability with Homogeneous Soil

The first application performs the stability analysis of a 23-degree hillslope with homogeneous soil (Fig. 10) (Lu et al. 2019). The hillslope is 15 m long and 6 m high. The hydromechanical properties are listed in Tab. 2. The boundaries are set 7 m away from the base of the hillslope on the right, 20 m away from the top of the hillslope on the left, and 19 m below the toe of the hillslope. The following boundary conditions for the mechanical model are assumed at three borders: no horizontal displacement on left and right sides, and no vertical displacement on the bottom. The hillslope is subjected to a constant rainfall intensity of 20 mm/h for 15 h.

Soil Parameter	Symbol	Value	U.M
Van Genuchten parameter 1	α	0.4	1/kPa
Van Genuchten parameter 2	n	1.8	-
Saturated hydraulic conductivity	k_s	0.0583	mm/s
Residual water content	θ_r	0.045	-
Saturated water content	θ_s	0.43	-
Specific gravity	G_s	2.6	-
Void ratio	e	0.5	-
Elastic module	E	10^7	kPa
Poisson module	ν	0.33	-
Cohesion	c	1	kPa
Friction angle	ϕ	40	degrees

Table 2. Hydraulic and mechanical parameters used for the benchmark application

The initial condition is a hydrostatic condition with a water table at 17 m height. A no flow boundary condition is set on the left border, on the bottom and on the right side below the water table level. The mechanical and hydraulic parameters are listed in Tab. 2. Fig. 10 shows the computational domain and the hydrologic curves (i.e., SWRC, HFC, SSCC) adopted in this application. The digital elevation model used to perform the hydrologic simulation with GEOtop has a resolution of 0.5 m. The vertical discretization consists in an increasing mesh size with depth (50 mm down to 2 m, 100 mm down to 6 m, 200 mm down to 25 m). The integration timestep is 1 min. The computational mesh used by the mechanical model is made of 6-nodes triangle, that are smaller and denser close to the surface, for a total amount of approximately 8,000 nodes and 3,900 elements.

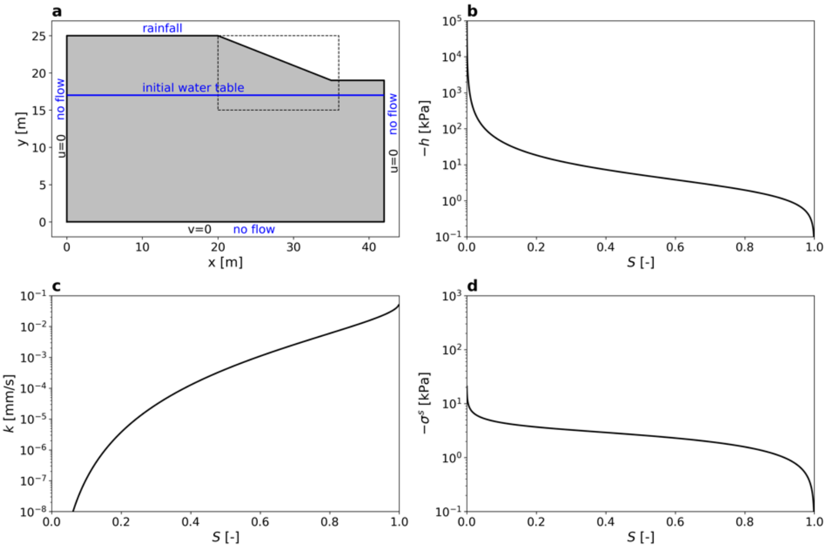

Figure 10. (a) Hillslope geometry, initial and boundary conditions for hydrologic (water table position and flux at borders) and mechanical models (displacements). The dashed black rectangle is the zoomed-in view shown in Fig. 12; (b) soil water retention curve; (c) hydraulic conductivity function; and (d) suction stress characteristic curve.

3.4.2 Large-Scale Application to the Alto Adige Hillslopes

The second application focuses on the stability analysis of multiple failed hillslopes within the Braies catchment (Fig. 8-a). This study specifically examines 9 landslides that occurred in the eastern part of the catchment during a storm that took place on the night of August 5th-6th, 2017. The triggering storm (Fig. 8-b) is characterized by a two-peak rainfall, with maximum intensities of 36.7 mm/h at 20:00 and 40.1 mm/h at 20:40. The total cumulative precipitation recorded from the beginning of the storm at 18:00 to its conclusion at 02:00 on August 6th is 58.4 mm. The meteorological data were acquired from the Meteo browser database of the Province of Bolzano (MeteoBrowser 2025) at a 5-minute resolution. These data have also been utilized in conjunction with Meteo radar in previous studies (e.g., Scorpio et al. 2022).

The 5-m resolution DEM (Fig. 8-c), downloaded from the web GIS portal of the Province of Bolzano (WEBGIS Bolzano 2025), is utilized to generate the other maps required for hydrologic simulations, as for example the slope map (Fig. 8-d). Fig. 8-e also depicts the land cover of the catchment, which is used to assign the vegetation parameters (e.g., canopy height, LAI, root depth) to each pixel to estimate the evapotranspiration. The 3D hydrologic simulation is performed using the GEOtop model, with a vertical discretization scheme consisting of a depth-increasing grid: 50 mm down to a depth of 2 m, 100 mm down to 4 m, 200 mm down to 10 m, and 500 mm down to 20 m. The model assumes an impermeable bottom boundary, along with lateral boundaries for the catchment, except at the river network outlet. The initial condition is defined by a water table positioned 10 m below the surface. The initial conditions before to the storm were determined using the setup period approach of Binley and Beven (1992), based on three months of recorded precipitation. This approach has also been adopted in other 3D hydrological studies (e.g., Ebel et al. 2007). The simulation runs with a 5-min integration time step.

The subsurface is divided into two distinct layers: soil and bedrock. The spatial distribution of soil depth, s_d is modeled using the $s_d = s_{d,0} cos\alpha$, where α is the slope angle, and $s_{d,0}$ is a reference soil depth at zero slope, set to 2 m. This equation predicts deeper soils in flat areas and shallower soils on steep slopes. This modeling approach has been previously applied in studies of Italian terrain (e.g., Del Soldato et al. 2018; Tufano et al. 2021). The resulting soil depth distribution is shown in the boxes within the subplots of Fig. 11 for the areas surrounding the landslides. The modeled soil depths are consistent with measured values from other studies in the Bolzano province (e.g., Sanzeni et al. 2019). Hydraulic parameters for the soil and bedrock are sourced from the EU-SoilHydroGrids ver1.0 database with a resolution of 250 m (Hengl et al. 2017; Toth et al. 2017). The geotechnical properties (e.g., friction angle, cohesion, elastic modulus) of coarse-grained soils and dolomitic rock are derived from ranges provided in the literature (e.g., Bell 2007) for these geological formations. The full set of parameters for this large-scale application is listed in Tab. 3.

For the 2D mechanical model, 9 cross sections of the failed hillslopes (Fig. 11) are extracted by profiling the DEM and soil depth maps along the landslide scars identified in the orthophotos. The failed hillslopes, approximately 100 m in length, are extended 200 m to the left and right to minimize boundary effects in displacements calculation. The bottom boundaries are set at a depth of 200 m from the base of the hillslopes. Boundary conditions are the same as in the first application: no horizontal displacement on the lateral sides and no vertical displacement at the bottom. The computational mesh used in the mechanical model is made of 6-node triangular elements, with finer and denser meshing in the soil layer and the bedrock immediately below the soil-bedrock interface. On average, the mesh consists of 150,000 nodes and 80,000 elements, for each hillslope. Fig. S5 provides a 3D view of the DEM, including two cross sections that illustrate the north-south and east-west transects of the 3D computational grid used in the hydrological model, as well as the 2D mesh used in the mechanical model.

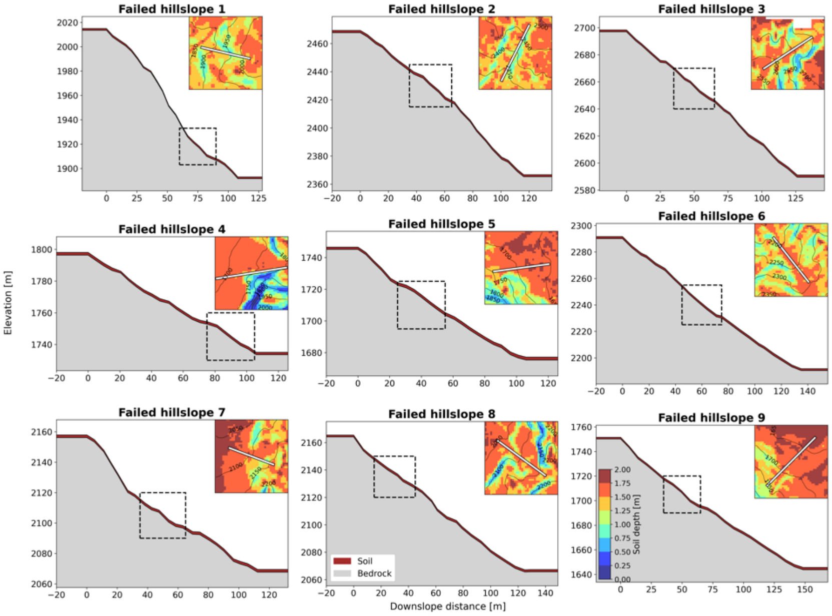

Figure 11. Cross sections of 9 failed hillslope pointed out in Fig. 8-a. For each hillslope we display: the soil layer (in dark grey), the bedrock layer (in light grey), the soil depth map close to the landslide area. Dashed rectangle is the zoom in view showed in Figs. 14 and 15.

To assess how uncertainty in mechanical parameters affects the LFS evaluation, we conduct a Monte Carlo simulation using 100 parameter sets sampled from a lognormal distribution (e.g., Formetta et al. 2016a; Arnone et al. 2016). The soil friction angle ϕ and soil cohesion c are treated as random variables with standard deviations set to 10% of their respective mean values (Tab. 3).

Soil Parameter	**Symbol**	**Value (soil)**	**Value (bedrock)**	**U.M**
Van Genuchten parameter 1	α	0.17	0.12	1/kPa
Van Genuchten parameter 2	n	1.30	1.12	-
Saturated hydraulic conductivity	k_s	$6.2 \cdot 10^{-3}$	$6.5 \cdot 10^{-5}$	mm/s
Residual water content	θ_r	0	0	-
Saturated water content	θ_s	0.55	0.45	-
Specific gravity	G_s	2.6	2.8	-
Void ratio	e	0.5	0.2	-
Elastic module	E	10^4	10^7	kPa
Poisson module	ν	0.33	0.33	-
Cohesion	c	15	1000	kPa
Friction angle	ϕ	30	40	degrees

Table 3. Hydraulic and mechanical parameters used for the large-scale application

3.5 Results and Discussion

3.5.1 Prediction Results and Analysis

Fig. 12 illustrates the evolution of water content, suction stress, and LFS for the benchmark test of a homogeneous hillslope at different hours following the onset of infiltration. In the first column, the water content evolution is depicted. Initially, at 0 h, the hillslope shows a stratified moisture distribution, with higher water content near the base and lower content toward the surface. As infiltration progresses, the wetting front moves downward into the slope. By 1 h, the surface layer begins to show increased moisture, and by 3 h, this wetting front has penetrated further, significantly increasing the water content in the upper layers. After 15 h, the wetting front has reached deeper into the slope, resulting in a substantially wetter profile compared to the initial state.

The second column in Fig. 12 presents the changes in suction stress. At 0 h, the suction stress is most negative at the top of the slope, reflecting strong unsaturated conditions, with less negative values toward the base. As time progresses and infiltration occurs, the suction stress decreases near the surface, indicating a reduction in the soil's ability to resist shear forces due to increased water content. By 15 h, the suction stress has notably decreased across the slope, particularly where the soil has become almost saturated.

The third column in Fig. 12 shows the evolution of the LFS. At 0 h, the slope is entirely stable, with LFS values greater than 1. As infiltration progresses, there is a gradual reduction in LFS, particularly near the surface where the wetting front is advancing. By 3 h, while the slope remains mostly stable, some areas begin to approach and overcome the critical threshold (e.g., on top of the hillslope). After 15 h, portions of the slope exhibit LFS values below 1, highlighted by the white segment, indicating instability and the onset of slope failure.

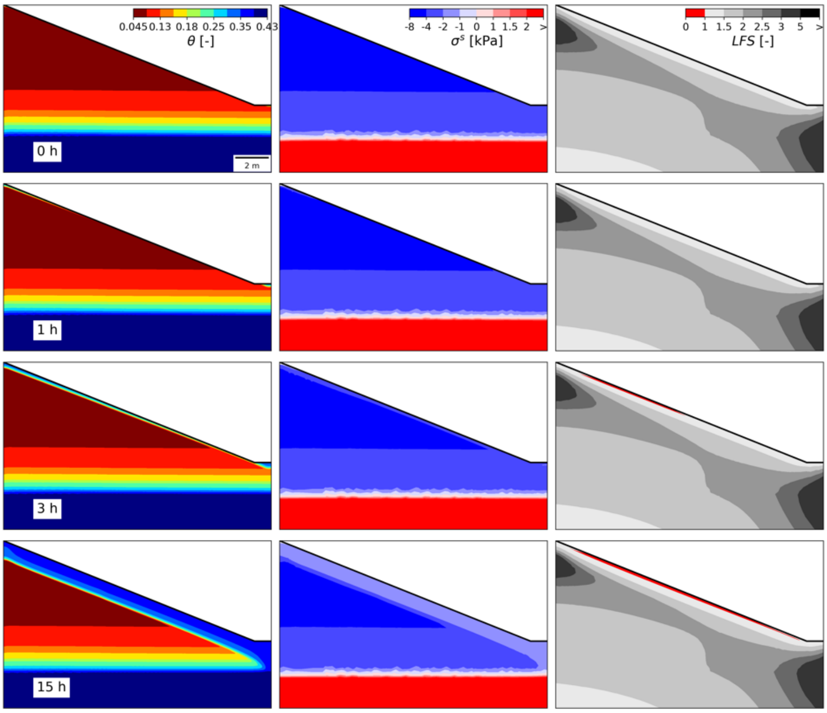

Figure 12. Soil moisture, suction stress, and LFS contours in a hillslope with constant slope angle and homogeneous soil at 0, 1, 3, 15 h. The first column shows the evolution of the infiltration, the second column shows the evolution in the suction stress field, and the third column shows the evolution of the failure surface, indicated by the red is with $LFS \leq 1$.

Fig. 13 presents the time series of suction stress and the LFS for 9 hillslopes in the Braies catchment, Alto Adige, that experienced failure. The figure shows the evolution of these variables at different depths within the landslide area, specifically at 0.5 m, 1 m, and just above the soil-bedrock interface, along with the corresponding rainfall intensity. The analysis reveals a consistent pattern across all hillslopes, where the LFS decreases, and the suction stress increases with ongoing rainfall infiltration.

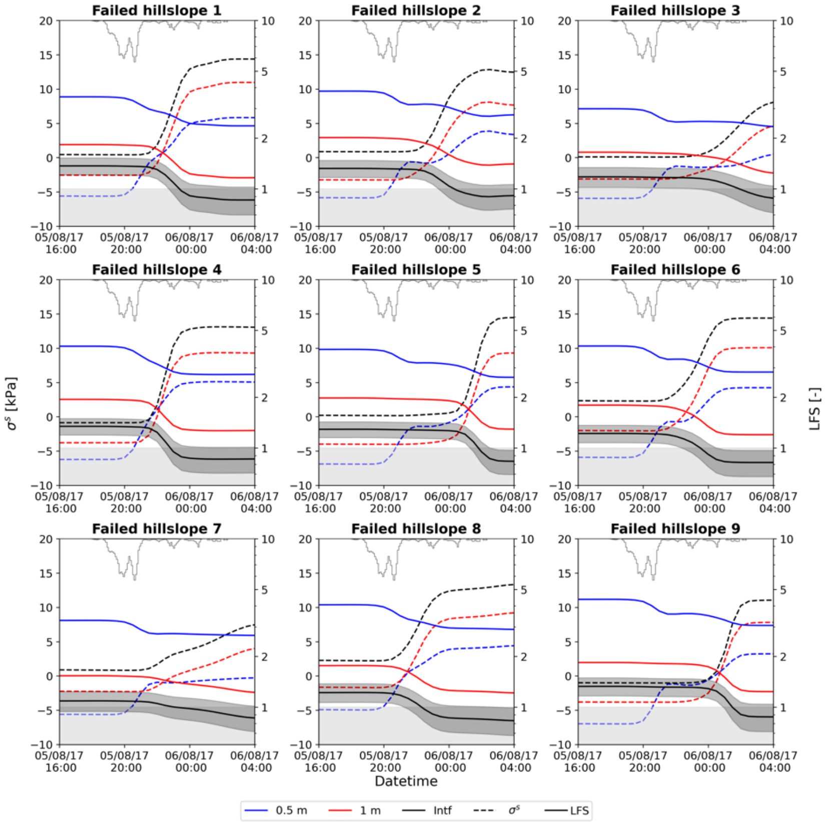

Figure 13. Time series of suction stress (dashed line) and local field safety factor (solid line) in correspondence of the 9 triggered landslides at different depths (i.e., 0.5 m, 1m and right above the soil-bedrock interface), together with the rainfall intensity (on top). Gray area indicates the region of LFS ≤ 1. The shaded area represents the 5th-95th percentile prediction interval of the LFS at the base of the soil, derived from the Monte Carlo analysis performed on soil friction angle and soil cohesion.

Initially, all depths exhibit LFS values above 1, indicating stable conditions. As infiltration progresses, the LFS begins to decrease, with the most significant drops occurring near the soil-bedrock interface. In all hillslopes, LFS values fall below 1 at this depth, signaling landslide initiation at the soil-bedrock interface. The increase in suction stress is more pronounced at shallower depths, coinciding with rainfall events, while the delayed response at deeper depths is primarily attributed to the low magnitude of unsaturated hydraulic conductivity. The temporal correlation between the decrease in LFS and the increase in suction stress indicates that the reduction in soil strength due to elevated water content plays a critical role in triggering landslides in these areas. The shaded gray areas in Fig. 13 represent the 5th-95th percentile confidence interval of the modeled LFS distribution obtained through Monte Carlo simulations. The 5th percentile LFS uncertainty scenario (lower bound of the prediction interval) indicates that for certain combinations of low mechanical parameter values, LFS can drop significantly (below 0.7), meaning that also landslide size is likely increasing. Notably, only hillslopes 3 and 7 appear consistently unstable even before the storm event. In contrast, for the 95th percentile LFS uncertainty scenario (upper bound of the prediction interval), all hillslopes, except for hillslopes 5, 6, and 8, remain stable throughout and after the storm. This analysis highlights that the uncertainty in mechanical parameters can substantially reflects on the simulated mechanical response of the slope. Fig. S6 displays the time series of pore water pressure at three different depths in the soil, up to three weeks before the event together with the estimated evapotranspiration flux for all 9 hillslopes.

Figs. 14 and 15 display the cross sections of the LFS for all failed hillslopes both before the beginning of the storm and at the moment of failure. Figs. S7 and S8 show the same cross-section views of the 5th quantile and 95th quantile LFS results of the Monte Carlo analysis. Initially, all hillslopes are stable, with both the bedrock and the overlying soil exhibiting LFS values greater than 1. Higher LFS values are observed in the shallower soil layers (e.g., LFS > 1.5 above 1 m depth on average), where the soil is unsaturated. In contrast, lower LFS values are found near the soil-bedrock interface, where pressure levels are higher. As the storm progresses, the LFS values decrease throughout the soil profile, eventually dropping below 1 (indicated by the white segment) near the soil-bedrock interface. This drop in LFS determines the initiation of landslides at the base of the soil layer. The likely cause of the instability is water accumulation at the base of the soil, where the low-permeability bedrock impedes drainage. This is amplified by lateral flow driven by the topographic gradient and modeled soil depth, which channels water into hollows and increases pressure at the soil-bedrock interface.

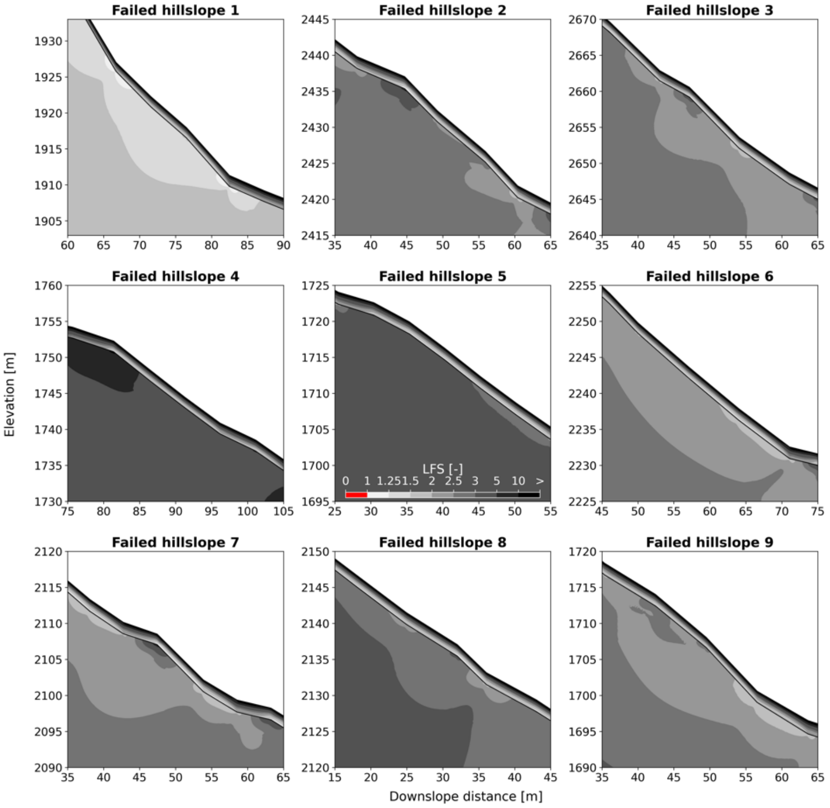

Figure 14. Cross sections of 9 hillslopes within the Braies catchment before the storm. The LFS is mapped along each hillslope, with darker shades representing areas of higher stability.

3.5.2 Practical Implications of Using Physically Based LFS Framework

Despite decades of development in slope stability modeling, accurately quantifying the mechanisms that trigger rainfall-induced landslides remains challenging and subject with uncertainty. The complexity arises from the multiphysical processes involved, which encompass both mechanical and hydrologic factors. These processes are further influenced by variables such as slope and bedrock topography, rainfall history, and sediment properties (e.g., Borja et al. 2012). This raises the question of whether an accurate, physically based model or other simulation tool exists that can reliably predict the location and timing of slope failures, particularly with validation against real-scale failed slopes. The framework employed in this study (Fig. 7) is designed to integrate the results of transient hydrologic analysis with stress computation at local, hillslope and basin scale, to lastly predict landslide occurrence through the evaluation of the LFS.

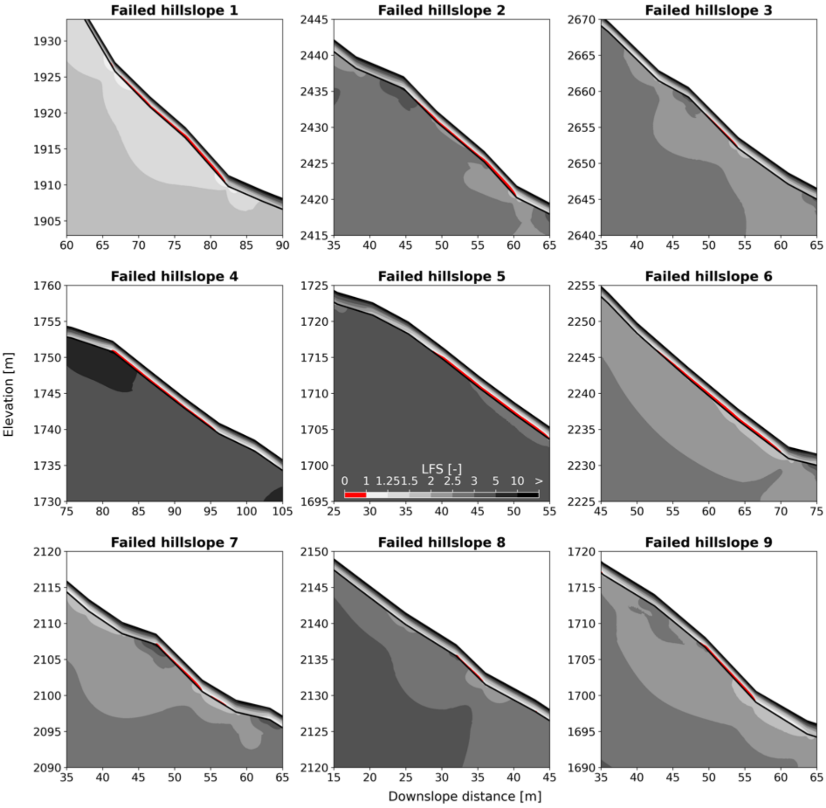

Figure 15. Cross sections of 9 hillslopes within the Braies catchment at the timing of landslide occurrences. The LFS is mapped along each hillslope, with darker shades representing areas of higher stability. The red segments indicate portions of the soil where LFS ≤ 1, corresponding to the initiation zones of landslides.

Failure surface-based (e.g., LEM) and stress field-based (e.g., LFS) slope stability analyses represent two fundamentally different methodologies for assessing landslide potential. In failure surface-based approaches, stability is evaluated by assuming a potential slip surface, often circular or arbitrarily shaped, and calculating the balance of driving and resisting forces along that surface. The result is a single factor of safety that reflects whether the slope is likely to remain stable or fail along the assumed surface. While these methods are widely used due to their simplicity and efficiency, they rely heavily on prior assumptions about the geometry of the failure mechanism and often treat the slope as a rigid body, without accounting for progressive deformation or internal strain. In contrast, stress field-based approaches, evaluate stability by computing the stress state at every point within the slope. Rather than requiring an a priori failure surface, zones of instability emerge naturally from areas where the local stress conditions exceed the material strength. This method offers a more mechanistic and detailed representation of slope behavior.

While LFS method provide a more comprehensive picture of slope stability, it requires more detailed input data than failure surface-based techniques. Nonetheless, for scenarios involving layered materials, complex subsurface hydrology, or the need to identify localized failure initiation points, stress field-based analysis presents a significant advantage in capturing the true behavior of natural slopes. In this study, the LFS demonstrated the potential for identifying specific zones of shallow landslide initiation, such as near-surface layers in the benchmark case (Application 1) or the soil-bedrock interface for real site application (Application 2).

The accuracy of LFS estimates is closely linked to the resolution of the underlying DEM, as terrain representation directly influences both mechanical and hydrological controls on slope stability (e.g., Paudel et al. 2016). Coarse-resolution DEMs tend to smooth or underrepresent local topographic gradients, which directly affects the estimation of driving stresses and influence the lateral redistribution of soil moisture across the basin, which in turn controls pore water pressure conditions that affect slope stability (e.g., Arnone et al. 2021). While fine resolutions (10-20 m) better capture slope morphology and hydrological patterns (e.g., Keijsers et al. 2011), excessively fine resolutions may reduce prediction accuracy, as highly localized topographic detail may not reflect slopescale processes (e.g., Tarolli and Tarboton 2006), particularly in complex, stratified terrain where data are not enough to characterize correctly the subsurface. Viet et al. (2016) demonstrated that finer grids (e.g., 5 m) enhance the spatial accuracy of landslide location predictions, while intermediate resolutions (10-15 m) offer better performance in timing, indicating a trade-off between spatial detail and temporal realism.

3.5.3 Comparison with Other Landslide Studies in Alto Adige

While the physically based modeling approach presented in this study offers detailed insights into the local mechanisms driving shallow landslide initiation in Alto Adige, it is also important to contextualize these results within the broader scope of landslide susceptibility assessment efforts carried out in the same region. Several recent studies have explored alternative, data-driven strategies to evaluate landslide hazard across Alto Adige, using regional event inventories and statistical modeling techniques to evaluate slope failure.

Piacentini et al. (2012) were the first to develop a regional-scale shallow landslide susceptibility map for the Alto Adige region (~7,500 km2), using the weight of evidence method based on 882 recorded events and considering both natural and anthropogenic factors. Their results classified the Braies hillslopes as having a medium to high risk of failure. Steger et al. (2023) expanded the regional-scale analysis by applying a generalized additive mixed model to produce continuous probability scores for landslide occurrence in Alto Adige. Based on a filtered data set of 2,832 events over 21 years and gridded daily precipitation data, they assessed the influence of short-term triggering rainfall, medium-term preparatory rainfall, and seasonal effects on slope failure. In our case, during the Braies August 5th-6th, 2017 event, the recorded 58.4 mm of cumulative rainfall (and 171.2 mm of antecedent rainfall over the previous 28 days) exceeds the threshold for landslide initiation defined in their study. Building on this approach, Moreno et al. (2023) integrated static ground conditions with dynamic precipitation triggers to improve landslide prediction across Alto Adige. Their model identified an optimal combination of rainfall conditions for triggering shallow landslides, around 63 mm of preparatory rainfall over two weeks, followed by approximately 50 mm of triggering rainfall. By applying these thresholds, the Braies subcatchments showed a high probability of failure (0.7-0.8) in their study. These values are matching the rainfall records of August 5th-6th, 2017 event (63.1 mm antecedent and 58.4 mm triggering rainfall).

Statistical and data-driven models are valuable tools for assessing landslide hazards at a regional/catchment scale, particularly in areas where detailed geotechnical data are limited. However, these models rely heavily on the quality and completeness of landslide inventories and often simplify the underlying physical processes. In contrast, the physically based framework applied in this study incorporates the dynamic hydrological and mechanical conditions that govern slope stability, allowing for a more mechanistic understanding of landslide triggering at the hillslope scale. The findings from the previously cited studies support our results, suggesting that the numerical models used, and the hypothesis made on soil depth and hydromechanical parameters are reasonable assumptions for assessing shallow landslide occurrence in the Braies hillslopes. Our physically based approach is thus complementary to statistical models, as it enhances the understanding of local failure mechanisms, guide targeted interventions, and emphasizes the importance of field data collection for monitoring potential high-risk areas.

3.5.4 Limitations

Despite the successful simulation of Alto Adige landslide timing and location, the accuracy of our analysis could be enhanced by addressing several limitations related to hydrogeological data availability and modeling approaches.

The SWRC parameters were derived from hydraulic data sets of 250-m coarse spatial resolution. The saturated hydraulic conductivity values obtained from SoilGrids are consistent with values reported in the literature for comparable soil textures. The selected value of $k_s = 6.2 \cdot 10^{-3}$ mm/s aligns with the SoilKsatDB global database (Gupta et al. 2021), which reports typical values of approximately $k_s = 5 \cdot 10^{-3}$ mm/s for loam to silt loam soils, corresponding to the predominant soil textural classes on the Braies hillslopes, as identified in the ESDAC soil properties maps. However, field measurements by Sanzeni et al. (2019) in Val Venosta (Alto-Adige) indicate a broader range of $k_s = [10^{-3}; 1]$ mm/s, suggesting that local soils may exhibit higher conductivities and potentially a decrease in conductivity with depth. These discrepancies highlight the importance of local field measurements. Nonetheless, in the absence of site-specific data, the use of a spatially constant k_s value from SoilGrids remains a plausible choice for regional-scale hydrological modeling, while acknowledging the associated uncertainties.

Regarding the bedrock layer, we lack direct data on its hydraulic properties, depth, fracture density, or the extent of weathering. This is a critical gap, as weathered bedrock significantly influences subsurface storage, streamflow generation, and lateral water movement. Ideally, observations of water table fluctuations and porosity profiles would allow estimation of the weathered bedrock thickness through application of topographic models such as that proposed by Rempe and Dietrich (2014). In our case, we assume a single-layer bedrock with hydraulic parameters derived from the k_s values available in the SoilGrids data set (at 2 m depth), representing an indicative depth for the soil-to-weathered bedrock transition. For example, Moser and Hohensinn (1983) conducted a detailed study of rainfall-induced slope movements in Eastern Tyrol, Austria (near the present case study site) finding that most failures occurred in hillside cover soils at depths of only 1 to 2 meters. Specifically, the value of $k_s = 6.5 \cdot 10^{-5}$ mm/s used here is within the expected range for moderately fractured dolomitic rock formations, based on standard references.

To improve soil depth estimations in our model, direct field measurements are essential. These would help us identify potential patterns or depth decay across different slope ranges, and define an upper threshold beyond which bedrock outcrops and soil depth is zero. In our simulations, we modeled landslides over hillslope profiles with slopes ranging from 20° to 50°. Within this range, the theoretical model produces estimates consistent with field measurements from other sites in Alto Adige (e.g., Sanzeni et al. 2019). Only in Case 4 did we encounter unusually steep slopes beyond the range of our profiles. In such extreme cases (>60°-70°), is very likely that steep topographic gradients primarily enhance surface runoff rather than promote infiltration to saturate and weaken the soil.

Another important limitation is the coupling of a 3-D hydrological model with a 2-D mechanical stress model. While the 3-D hydrological model effectively captures complex flow pathways, spatial variability in saturation and water accumulation zones, the 2-D mechanical model simplifies these dynamics into a single profile, potentially biasing stress distributions and failure zones, particularly in geologically complex terrains. Furthermore, lateral effects that are significant in real-world slope stability may be overlooked in the 2-D framework. Nonetheless, this hybrid approach provides computational advantages: it allows detailed hydrological analysis to be maintained while simplifying mechanical computations, making the model more suitable for large-scale or long-term simulations.

3.6 Conclusions

This study presented a physics-based hydro-mechanical framework for assessing hillslope stability, demonstrated through two different applications. In the first, the model was validated by simulating shallow landslide initiation on a homogeneous hillslope. The results reproduced the findings of Lu et al. (2019), revealing instability occur after 3 hours at the crest, which then propagated downslope toward the toe. The second application focused on a real-world scenario in the Alto Adige region, incorporating greater complexity by modeling two contrasting layers (soil+bedrock) with significantly different hydraulic and mechanical properties. The model effectively captured failure initiation during the storm event, with failure surfaces forming approximately parallel to the ground at the soil-bedrock interface.

The methodology presented in this work, along with the modeling framework, demonstrates strong potential for broader application due to its basis in open data. The stability analysis performed can be extended to other catchments in the North-Eastern Italian Alps, that share the key hydro-geomorphological features of the Dolomitic landscape, but also can be applied in any other scenario. However, soil parametrization from both hydrological and mechanical perspectives varies significantly between sites and requires the user to have knowledge of local geotechnical, hydrological, and geomorphological conditions to be effective.

Further improvements in the accuracy and validation of our results within the Alto Adige region could be achieved by: (1) collecting soil samples, (2) conducting in-situ and laboratory tests to estimate hydro-mechanical parameters and characterize the soil-bedrock profile, and (3) measuring hydrologic variables such as pore water pressure and water content. Despite these limitations, we were able to predict the location and timing of landslide initiation with precision. The models offer a practical approach to evaluating subsurface flow and mechanical stability of hillslopes under variably saturated conditions, applicable from basic laboratory experiments to complex real-world scenarios.

Data Availability Statement

All data and models generated or used during this study appear in the published article. The hydrologic model (GEOtop) is available on GitHub: https://github.com/geotopmodel/geotop.

Acknowledgments

The authors would like to thank the University of Trento (https://www.unitn.it/it) for providing the computational resources and the Agenzia per la Protezione Civile (https://home.provincia.bz.it/it/contatti/7596), in particular, the Ufficio Centro Funzionale Provinciale (corresponding contact, Omar Formaggioni), for providing access to the landslide data necessary to this study.

Author Contributions

Riccardo Busti: Data curation; Formal analysis; Methodology; Software; Visualization; Writing - original draft. Giuseppe Formetta: Conceptualization; Data curation; Formal analysis; Funding acquisition; Investigation; Methodology; Resources; Software; Supervision; Validation; Writing - review and editing. Ning Lu: Investigation; Methodology; Supervision; Writing - review and editing.

References

Abbasov, R., Fahs, M., Younes, A., Nowamooz, H., Måløy, K. N., and Toussaint, R. (2024). Modeling rainfall-induced landslide using the concept of local factor of safety: Uncertainty propagation and sensitivity analysis. Comput. Geotech. 167 (Mar): 106102.

Alvioli, M., Melillo, M., Guzzetti, F., Rossi, M., Palazzi, E., von Hardenberg, J., Brunetti, M. T., and Peruccacci, S. (2018). Implications of climate change on landslide hazard in central Italy. Sci. Total Environ. 630 (Jul): 1528-1543.

Arnone, E., Dialynas, Y. G., Noto, L. V., and Bras, R. L. (2016). Accounting for soil parameter uncertainty in a physically based and distributed approach for rainfall-triggered landslides. Hydrol. Processes 30 (6): 927-944.

Arnone, E., Francipane, A., Dialynas, Y. G., Noto, L. V., and Bras, R. L. (2021). Implications of terrain resolution on modeling rainfall-triggered landslides using a TIN-based model. Environ. Modell. Software 141 (Jul): 105067.

Bell, F. G. (2007). Engineering geology. Burlington, MA: ButterworthHeinemann.

Bertoldi, G., Rigon, R., and Over, T. M. (2006). Impact of watershed geomorphic characteristics on the energy and water budgets. J. Hydrometeorol. 7 (3): 389-403.

Binley, A. B., and Beven, K. J. (1992). Three-dimensional modeling of hillslope hydrology. Hydrol. Processes 6 (3): 347-359.

Bishop, A. W. (1955). The use of the slip circle in the stability analysis of slopes. Géotechnique 5 (1): 7-17.

Borga, M., Dalla Fontana, G., Da Ros, D., and Marchi, L. (1998). Shallow landslide hazard assessment using a physically based model and digital elevation data. Environ. Geol. 35 (2): 81-88.

Borja, R., and White, J. (2010). Continuum deformation and stability analyses of a steep hillside slope under rainfall infiltration. Acta Geotech. 5 (1): 1-14.

Borja, R. I., Liu, X., and White, J. A. (2012). Multiphysics hillslope processes triggering landslide. Acta Geotechnica 7 (Dec): 261-269.

Borrelli, L., Ciurleo, M., and Gullà, G. (2018). Shallow landslide susceptibility assessment in granitic rocks using GIS-based statistical methods: The contribution of the weathering grade map. Landslides 15 (6): 1127-1142.

Bozzolan, E., Holcombe, E., Pianosi, F., and Wagener, T. (2020). Including informal housing in slope stability analysis—An application to a datascarce location in the humid tropics. Nat. Hazards Earth Syst. Sci. 20 (11): 3161-3177.

Busti, R., Capparelli, G., and Formetta, G. (2024). Exploring hydrologic dynamics of layered pyroclastic soils by combining laboratory and field experiments with a numerical model. Hydrol. Processes 38 (8): e15257.

Calvello, M. (2017). Early warning strategies to cope with landslide risk. Riv. Ital. Geotecnica 2 (17): 63-91.

Capparelli, G., and Versace, P. (2014). Analysis of landslide triggering conditions in the Sarno area using a physically based model. Hydrol. Earth Syst. Sci. 18 (8): 3225-3237.

Chen, P., Lu, N., Formetta, G., Godt, J., and Wayllace, A. (2018). Tropical storm-induced landslide potential using combined field monitoring and numerical modeling. J. Geotech. Geoenviron. Eng. 144 (11): 05018002.

Ciabatta, L., Camici, S., Brocca, L., Francesco, P., Stelluti, M., Berni, N., and Moramarco, T. (2016). Assessing the impact of climate-change scenarios on landslide occurrence in Umbria Region, Italy. J. Hydrol. 541 (Oct): 285-295.

Crozier, M. (2010). Deciphering the effect of climate change on landslide activity: A review. Geomorphology 124 (3): 260-267.

Dall'Amico, M., Endrizzi, S., Gruber, S., and Rigon, R. (2011). An energyconserving model of freezing variably-saturated soil. Cryosphere 5 (2): 469-484.

Del Soldato, M., Pazzi, V., Segoni, S., De Vita, P., Tofani, V., and Moretti, S. (2018). Spatial modeling of pyroclastic cover deposit thickness (depth to bedrock) in peri-volcanic areas of Campania (Southern Italy). Earth Surf. Proceses Landforms 43 (9): 1757-1767.

Ebel, B. A., Loague, K., Vanderkwaak, J. E., Dietrich, W. E., Montgomery, D. R., Torres, R., and Anderson, S. P. (2007). Near-surface hydrologic response for a steep, unchanneled catchment near Coos Nay, Oregon: 2. Physics-based simulations. Am. J. Sci. 307 (4): 709-748.

Eberhardt, E., Stead, D., and Coggan, J. S. (2004). Numerical analysis of initiation and progressive failure in natural rock slopes: The 1991 Randa rockslide. Int. J. Rock Mech. Min. Sci. 41 (1): 69-87.

Endrizzi, S., Gruber, S., Dall'Amico, M., and Rigon, R. (2014). GEOtop 2.0: Simulating the combined energy and water balance at and below the land surface accounting for soil freezing, snow cover and terrain effects. Geosci. Model Dev. 7 (6): 2831-2857.

Endrizzi, S., and Marsh, P. (2010). Observations and modeling of turbulent fluxes during melt at the shrub-tundra transition zone 1: Point scale variations. Hydrol. Res. 41 (6): 471-491.

Fellenius, W. (1936). Calculation of the stability of earth dams. Transactions second congress on large dams, 445-462. Washington, DC: United States Government Printing Office.

Formetta, G., and Capparelli, G. (2019). Quantifying the three-dimensional effects of anisotropic soil horizons on hillslope hydrology and stability. J. Hydrol. 570 (Mar): 329-342.

Formetta, G., Capparelli, G., David, O., Green, T., and Rigon, R. (2016a). Integration of a three-dimensional process-based hydrologic model into the object modeling system. Water 8 (1): 12.

Formetta, G., Simoni, S., Godt, J. W., Lu, N., and Rigon, R. (2016b). Geomorphological control on variably saturated hillslope hydrology and slope instability. Water Resour. Res. 52 (6): 4590-4607.

Fredlund, D. G., and Krahn, J. (1977). Comparison of slope stability methods of analysis. Can. Geotech. J. 14 (3): 429-439.

Froude, M. J., and Petley, D. N. (2018). Global fatal landslide occurrence from 2004 to 2016. Nat. Hazards Earth Syst. Sci. 18 (8): 2161-2181.

Gariano, S., and Guzzetti, F. (2016). Landslides in a changing climate. Earth Sci. Rev. 162 (Nov): 227-252.

Godt, J. W., Baum, R. L., Savage, W. Z., Salciarini, D., Schulz, W. H., and Harp, E. L. (2008). Transient deterministic shallow landslide modeling: Requirements for susceptibility and hazard assessments in a GIS framework. Eng. Geol. 102 (3-4): 214-226.

Greco, R., Marino, P., and Bogaard, T. A. (2023). Recent advancements of landslide hydrology. WIREs Water 10 (6): e1675.

Griffiths, D. V., and Lane, P. A. (1999). Slope stability analysis by finite elements. Géotechnique 49 (3): 387-403.

Gubler, S., Endrizzi, S., Gruber, S., and Purves, R. S. (2013). Sensitivities and uncertainties of modeled ground temperatures in mountain environments. Geosci. Model Dev. 6 (4): 1319-1336.

Gupta, S., Hengl, T., Lehmann, P., Bonetti, S., and Or, D. (2021). SoilKsatDB: Global database of soil saturated hydraulic conductivity measurements for geoscience applications. Earth Syst. Sci. Data 13 (4): 1593-1612.

Haque, U., et al. (2019). The human cost of global warming: Deadly landslides and their triggers (1995-2014). Sci. Total Environ. 682 (Sep): 673-684.

Hengl, T., et al. (2017). SoilGrids250m: Global gridded soil information based on machine learning. PLoS One 12 (2): e0169748.

Hungr, O., Eberhardt, E., and Corominas, J. (2005). Estimating landslide motion mechanism, travel distance and velocity. In Landslide risk management, 99-128. London: CRC Press.

Irmler, R., Daut, G., and Mausbacher, R. (2006). A debris flow calendar derived from sediments of lake Lago di Braies (N. Italy). Geomorphology 77 (1-2): 69-78.

ISPRA (Istituto Superiore per la Protezione e la Ricerca Ambientale). (2021). IFFI—Inventario dei fenomeni franosi in Italia. Accessed January 14, 2025.

Iverson, R. M., and Reid, M. E. (1992). Gravity-driven groundwater flow and slope failure potential 1. Elastic effective-stress model. Water Resour. Res. 28 (3): 925-938.

Iverson, R. M., and Reid, M. E. (1997). Debris-flow mobilization from landslides. Annu. Rev. Earth Planet. Sci. 25 (1): 85-138.

Janbu, N. (1973). Slope stability computations. In Embankmentdam engineering: Casagrande volume, 47-86. New York: Wiley.

Keijsers, J. G. S., Schoorl, J. M., Chang, K. T., Chiang, S. H., Claessens, L., and Veldkamp, A. (2011). Calibration and resolution effects on model performance for predicting shallow landslide locations in Taiwan. Geomorphology 133 (3-4): 168-177.

Lanni, C., Borga, M., Rigon, R., and Tarolli, P. (2012). Modelling shallow landslide susceptibility by means of a subsurface flow path connectivity index and estimates of soil depth spatial distribution. Hydrol. Earth Syst. Sci. 16 (11): 3959-3971.

Lu, N., and Godt, J. W. (2013). Hillslope hydrology and stability. New York: Cambridge University Press.

Lu, N., Godt, J. W., and Wu, D. T. (2010). A closed-form equation for effective stress in unsaturated soil. Water Resour. Res. 46 (5): W05515.

Lu, N., and Likos, W. J. (2006). Suction stress characteristic curve for unsaturated soil. J. Geotech. Geoenviron. Eng. 132 (2): 131-142.

Lu, N., Sener-Kaya, B., Wayllace, A., and Godt, J. W. (2012). Analysis of rainfall-induced slope instability using a field of local factor of safety. Water Resour. Res. 48 (9): W09524.

Lu, N., Wayllace, A., and Chen, P. (2019). The slope stress and stability (Slope Cube) module for HYDRUS (3D): Simulating slope stress and stability in variably-saturated soils, hydrus software series 3.02.0290, PC-Progress. Madison, WI: Soil Water Retention, LLC. PC-Progress.

Mathews, N. W., Leshchinsky, B. A., Mirus, B. B., Olsen, M. J., and Booth, A. M. (2024). RegionGrow3D: A deterministic analysis for characterizing discrete three-dimensional landslide source areas on a regional scale. J. Geophys. Res. Earth Surf. 129 (9): e2024JF007815.

MeteoBrowser. (2025). Meteo browser Alto Adige. Accessed January 9, 2025.

Montgomery, D. R., and Dietrich, W. E. (1994). A physically-based model for topographic control on shallow landsliding. Water Resour. Res. 30 (4): 1153-1171.

Moradi, S., Huisman, J. A., Class, H., and Vereecken, H. (2018). The effect of bedrock topography on timing and location of landslide initiation using the local factor of safety concept. Water 10 (10): 1290.

Morar, C., Lukic, T., Basarin, B., Valjarevic, A., Vujicic, M., Niemets, L., Telebienieva, I., Boros, L., and Nagy, G. (2021). Shaping sustainable urban environments by addressing the hydro-meteorological factors in landslide occurrence: Ciuperca hill (Oradea, Romania). Int. J. Environ. Res. Public Health 18 (9): 5022.

Moreno, M., Lombardo, L., Crespi, A., Zellner, P. J., Mair, V., Pittore, M., van Westen, C., and Steger, S. (2023). Space-time data-driven modeling of precipitation-induced shallow landslides in South Tyrol, Italy. Sci. Total Environ. 912 (Feb): 169166.

Morgenstern, N. R., and Price, V. E. (1965). The analysis of the stability of general slip surfaces. Géotechnique 15 (1): 79-93.

Moser, M., and Hohensinn, F. (1983). Geotechnical aspects of soil slips in alpine regions. Eng. Geol. 19 (3): 185-211.

Mualem, Y. (1976). New model for predicting hydraulic conductivity of unsaturated porous-media. Water Resour. Res. 12 (3): 513-522.

Paronuzzi, P., and Bolla, A. (2023). Rainfall infiltration and slope stability of alpine colluvial terraces subject to storms (NE Italy). Eng. Geol. 323 (Sep): 107199.

Patton, A. I., Luna, L. V., Roering, J. J., Jacobs, A., Korup, O., and Mirus, B. B. (2023). Landslide initiation thresholds in data-sparse regions: Application to landslide early warning criteria in Sitka, Alaska, USA. Nat. Hazards Earth Syst. Sci. 23 (10): 3261-3284.

Paudel, U., Oguchi, T., and Hayakawa, Y. (2016). Multi-resolution landslide susceptibility analysis using a DEM and random forest. Int. J. Geosci. 7 (5): 726-743.

Petrovic, N., Bozic, B., and Lukic, I. (2018). Climate changes and landslide hazard. Ann. Disaster Risk Sci. 1 (1): 3-18.

Piacentini, D., Troiani, F., Soldati, M., Notarnicola, C., Savelli, D., Schneiderbauer, S., and Strada, C. (2012). Statistical analysis for assessing shallow-landslide susceptibility in South Tyrol (South-Eastern Alps, Italy). Geomorphology 151-152 (May): 196-206.

Reddy, J. N. (1985). An introduction to the finite element method. New York: McGraw-Hill.

Rempe, D. M., and Dietrich, W. E. (2014). A bottom-up control on freshbedrock topography under landscapes. Proc. Natl. Acad. Sci. U.S.A. 111 (18): 6576-6581.

Rigon, R., Bertoldi, G., and Over, T. (2006). Geotop: A distributed hydrologic model with coupled water and energy budgets. J. Hydrometeorol. 7 (3): 371-388.

Rosso, R., Rulli, M. C., and Vannucchi, G. (2006). A physically based model for the hydrologic control on shallow landsliding. Water Resour. Res. 42 (6): W06410.

Sanzeni, A., Peli, M., Barontini, S., and Colleselli, F. (2019). Modelling of an accidentally triggered shallow landslide in Northern Italy. Landslides 16 (11): 2277-2286.

Schlögel, R., Kofler, C., Gariano, S. L., Van Campenhout, J., and Plummer, S. (2020). Changes in climate patterns and their association to natural hazard distribution in South Tyrol (Eastern Italian Alps). Sci. Rep. 10 (1): 5022.

Scorpio, V., Cavalli, M., Steger, S., Crema, S., Marra, F., Zaramella, M., Borga, M., Marchi, L., and Comiti, F. (2022). Storm characteristics dictate sediment dynamics and geomorphic changes in mountain channels: A case study in the Italian Alps. Geomorphology 403: 108173.

Shao, W., Bogaard, T. A., Bakker, M., and Greco, R. (2015). Quantification of the influence of preferential flow on slope stability using a numerical modelling approach. Hydrol. Earth Syst. Sci. 19 (5): 2197-2212.

Simoni, S., Zanotti, F., Bertoldi, G., and Rigon, R. (2008). Modelling the probability of occurrence of shallow landslides and channelized debris flows using GEOtop-FS. Hydrol. Processes 22 (4): 532-545.

Sorbino, G., Sica, C., and Cascini, L. (2009). Susceptibility analysis of shallow landslides source areas using physically based models. Nat. Hazard. 53 (2): 313-332.

Steger, S., et al. (2023). Deciphering seasonal effects of triggering and preparatory precipitation for improved shallow landslide prediction using generalized additive mixed models. Nat. Hazards Earth Syst. Sci. 23 (4): 1483-1506.

Stoffel, M., Tiranti, D., and Huggel, C. (2014). Climate change impacts on mass movements—Case studies from the European Alps. Sci. Total Environ. 493 (Sep): 1255-1266.

Tarolli, P., and Tarboton, D. G. (2006). A new method for determination of most likely landslide initiation points and the evaluation of digital terrain model scale in terrain stability mapping. Hydrol. Earth Syst. Sci. 10 (5): 663-677.

Toth, B., Weynants, M., Pasztor, L., and Hengl, T. (2017). 3D soil hydraulic database of Europe at 250 m resolution. Hydrol. Processes 31: 2662- 2666.

Tufano, R., Formetta, G., Calcaterra, D., and De Vita, P. (2021). Hydrologic control of soil thickness spatial variability on the initiation of rainfallinduced shallow landslides using a three-dimensional model. Landslides 18 (10): 3367-3380.

Tyagi, A., Kamal Tiwari, R., and James, N. (2022). A review on spatial, temporal and magnitude prediction of landslide hazard. J. Asian Earth Sci.: X 7 (Jun): 100099.

Van Genuchten, M. T. (1980). A closed-form equation for predicting the hydraulic conductivity of unsaturated soils. Soil Sci. Soc. Am. J. 44 (5): 892-898.

Viet, T. T., Lee, G., Thu, T. M., and An, H. U. (2016). Effect of digital elevation model resolution on shallow landslide modeling using TRIGRS. Nat. Hazard. Rev. 18 (2): 04016011.

WEBGIS Bolzano. (2025). GeoBrowser MapView. Accessed January 9, 2025.

Wu, W., and Sidle, R. C. (1995). A distributed slope stability model for steep forested basins. Water Resour. 31 (8): 2097-2110.

Yang, Y. S., Yeh, H. F., Ke, C. C., Chen, N. C., and Chang, K. C. (2022). Assessment of probability of failure on rainfall-induced shallow landslides at slope scale using a physical-based model and fuzzy point estimate method. Front. Earth Sci. 10 (Sep): 957506.

Chapter 4: Surface and Subsurface Hydrological Responses to Different Critical Zone Geometries on Steep Hillslopes

Giuseppe Formetta[1], Riccardo Busti[1], Justin T. Higa[2], Dino G. Bellugi[3], Brian A. Ebel[4], William E. Dietrich[3,5], David G. Milledge[6], and Seulgi Moon[2]

[1]Department of Civil, Environmental and Mechanical Engineering (DICAM), University of Trento, Trento (TN), Italy

[2]University of California Los Angeles, Department of Earth, Planetary, and Space Sciences, Los Angeles, CA, United States of America

[3]University of California, Berkeley, Department of Geography, Berkeley, CA, United States of America

[4]U.S. Geological Survey, Water Mission Area, Burlington, VT, United States of America

[5]University of California, Berkeley, Department of Earth and Planetary Science, Berkeley, CA, United States of America

[6]School of Engineering, Newcastle University, Newcastle upon Tyne, United Kingdom

This article advances understanding hydrological response of different Critical Zone structures of steep hillslopes.

The article is currently under review.

Abstract

The structure and depth of the critical zone (CZ) significantly influence how water is stored on hillslopes, the paths of underground flow, and how rainfall can trigger landslides. However, many hydrological and slope-stability models still use simplified scenarios of shallow soils above impermeable bedrock, and they ignore the impact of CZ structure. This study looks at how different three-dimensional CZ shapes affect underground water response on a steep forested hillslope. Four different CZ architectures are explored, ranging from soil-only to more complex shapes with weathered bedrock at the well-monitored CB1 catchment in the Oregon Coast Range. 3D hydrological simulations are performed with GEOtop for a controlled sprinkling experiment and a storm that triggered a landslide. Results are compared with an extensive dataset that includes weir discharge records, and measurements from tensiometers and piezometers. Model performance is assessed by looking at pressure responses, discharge patterns, saturation patterns, and the directions of seepage at the soil-bedrock interface. The results show that CZ structure significantly affects how water is distributed between shallow soils and deeper weathered bedrock. It also influences the formation and connection of temporary saturated zones driving subsurface runoff production and slope instability.

4.1 Introduction

The Critical Zone (CZ) structure, from the vegetation canopy to the base of permeable bedrock, plays a significant role in subsurface hydrological processes (e.g., Lin, 2010; Wlostowski et al. 2021; Chen et al. 2024). The spatially varying material properties and structures of the CZ control hydrologic partitioning and water cycle dynamics (e.g., Brooks et al. 2015; Chorover et al. 2017), and therefore affect locations and timings of hydrologically driven natural hazards (e.g., landslides, debris flows, floods). The quantification of water stored in the deep CZ (e.g., fractured or weathered bedrock) and its exchange with soil has long been (e.g., Tsukamoto et al.1982; Wilson and Dietrich,1987; Gabrielli et al. 2012), and continues to be, an open question in hydrological research and impacts a variety of fields. It plays a crucial role not only in streamflow and runoff production (e.g., Dwivedi et al. 2019; Singha and Navarre-Sitchler, 2021), but also in landslide initiation (e.g., Regmi et al. 2015; Moon et al. under review), and drought onset, for example, by regulating the amount of plant-available water (e.g., Rempe and Dietrich, 2018; Pedrazas et al. 2021) and evapotranspiration (e.g., Hahm et al. 2022a; Hahm et al. 2022b).

Traditional hydrological theories placed soil at the center of water movement and availability, emphasizing its hydraulic properties as primary drivers of hydrological processes. Research in critical zone science reveals that in many upland regions, where soil layers are thin, plants tap into moisture stored in weathered bedrock, so-called “rock moisture”, as a crucial water source for transpiration and survival (Lapides et al. 2024). Despite its significance, this bedrock-stored water remains largely unrepresented in most earth system models. Additionally, many of these models still adopt overly simplistic representations of land hydrology, typically modeling water flow as one-dimensional, constant shallow (2-3 m), and free-drainage boundary conditions. Other simplified assumptions consist of impermeable bedrock, parallel to the topographic surface. In certain cases, these assumptions could be too simplistic, given that the bedrock could be permeable and could accommodate deep infiltration or exfiltration and that bedrock geometry may create localized hot spots of pore-water pressure and water exfiltration (e.g., Wilson and Dietrich, 1987). Fan et al. 2019 concluded that this simplified hypothesis often fails to capture key processes such as lateral, ridge-to-valley flow and insolation-driven energy contrasts between sunny and shady slopes, both of which strongly influence vegetation patterns and water dynamics within landscapes.

The dynamic moisture content of the root zone also controls the partitioning of rainfall into groundwater recharge or plant water uptake (Hahm et al. 2022). Yet quantifying groundwater recharge remains challenging: direct observations via boreholes are sparse, and models require poorly constrained parameters like bedrock hydraulic conductivity (e.g., Jasechko et al. 2014). To address these limitations, new simplified modeling approaches such as inferring recharge from streamflow dynamics have been proposed, such as analyzing the storage, discharge relationship at the catchment scale. This can provide a simple and integrated signal of water storage and groundwater recharge dynamics (Dralle et al. 2023; Kirchner, 2009). Finally, recent continental-scale studies show that deep groundwater, originating from depths of 10 to 100 meters below the surface, contributes significantly to baseflow in many river systems, challenging traditional water balance approaches that often ignore such deep flow paths (Yang et al. 2025). Together, these findings call for a paradigm shift in how hydrological processes are conceptualized and modeled, that moves beyond static soil properties and embraces the dynamic, three-dimensional interactions between climate, vegetation, and subsurface structure.

When modeling transient hydrologic processes within the subsurface, it is crucial to consider information and constraints related to geologic critical zones, such as spatial variations in soil depth and weathered bedrock thickness. Several observational studies have pointed out that subsurface water flow exfiltrating from underlying weathered bedrock to soil is an important hydrological process, which may in turn trigger natural hazards such as shallow landslides (e.g., Montgomery et al. 2002; Liang, 2020; Li et al. 2016; Brönnimann et al. 2013). In addition, much evidence has been presented of the so-called fill-and-spill runoff generation process (e.g., Tromp-van Meerveld and McDonnell, 2006; Weiler et al. 2006; McDonnell et al. 2021), i.e., the fact that during storm events, transient subsurface lateral flow fills up local depressions in the soil-bedrock interface surface, and only after certain precipitation thresholds do these transient saturated areas become connected and produce significantly substantially greater subsurface storm flow contributions to streamflow generation.

Despite the importance of the deep CZ, the structures (i.e., the geometry) and the parameterization (i.e., hydrological and geological parameters) of the deep CZ below the soil layer are largely unknown due to limited available information and quantitative measurements. To improve our understanding of the CZ structure's impact on the pore water pressure and the hydrologic response to precipitation events, comprehensive field measurements (i.e., piezometric response, unsaturated pore water pressure, and soil water content measurements) detailing the hydrologic response within the soil or deep CZ, as well as discharge data, are critical. Such data, despite their inherent value for the investigation of subsurface hydrology, pose a significant challenge to acquire due to the inherent difficulties of monitoring these subsurface processes over extended periods and across large areas. In addition, there are limited studies incorporating spatially varying CZ layers based on direct observations due to the high economic costs (e.g., drilling) and technological challenges, as the CZ can be highly heterogeneous and thick (tens of meters) (e.g., Burke et al. 2007). Large efforts have been made by the scientific community to build and extend CZ observatory networks (e.g., Wilson and Dietrich, 1987, Guo and Lin, 2016; Arora et al. 2023). Geophysical techniques have been applied to infer CZ thickness and geotechnical and hydrological parameters (e.g., Holbrook et al. 2014).

There are only a few studies that combine CZ characteristics (e.g., geometry, thickness, and parameters) with hydrological models to examine their influence on hillslope hydrological fluxes (e.g., Ebel et al. 2007a, b; Brantley et al. 2017) or shallow landslide initiations (e.g., Moon et al. (under review)).

Only a few locations offer such a detailed dataset of hydrological variables measured within the CZ and hydrologic model implementation and validation such as Critical zone Observatories (e.g., White et al. 2015). One of those extensively studied sites is the CB1 experimental catchment near Coos Bay, Oregon. Intensive field measurements documented soil and bedrock moisture and groundwater dynamics through the CZ (Anderson et al. 1997a; Anderson et al. 1997b; Montgomery et al. 1997; Torres et al. 1998; Montgomery et al.

2002). Runoff generation occurs entirely through subsurface storm flow, with no evidence of surface drainage (Anderson et al. 1997a). This is due to the high soil hydraulic conductivity that enhances infiltration. Analysis of the timescales of piezometric responses in shallow bedrock has shown a rapid response without complete soil saturation, with subsurface flow paths developing much faster than the transit time for water in the uppermost soil (e.g., Montgomery et al. 1997; Torres et al. 1998, Ebel et al. 2007a, b; Ebel and Loague, 2008). These lead to two main flow pathways: vertical percolation in the unsaturated soil and rapid saturated flow through soil and weathered bedrock (Anderson et al. 1997a). These pathways converge near the CB1 channel head creating a condition like the concept of the variable source area than in this case occurs as a subsurface variable source area, which has crucial importance in the runoff generation process over the hillslope.

Ebel et al. (2007a, b) modeled surface-subsurface hydrologic responses during sprinkling experiments on CB1 using a physics-based model of 3D variably saturated flow based on Richard's equations. The model simulated runoff at the upper weir and pore-water pressure dynamics in space and time. A single critical zone scenario was used, with soil and saprolite depths interpolated from 630 measurements, weathered bedrock thickness decreasing downslope from ~4 m at the ridge crest to near zero at the upper weir, and bedrock extending to the basal boundary. Results showed that the 3D geometry and hydraulic properties of layered geologic interfaces strongly control saturation and pore-water pressure development at the soil–saprolite boundary.

However, extensive hydrologic observations and measurements near the surface have not been fully used to compare with simulations based on varying deep critical zone structures. Furthermore, we still have limited knowledge whether or how spatially varying deep CZ structures induce measurable differences in hydrologic response and discharge near the surface.

This study aims to examine the effects of varying critical zone (CZ) structures on hillslope subsurface hydrology, with a focus on how water fluxes within the CZ influence soil and bedrock saturation and associated implications for soil water exfiltration and runoff production, focusing on the Coos Bay site. We utilize extensive field measurements, which include long-term data series (of piezometric response and discharge) and sprinkling experiments (Anderson et al. 1997a; Montgomery et al. 1997), together with i) CZ geometry scenarios constructed based on available data including topography (Ebel et al. 2007b), uplift-erosion rates (Reneau and Dietrich, 1991), borehole profile characterization (Anderson et al. 1997a) and ii) robust, physics-based numerical models of surface hydrology. We constructed four end-member CZ structures, ranging from constant, impermeable unweathered bedrock to spatially complex weathered bedrock, based on a topographic stress model. Using a three-dimensional hydrological model, we simulated coupled energy and water infiltration processes to investigate differences in subsurface soil water fluxes (intensity and directions) and potential water exfiltration patterns from bedrock to soil under two rainfall scenarios: a sprinkler experiment and a historic natural extreme rainfall event, that induced a landslide. Then, simulated model results were validated systematically against the field measurements, at multiple points in space and over multiple hydrological variables (i.e., pore-water pressure, weir discharge).

This model-data integration aims to provide a comprehensive perspective, allowing for improved knowledge of surface runoff, subsurface infiltration and exfiltration, and saturation of different CZ layers, and to provide insights into the factors influencing natural hazards onset such as flash-floods, droughts, or landslides occurrences.

4.2 Study area and data

The CB1 Experimental Catchment is a research site of 860 m2 located in the Oregon Coast Range near Mettman Ridge, situated 15 km northeast of the city of Coos Bay in Oregon, USA (Fig. 16-a). Since the early 1990s, it has served as a benchmark site for investigating CZ processes, including landscape evolution such as channel initiation and hillslope transport (e.g., Anderson et al. 1997b; Torres et al. 1998; Montgomery et al. 2002; Anderson et al. 2002; and nearby: Roering et al. 1999, Heimsath, et al. 2001; Stock and Dietrich, 2006). The site provides scientists with the opportunity to monitor hydrological, geomorphic, and biogeochemical processes at a fine scale, while considering the influence of topography, vegetation, and soil characteristics. This steep first-order hillslope (with an average slope of 43°) exhibits small-scale variability in colluvial soil depth, with an average around 1 m (Fig. 16-c). A thin saprolite layer exists between the soil and the weathered bedrock (hereafter, WB), being well-developed near the ridge crest and thinning toward the channel head where it outcrops. Above the unweathered fresh bedrock (hereafter, UB) lies fractured, slightly oxidized bedrock, with its depth decreasing downhill. Limited information regarding the spatial distribution and aperture of fractures in the bedrock at CB1 is discussed in Anderson et al. (2002) and Ebel et al. (2007b).

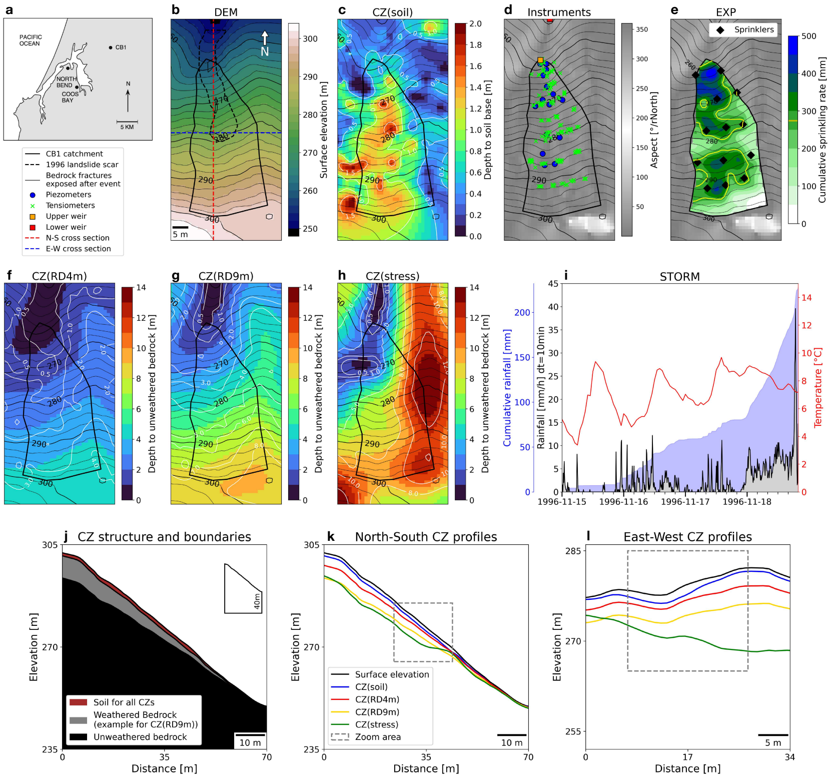

Figure 16. (a) Location map for the CB1 study area in the Oregon Coast Range (from Ebel et al. 2007a). (b) Digital elevation model with North–South (in red, profile shown in panels j and k) and East–West (in blue, profile shown in panel l) cross-sections, with CB1 boundary, 1996 landslide scar and bedrock fractures open after the event. (c) Soil thickness which is used also as CZ(soil) scenario. (d) Locations of measurement instruments: 14 piezometers, 100 tensiometers, 1 upper weir, and 1 lower weir; the grey background indicates terrain aspect, also used in subsequent figures. (e) Spatial distribution of cumulative rainfall from 13 sprinklers during Experiment 3. The yellow contour indicates the target mean cumulative rate, corresponding to a constant application rate of 1.65 mm/h and a total of 274 mm over 166 hours (Ebel et al. 2007a). (f, g, h) Depth from the surface to the unweathered bedrock and, in white contours,

thickness of weathered bedrock for the CZ(RD4m), CZ(RD9m), and CZ(stress) scenarios, respectively. (i) Rainfall intensity during the November 1996 storm (black line filled in grey) and air temperature (red line). The blue shaded area represents cumulative rainfall from 00:00 on November 15th to 20:00 on November 18th, 1996. (j) North-South view of each layer with an inset on the top-right position showing a schematic view of the full computational domain. (k) N-S and (l) E-W cross section showing the depth of the CZ structure in each scenario. The grey dashed zoom areas in these panels show the extent of the cross section visualized in Fig. 7 and in the supplementary material Fig. S5 to S8. Bottom left corner maps coordinates are (x,y)=(410002,4812902.5) in EPSG:26910 reference system.

A high-density network of instruments was deployed to monitor and understand the near-surface hydrologic response during sprinkling experiments conducted from 1990 to 1992 (e.g., Montgomery et al. 2002; Ebel et al. 2007a). This network captured high-resolution data regarding various hydrological quantities, including piezometer and tensiometer measurements, runoff generation, rainfall intensity and distribution, and water chemistry. Records were acquired from 148 manual rain gauges, three automated tipping-bucket rain gauges, 223 piezometers (28 of which were installed into bedrock and 42 of which were equipped with pressure transducers), and 100 soil-buried tensiometers during a three-year field monitoring period (Ebel et al. 2007a; Ebel et al. 2007b; Ebel et al. 2008; Montgomery et al. 2009). Discharge at CB1 was monitored at two V-notch weirs located at the basin outlet and anchored to bedrock (Fig. 16-d). The two weirs, named “Upper weir” (UW) and “Lower weir” (LW) have been installed to catch the subsurface flow from soil and WB respectively, because during the experiments the researchers realized that much of the subsurface was not emerging at the spring upslope of the first weir, instead water traveled subsurface another ~15 m and was captured in a second weir (e.g., Montgomery et al. 2002). Hence, these studies have identified several hydrological mechanisms underlying the CB1 hydrological behavior, such as: i) the soil-water retention properties led to rapid unsaturated zone response once the soil was wet, and a rapid rise in the saturated zone; ii) nearly all of the infiltrating rainwater entered the underlying saprolite and weathered bedrock layers and returned locally to soil, creating spatially discontinuous patterns of positive pore water pressure in the soil; iii) upward head gradients were generated from the saprolite and weathered bedrock during high-intensity rainfall, generating runoff mainly through fracture zones

(Anderson et al. 1997a,b; Montgomery et al. 2002; Montgomery and Dietrich, 2002; Torres et al. 1998; Ebel et al. 2007a).

In this work, we analyze two rainfall events: a sprinkling experiment carried out in May-June 1992 (Experiment 3 in Ebel et al. 2007a; Montgomery et al. 1997; Montgomery et al. 2002) and the intense natural rainfall event that triggered the CB1 landslide in 1996 (Montgomery et al. 2009).

The sprinkling experiment (hereafter, EXP) lasted for six days from May 27th to June 3rd, 1992. Initially designed with a constant application rainfall rate of 1.65 mm/h for a total of 274 mm over 166 hours, it resulted in spatially varying rainfall across CB1 from the 13 installed sprinklers (Fig. 16-e, Ebel et al. 2007a). During EXP, fluctuations in pore water pressure were measured in the 100 tensiometers, and discharge data from colluvial soil were collected at the two weirs (Fig. 16-d).

The intense storm (hereafter, STORM), occurred in November 1996 (Fig. 16-i), triggered a shallow landslide at the CB1 site (Fig. 16-b, Montgomery et al. 2009). During November 16th-18th, 1996, rain gauges at CB1 measured a total of 225 mm of rain with a momentary peak of ~40 mm/h at 18:50, a maximum daily intensity of 145 mm/day and a 48-hour average intensity of 85 mm/day (Montgomery et al. 2009). The event culminated in the slope's failure: a shallow landslide occurred between 19:50-20:00 on November 18th, destroying a large part of the site's instrumentation. The debris flow excavated colluvial soil to the bedrock surface over the upper portion of the scar. There was smooth, relatively unfractured sandstone bedrock at the base of the scar, except for three zones where large fractures produced post-failure water discharge (Fig. 16-b). These zones corresponded to the partial soil saturation observed in prior sprinkler experiments at CB1 (Montgomery et al. 2009). During the storm, measurements included pore water pressure over the soil base at the time of the landslide, collected from 15 automated piezometer nests, located in the hollow (Fig. 16-d).

4.3 Methods

4.3.1 Critical Zone Models

We adopted 4 theoretical CZ models to describe the subsurface structure of the CB1 site, similar to the approach used by Moon et al. (under review). The authors constructed diverse CZ for a large area of

Coos Bay, including the CB1 site, with varying hydrologic properties of the UB and geometries of the WB layer. We followed their approach but regenerated the grids for each CZ layer by utilizing a higher resolution DEM (from 2 m to 1 m) and dense soil thickness measurements instead of a modeled soil map. We subdivided the CZ into three layers: soil, WB (including saprolite and weathered bedrock), and UB. For our models, the depth of the soil layer (Fig. 16-c) was calculated by performing a kriging interpolation based on 195 measurements of colluvial soil depth from soil borings at CB1 (Schmidt, 1999). This soil layer was used in all four scenarios named CZ(soil), CZ(RD4m), CZ(RD9m) and CZ(stress).

The CZ(soil) has only soil directly above UB. Three scenarios, CZ(RD4m), CZ(RD9m), and CZ(stress), explore the different geometric configurations of WB, adopted from Moon et al. (under review). These scenarios have a WB layer (Fig. 16-f,g,h) between the soil and UB layers, whose geometries differ based on bedrock weathering models (Rempe and Dietrich, 2014; St. Clair et al. 2015). These models were calibrated based on field observations from CB1 shallow and deep boreholes (e.g., Schmidt, 1999, Anderson et al. 2002). A detailed explanation of the approach and modeling procedures for constraining the WB is presented in Moon et al. (under review), and a relevant summary is provided below.

Two scenarios, CZ(RD4m) (Fig. 16-f) and CZ(RD9m) (Fig. 16-g), are based on the bedrock drainage model by Rempe and Dietrich (2014). They propose a WB-UB boundary based on field measurements of soil and rock properties, channel incision rates, critical slope, and hillslope length. We represent the WB with a sloping line from exposed bedrock at the channel head to hillslope with a chosen depth below the surface: CZ(RD4m) matches the 4.5 m depth of the interface between pervasively oxidized and fractured WB bedrock observed in the CB1 borehole at the ridge, while CZ(RD9m) matches the 9 m deep interface boundary of the fractured bedrock and UB (Anderson et al. 2002).

CZ(stress) (Fig. 16-h) has a modeled WB-UB boundary based on the results of a three-dimensional topographic stress model. The 3D stress field is computed as the combination of ambient tectonic compression, gravitational loading, and topographic perturbations on regional stress fields (St. Clair et al. 2015; Moon et al. 2017). We used the poly3D model (Thomas, 1993) to quantify 3D stress fields with assumed material properties (e.g., linear elastic and homogenous rock) and regional stress boundary conditions constrained from compiled in-situ measurements from the World Stress Map as an input (Heidbach et al. 2016). Based on 3D stress fields, we obtained the least compressive stress (LCS) value at 9 m depth at the CB1 borehole location (LCS =0.11 MPa). The WB-UB boundary was generated from an isosurface of LCS=0.11 MPa, assuming this value as a threshold for fracture opening and physical-chemical weathering.

4.3.2 Hydrological Modeling

The GEOtop model (Bertoldi et al. 2006; Rigon et al. 2006; Endrizzi et al. 2014) is used to simulate the 3-D coupled hydrological surface and subsurface response within the CZ. GEOtop is a fine-scale, grid-based, distributed hydrologic model used for simulating each component of the hydrological cycle. It is designed to solve the coupled energy-water balance system at and below the water surface for small watersheds. GEOtop uses a discretization of the landscape based on digital elevation data to model the effects of topography on energy exchange with the atmosphere.

The water budget accounts for both surface and subsurface hydrology: the continuity equation at the surface simulates surface hillslope flow, and the 3-D Richards equation solves the three-dimensional water flux within variably saturated soils, accurately modeling the vertical structure of soil moisture and suction dynamics in addition to lateral flux (Endrizzi et al. 2014). The soil water retention curve (SWRC, Eq. 1) and hydraulic conductivity function (HCF, Eq. 2) follow the van Genuchten-Mualem parameterization for porous media (Mualem 1976; van Genuchten 1980):

$$\theta = \begin{cases} \theta_r + \frac{\theta_s - \theta_r}{(1+|\alpha h|^n)^m}, & h < 0, m = 1 - 1/n \\ \theta_s, & h \geq 0 \end{cases} \tag{1}$$

$$k = k_s \sqrt{S} \left[1 - \left(1 - S^{\frac{1}{m}} \right)^m \right]^2, \quad S = \frac{\theta - \theta_r}{\theta_s - \theta_r} \tag{2}$$

where h [L] is the pore water pressure, θ [-] is the water content, θ_R [-] and θ_S [-] are the residual and saturated water content, k and k_S [L/T] are the unsaturated and saturated hydraulic conductivities, S [-], is the saturation degree, α[1/L] is related to the inverse of the air-entry pressure, and n [-] is a measure of pore-size distribution. The hydrologic parameters for soil, WB, and UB adopted from Ebel et al. (2007b) and Torres et al. (1998) are listed in Tab. 4. To explore the impact of hydrologically active WB, the hydrological properties of saprolite are adopted for WB in our scenarios. The CZ are analyzed under two scenarios using different order of magnitude of the UB saturated hydraulic conductivity: i) 10^{-7} m/s (referred as KS7 in Results section), corresponding to the arithmetic mean from slug tests in bedrock reported in Ebel et al. (2007b), represents a leaky UB, and ii) 10^{-10} m/s (referred as KS10 in Results section), as predicted by Rempe and Dietrich model (2014), represents a more impermeable UB. The SWRC are displayed in Fig. S9-a,b and HCF in Fig. S9-c in the Supplementary Material.

	Hydraulic parameters				
CZ layer	k_S **[m/s]**	θ_R **[-]**	θ_S **[-]**	**α [1/m]**	n **[-]**
Soil	$3.4 \cdot 10^{-3}$	0.18	0.5	18	2.8
Weathered Bedrock	$7 \cdot 10^{-5}$	0.08	0.15	4	1.25
Unweathered Bedrock	$5 \cdot 10^{-7}*, 1 \cdot 10^{-10}**$	0.08	0.12	4.3	1.25

Table 4. Van Genuchten hydraulic parameters used for the Soil Water Retention Curve (SWRC, Eq. 1) and Hydraulic Conductivity Function (HCF, Eq. 2) for each CZ layer. Parameter values are taken from Ebel et al. (2007b) and Ebel et al. (2008). The highest value for unweathered bedrock saturated conductivity (*) is from Ebel et al. (2007b), whereas the lowest value (**) is from Rempe and Dietrich (2014).

The energy balance component considers the combined energy content of water and soil, accounting for energy fluxes between soil, vegetation, and atmosphere. Net radiation is calculated considering the balance between shortwave and longwave radiation, influenced by atmospheric conditions (Endrizzi et al. 2014). It also computes actual evapotranspiration by summing evaporation from bare soil and wet vegetation, and transpiration, using a double layer structure for fluxes between vegetation and the ground (Rigon et al. 2006; Endrizzi and Marsh, 2010). In the absence of site-specific temperature records, we used the temperature measured at the closest available meteorological station (approx. 10 km) in North Bend, Coos Bay (OR), as representative of the coastal weather. The data were acquired from the NOAA Online Weather Data (US National Weather Service). The vegetation-related parameters were selected to model the characteristics of Douglas Fir seedlings at the site (Ebel et al. 2007a; Montgomery et al. 2009).

GEOtop requires a three-dimensional breakdown of the hillslope. The CB1 digital elevation model, kriged with 630 elevation measurements (Ebel et al. 2007b), was used to create a surface grid with a horizontal resolution of 1 m (Fig. 16-b). A vertically variable discretization of the subsurface was applied, featuring finer layers (0.05 m) in the upper 4 m and increasing cell size (up to 2m) with deeper depths. A bottom horizontal impermeable boundary is set 40 m depth below the lower weir (Fig. 16-j). Impermeable lateral boundaries were also defined, except at the northern face where outflow was allowed both at surface and subsurface. Initial conditions were set using a two-month spin-up period with recorded precipitation, consistent with previous studies (e.g., Ebel et al. 2007b), assuming an initial water table depth of 2 m below the surface. The boundary conditions and spin-up duration were the same for both rainfall events. All simulations are run with 10 minutes time step, the same of recorded rainfall.

4.3.3 Hydrological model post-processing and data comparison

The main outputs of the hydrological model are time-varying three-dimensional fields of pore water pressure and water content expressed as multiple maps along the vertical grid, and matrices containing the variation along the ground depth in time of a specific hydrological variable for given point coordinates. The model outputs are processed to illustrate the influence of the CZ scenarios on pressure distribution, saturation patterns, discharge, seepage flow magnitude and direction.

In EXP: i) the observed discharges at the weirs are compared against the modeled discharge, and ii) the space-time varying records (i.e., from May 27th to June 7th) from the buried 100 tensiometers against the simulations. Nash-Sutcliffe modeling efficiency (NSE, Eq. 3), mean absolute error (MAE, Eq. 4), and bias normalized by standard deviation (NBIAS, Eq. 5) are employed as goodness-of-fit (GOF) indices between observed and modeled quantities, as for other studies in CB1 (e.g., Ebel et al. 2007b):

$$NSE = 1 - \frac{\sum_{i=1}^{n}(O_i - M_i)^2}{\sum_{i=1}^{n}(O_i - \bar{O})^2} \tag{3}$$

$$MAE = \frac{\sum_{i=1}^{n}|O_i - M_i|}{n} \tag{4}$$

$$NBIAS = \frac{\sum i=1^{n} M_i - O_i}{n\sigma_o} \tag{5}$$

where $\bar{O}$ is the mean of observed data, σ_O is the standard deviation of the observed data, O_i and $M_i$are observed and modeled data at the i-th time, respectively, and n is the number of measurements. NSE ranges between minus infinity and 1. An NSE value lower than 0 means that the average of the observations is a better predictor than the model, whereas an NSE value of 1 means a perfect fit between observation and model predictions. MAE indicates, on average, how far the model's predictions are from the observed values. It does not show the direction of bias and is not normalized. To complement it, NBIAS, a bias normalized by standard deviation, is also used to specify how many standard deviations the model's mean bias is away from zero. A positive NBIAS indicates overprediction, a negative one indicates underprediction, and the magnitude reflects how far the model is from being unbiased.

In STORM the following quantities are analyzed: i) the pressure at soil base along with soil saturation ratio, ii) the subsurface flow patterns, iii) discharge at UW. The modeled and measured soil saturation ratios (h/z) are compared at the time of the landslide in the 15 piezometers where measurements were available (Montgomery et al. 2009). The h/z ratio is computed as the pore water pressure above the base of the soil divided by the soil depth (Fig. S10). Values of $h/z > 0$ indicate the presence of a water table above the soil layer, while $h/z < 0$ denoting an unsaturated soil base. The 3D grids of pore pressures are used to determine the hillslope subsurface flow directions by computing the flux magnitude and components using the gradient terms in the Richards equation (e.g., Richards, 1931; Brutsaert, 2005). The evolution over time of pore water pressure, seepage flux magnitudes, and directional changes are presented for two different cross sections within CB1, i.e., North-South (NS) in Fig. 16-k and West-East (EW) in Fig. 16-l, located around the landslide's upper scar. Specifically, we extract two-dimensional y-z and x-z plane (Fig. 16-b) slices from a 3D grid of pore pressure and quantified seepage flux magnitudes and directions within the NS-EW cross sections, respectively. To investigate the effect of groundwater flow governing the hydrological processes occurring at the soil-bedrock interface, the temporal evolution and the spatial variability of the magnitude and angle of the seepage vector are also examined. The angle of the seepage vector λ [°] was calculated with respect to an outward-directed vector normal to the soil-bedrock interface, following Iverson and Major (1986). Values of λ close to 90° indicate slope parallel subsurface flow, values below 90° indicate upward flux (e.g., exfiltration) from the soil-bedrock boundary, and values above 90° indicate downward flux (e.g., infiltration) to the soil-bedrock boundary. The graphical representation of λ is depicted in Fig. S10 in the Supplementary Material.

4.4 Results

4.4.1 Sprinkling experiment (EXP)

In this section, a comparison between observed and modeled soil pore water pressure and discharge is presented for EXP across various CZ scenarios and UB conductivities. The aim is to assess the robustness of the numerical model through verification against field-monitored data to quantify the effects of different CZ scenarios on the model's ability to reproduce observations all over CB1.

Fig. 17-a-to-h displays observed and simulated soil pore water pressure during the sprinkling experiment across all 100 tensiometers, for each CZ scenario and both conductivity cases. Pressure values range between -1.5 m and 0.5 m, with most points remaining unsaturated throughout the sprinkling experiment. The model does not fully capture the spatially varying initial conditions of EXP (dark blue colors, May 27th - May 28th) across multiple points. The accuracy increases as the EXP infiltration progresses (colors transitioning from light blue to green and yellow, May 29th - June 3rd). CZ(soil), CZ(RD4m) and CZ(RD9m) exhibit a saturated response in few points in contrast to CZ(stress). This effect is amplified with lower bedrock conductivity. In the draining phase (colors transitioning from orange to red, June 3rd - June 7th), the pore water pressures are slightly overestimated for all scenarios.

The limited ability to reproduce the initial conditions can be partly attributed to the high heterogeneity, uncertainty, and variability of the soil hydrologic properties, as well as potential errors in the localized placement of tensiometers. Additionally, uncertainties in vegetation-related parameters used in the evapotranspiration formulation may have contributed, particularly in capturing the effects of the three-week dry period preceding the experiment. The discrepancy in the draining phase instead is primarily attributed to the hysteretic behavior of CB1 unsaturated soil, which necessitates accounting for the dual nature of the SWRC during wetting and drying, as observed in local field measurements (Torres et al. 1998, Ebel et al. 2010). GEOtop does not support hysteresis of unsaturated medium and therefore the SWRC adopted are the mean of wetting and drying curves shown in Ebel et al. (2007b) and Ebel et al. (2008).

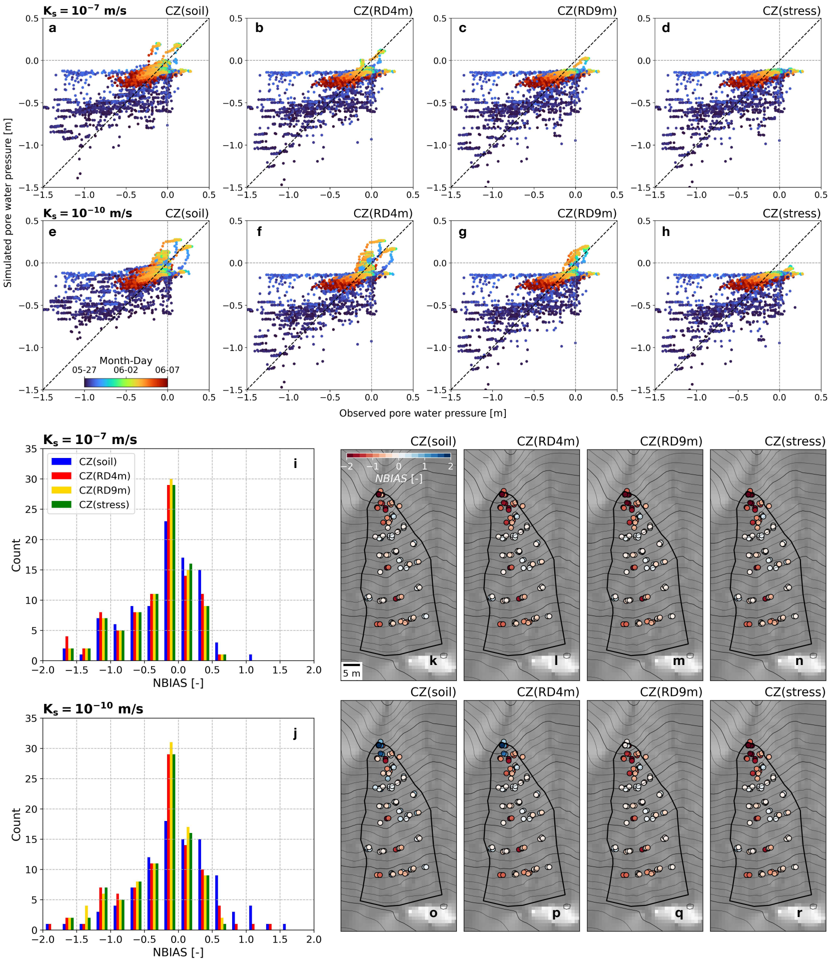

Figure 17. a EXP results. Scatter plot between observed and simulated pore water pressure in the 100 tensiometers for each CZ scenario subdivided by $k_s=10^{-7}$ m/s (a, b,

c, d) and $k_S=10^{-10}$ m/s (e, f, g, h). The color ranges from blue (begin of the experiment in May 27th, 1992) to red (after the end of the experiment in June 7th, 1992). The dashed-grey lines indicate the separation between unsaturated-saturated domains. (i) histogram and (k, l, m, n) spatial variation of NBIAS across all CZ for $k_S=10^{-7}$ m/s. (j, o, p, q, r) The same for $k_S=10^{-10}$ m/s.

To assess the model performance on pressure prediction robustly, we quantify mean and median GOF indices across all 100 tensiometers for each test (Tab. 5). The average NSE for all tensiometers rises with lower hydraulic conductivity and becomes positive in all scenarios except CZ(stress). The greatest improvements occur in CZ(RD4m) and CZ(RD9m), where NSE increases from -0.01 to -0.13 and to 0.19 and 0.08, respectively. NBIAS remains consistently negative, ranging from -0.25 to -0.39 for KS7 and from -0.33 to -0.09 for KS10. This indicates a general underestimation of pore water pressure, except for CZ(soil)-KS10, where it is positive. The bias becomes less negative as conductivity decreases and in CZ scenarios with a shallow WB. MAE shows no significant variation among the scenarios. CZ(stress) performs the worst across all evaluated indices.

When focusing only on tensiometers with positive NSE values, both the median and mean NSE increase significantly to 0.69 and 0.63 for all CZ scenarios with WB and each conductivity setting. The similar NSE values in these CZ scenarios are due to most tensiometers with positive NSE being located in unsaturated zones, which behave similarly across all CZ configurations with WB underneath soil. In contrast, CZ(soil) displays lower performance in median and mean for KS7 (0.66 and 0.61) and KS10 (0.52 and 0.51). NBIAS eventually becomes less negative, with values ranging from -0.10 to 0, but still showing no major differences across CZ structures and conductivities. CZ(RD9m)-KS10 has the highest count of tensiometers with NSE greater than zero, totaling 76 out of 100.

Fig. 17-k-to-r shows the spatial variation of NBIAS across all simulations to better understand where pore water pressure is over or underestimated. The central and upper parts of CB1 show almost no difference in NBIAS, which stays near zero for most points. Only a few underestimations appear in some tensiometer nests in the top row or in the CB1 hollow. The most significant variations occur at the UW. In the KS10 case (Fig. 17-o-to-r), the points at the outlet indicate a positive

NBIAS, meaning there is a pressure overestimation compared to the observed values. In contrast, KS7 (Fig. 17-k-to-n) shows very similar behavior across all CZs. The positive NBIAS in KS10 gradually decreases from CZ(soil), where it is nearly twice the variance, to CZ(RD4 m), around 1, and then to CZ(RD9 m), which is close to zero, as the WB depth increases. This trend is also visible in the NBIAS histograms (Fig. 17-i,j). The saturated area above the UW is crucial for CB1, as its size controls the subsurface runoff generation (e.g., Anderson et al. 1997; Montgomery et al. 1997; Montgomery et al. 2001). The spatial variation of NSE and MAE are presented in the Supplementary Material in Figs. S11 and S12.

		Sprinkling Experiment (1992)													**Landslide Storm**
		All tensiometers			**Positive tensiometers (NSE>0)**							**Discharge (NSE)**			**Discharge (NSE)**
		Mean			*Mean*			*Median*			Count>0	UW	LW	SUM	UW
		NSE	MAE	NBIAS	NSE	MAE	NBIAS	NSE	MAE	NBIAS					
KS7	CZ(soil)	-0.05	0.12	-0.25	0.66	0.11	**-0.01**	0.61	0.12	-0.01	73	0.73	-1.04	0.71	0.86
	CZ(RD4m)	-0.01	0.12	-0.36	**0.69**	**0.10**	-0.08	**0.63**	0.12	-0.09	74	**0.91**	-1.01	0.31	0.88
	CZ(RD9m)	-0.13	0.12	-0.39	**0.69**	0.11	-0.10	**0.63**	0.12	-0.10	74	0.15	-0.03	0.06	0.60
	CZ(stress)	-0.18	0.12	-0.39	**0.69**	0.11	-0.10	**0.63**	0.12	-0.10	74	-0.73	-0.08	-0.41	-0.44
KS10	CZ(soil)	0.07	0.13	0.13	0.52	0.11	**-0.01**	0.51	0.13	**0.00**	70	-5.45	-1.04	0.51	-0.18
	CZ(RD4m)	**0.19**	**0.11**	**-0.09**	0.68	**0.10**	-0.08	**0.63**	**0.11**	-0.06	74	-3.68	-0.86	0.67	0.25
	CZ(RD9m)	0.08	**0.11**	-0.27	**0.69**	**0.10**	-0.10	**0.63**	**0.11**	-0.09	**76**	0.62	**0.46**	**0.74**	**0.92**
	CZ(stress)	-0.07	0.12	-0.33	**0.69**	0.11	-0.10	**0.63**	0.12	-0.09	74	-0.40	0.31	-0.02	-0.21

Table 5. a Summary of the GOF indicators (NSE [-] , MAE [m] and NBIAS [-]) for all 100 tensiometers and for the discharges measured at the two weirs during EXP. The GOF were computed first using all instruments, and then considering only those with NSE > 0, following Ebel et al. (2007b). Results are presented for all CZ scenarios, subdivided by saturated hydraulic conductivity values of $k_s=10^{-7}$ *m/s and* $k_s=10^{-10}$ *m/s. For STORM, the only available measurement in time is the discharge at the upper weir. Bold numbers indicate the best GOF in each column. (UW=upper weir, LW=lower weir, SUM=upper weir+lower weir)*

The comparison between the observed and simulated discharges at the two weirs (Fig. 18-a-to-f) shows very strong differences in the simulated hydrograph depending on the different CZ scenarios and the hydraulic conductivity adopted. Fig. 18 panel rows are subdivided for showing the discharge at UW (Fig. 18-a,b), at LW (Fig. 18-c,d) and their SUM (Fig. 18-e,f) with columns being KS7 and KS10 cases. CZ(soil) is the only scenario without WB and therefore has no water flow through the LW.

In the KS7 case, CZ(RD4m) shows the best agreement with the observed UW discharge, achieving an NSE of 0.91 (Tab. 5), although it produces almost no flow through LW and has a low NSE for the total discharge SUM of 0.31. The timing of the rising and falling limbs of the hydrograph is well reproduced, although the model slightly underestimates the steady-state discharge with average modeled 0.11 L/s against observed 0.14 L/s. All CZ scenarios underestimate SUM, with the water balance indicating that only 37%, 23%, 17%, and 9% of rainfall is converted into discharge for CZ(soil), CZ(RD4m), CZ(RD9m), and CZ(stress), respectively. The remaining portion is retained within the leaky UB, highlighting a consistent underestimation of runoff compared to the observed partitioning of 59% runoff and 41% deep groundwater recharge.

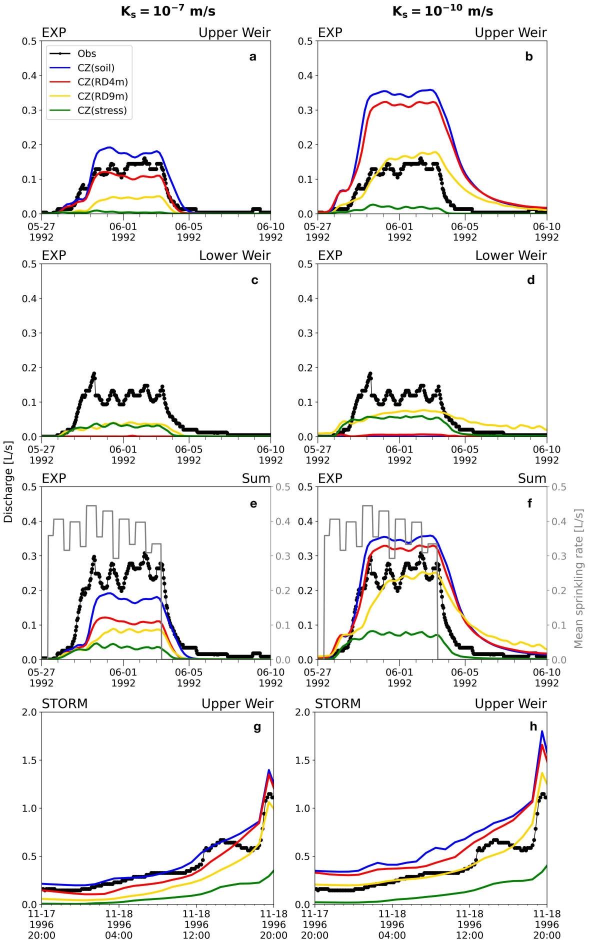

Figure 18. Comparison between modeled and observed discharge during EXP at the Upper Weir, at Lower Weir and their Sum for each CZ scenario subdivided by $k_s=10^{-7}$ *m/s (a, b, c) and* $k_s=10^{-10}$ *m/s (e, f, g). In the background (c, g), the mean measured sprinkling rate in grey. Comparison between modeled and observed discharge during STORM at the Upper Weir* $k_s=10^{-7}$ *m/ (d) and* $k_s=10^{-10}$ *m/s (h).*

In the KS10 case, CZ(soil) and CZ(RD4m) produce more than twice the observed discharge at UW, exceeding 0.3 L/s, with discharge-to-rainfall ratios of 91% and 84%. This indicates that nearly all rainfall is converted into rapid runoff and leaves CB1, as illustrated in Fig. 18-f, where the simulated discharge volume matches the mean sprinkling rate. In contrast, CZ(RD9m) successfully reproduces both the rising and steady-state phases of the UW hydrograph, although it exhibits a slower drainage response. A marked improvement is also observed at LW for CZ(RD9m) and CZ(stress), where NSE values increase to 0.46 and 0.31, respectively, from the negative values obtained under KS7. Notably, CZ(RD9m) is the only scenario achieving positive NSE values across UW, LW, and SUM simultaneously, with the latter showing a global NSE of 0.74. Furthermore, its discharge ratio of 66% closely matches the observed value of 59%.

4.4.2 Landslide-triggered Rainfall Event (STORM)

In the STORM analysis, soil saturation and pressure, subsurface flow patterns, and discharge dynamics are examined to characterize the spatial and temporal evolution of pore pressure and subsurface flow under an extreme rainfall event for all CZ structures and bedrock conductivities.

Fig. 19 shows the pressure at the soil base for all CZ configurations. The rows are arranged by increasing WB depth from top to bottom. The maps are displayed at different time steps: 24, 12, and 2 hours before (the moment of highest recorded rainfall intensity), as well as at the time of the landslide. This scheme applies to both bedrock conductivities, with KS7 including the left panels and KS10 the right ones. Fig. S13 presents the corresponding results for h/z. Since h/z maps serve as a proxy for pressure, the conclusions are consistent with those derived from the pressure maps. The figures highlight distinct spatial pressure patterns and variations over time. The pressure concentration zones are located along the hollow, matching the fracture zone exposed after the landslide event. CZ(soil) is the only scenario to reach full soil base saturation over CB1. CZ(RD4m) exhibits soil saturation even above the upper scar. Instead, the CZ(RD9m) and CZ(stress) saturation area is confined below the upper scar or only in the lowest part of CB1, respectively. These patterns are mainly influenced by the CZ structure instead of bedrock conductivity. In CB1, both the area and intensity of pressure decrease as WB depth increases. As expected, larger pressures are found within the CB1 hollow and around the UW area. These areas reflect topographic convergence and weathered bedrock thinning towards the outlet, that constitute first order effects on saturation development. Secondly, spatial variability in soil and WB thickness influences the pressure field, leading to a heterogeneous, patchy pattern of saturation, which is noticeable in the CB1 hillslope above the landslide's upper scar in CZ(RD4m), CZ(RD9m), and CZ(stress) during the last two dates.

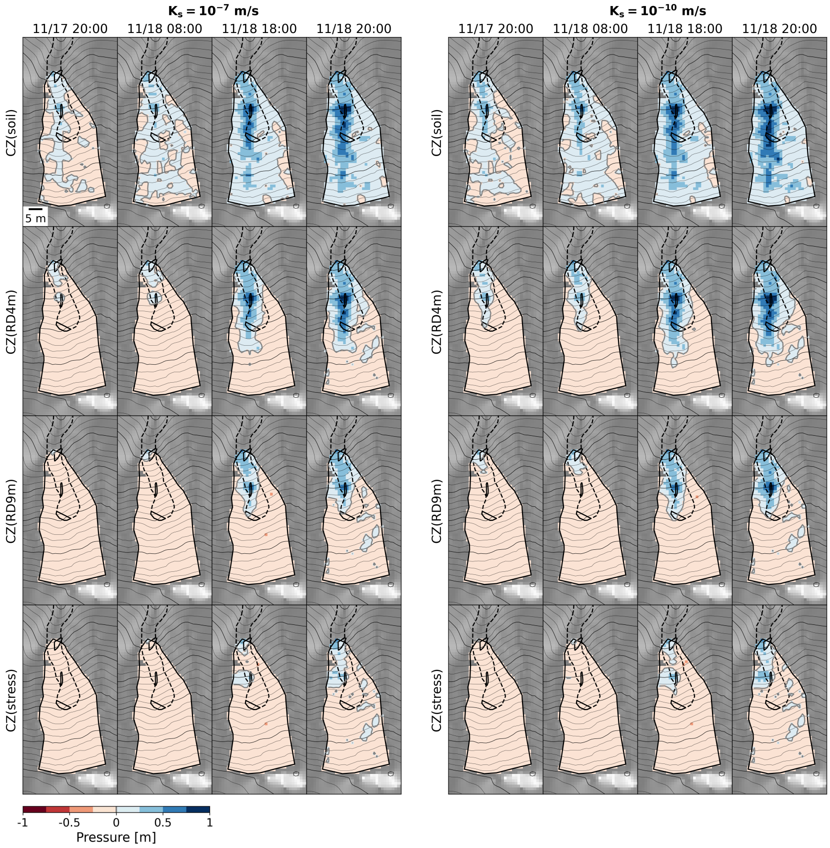

Figure 19. STORM results. Simulated pore water pressure at soil base for each CZ scenario subdivided by $k_s=10^{-7}$ m/s (left panels) and $k_s=10^{-10}$ m/s (right panels) at landslide timing, 2, 12 and 24 hours before. From top to bottom, the degree of bedrock weathering increases, while from left to right, the time approaches the landslide event. Red colors indicate unsaturated areas and blue colors saturated areas. Dashed black

line is the 1996 CB1 landslide scar, continuous black lines are the fractures exposed after the event.

Fig. 20 shows a quantitative point-wise evaluation of the h/z results at landslide time. Panel i shows the location of the 15 analyzed piezometers colored by h/z. The points of higher saturation correspond to the three post-failure open fractures. The numbers help the reader to identify specific points across all panels. Panels a-to-h illustrate the comparison between simulated and observed h/z for all CZ and both bedrock conductivities, where the points are colored by the soil thickness and shaped by absolute error quantiles (below 25%, above 75% and in between) computed considering all values across all tests. Panels j-to-q illustrate the spatial variations corresponding to panels a-to-h. Saturated areas where h/z>0 is superimposed using a black hatch pattern. Points 0, 3, 9, located above the outlet and the central fracture, are generally consistent with field observations. Regardless of the CZ scenario, point 12 at the top of the landslide head scarp is always underestimated. In general, points 1, 8, and 11, located in the lower portion of the CB1 hollow, are overestimated. CZ(RD4m) best reproduces points 5, 13, and 14 in the upper part of the hillslope, whereas CZ(RD9m) performs better in the lower section. Both scenarios exhibit the lowest absolute errors at these respective locations, as indicated by the higher concentration of circles: the deeper the WB , the error in h/z increases in the upper portion of CB1, the error decreases in the lower portion. However, plausible localized effects associated with variation of the CZ structure or hydraulic properties may influence the saturation response at points 2, 6, and 10, where the observed h/z values are very low, but the modeled values are higher.

Fig. 18-g,h displays the comparison between modeled and observed discharge at the UW for all CZ scenarios and bedrock conductivities until 24h before the landslide event. The LW is not considered since it is affected by the subsurface runoff from the neighboring CB2 basin during the storm. The results are consistent with EXP (Fig. 18-a,b and Tab. 5). CZ(RD4m)-KS7 and CZ(RD9m)-KS10 are the two cases where discharge closely match the observation at UW, beside the peak overestimation of ~1.33 L/s, compared with the measured 1.15 L/s on November 18th 19:30, for both cases. The buildup to the peak is better represented by CZ(RD9m)-KS10, which reaches the highest KGE of

0.92. The small discharge bump that occurs between November 18th, 12:00-16:00 is missed by the model. This likely happens because the recorded rainfall intensity stays relatively constant throughout the day. CZ(stress) always underpredicts discharge by ~70%.

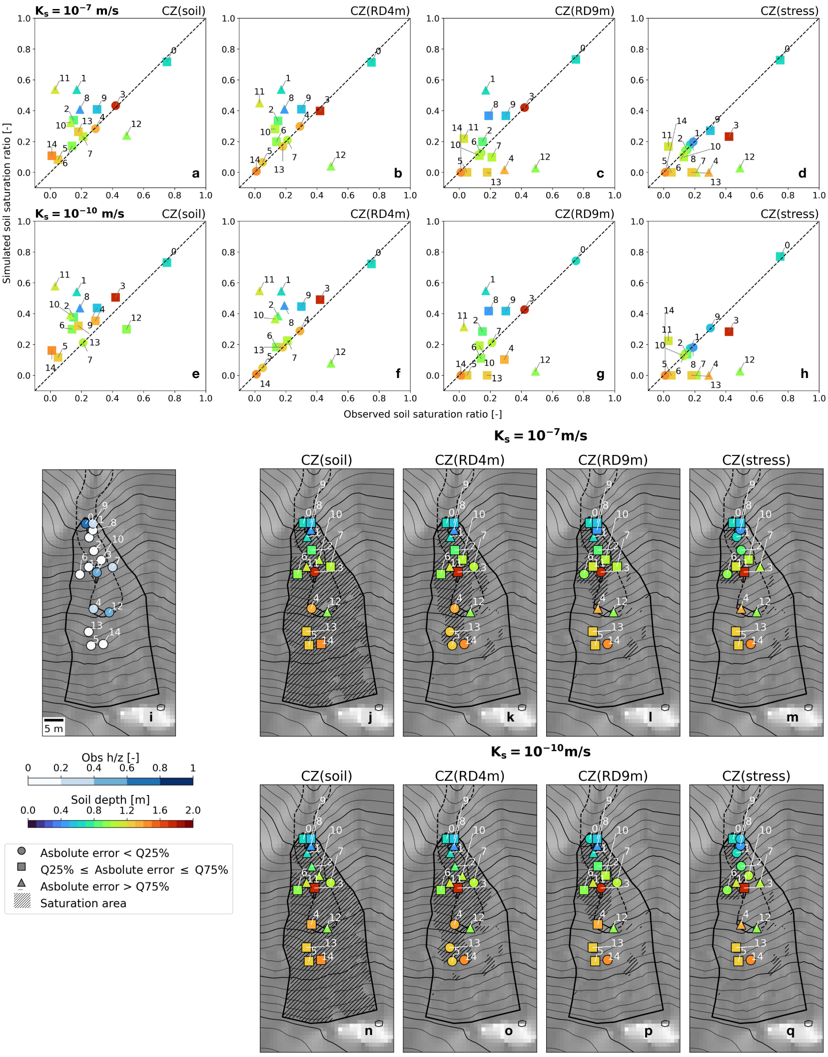

Figure 20. STORM results. Comparison between simulated and observed soil saturation ratio h/z for 14 piezometers at landslide time. The sub-panels (a to h) show scatter plots of measured against simulated h/z values for each CZ scenario subdivided by k_S=10^{-7} m/s (a, b, c, d) and k_S=10^{-10} m/s (e, f, g, h). Marker shape indicates the absolute error quantile, and color represents soil thickness. (i) Piezometer locations colored by the observed h/z. The sub-panels (j to q) display the extent of the saturated area at landslide time (black hatch) and the piezometers colored by soil depth and

shaped according to absolute error quantile for all CZ and bedrock conductivities. Dashed black line is the 1996 CB1 landslide scar, continuous black lines are the fractures exposed after the event.

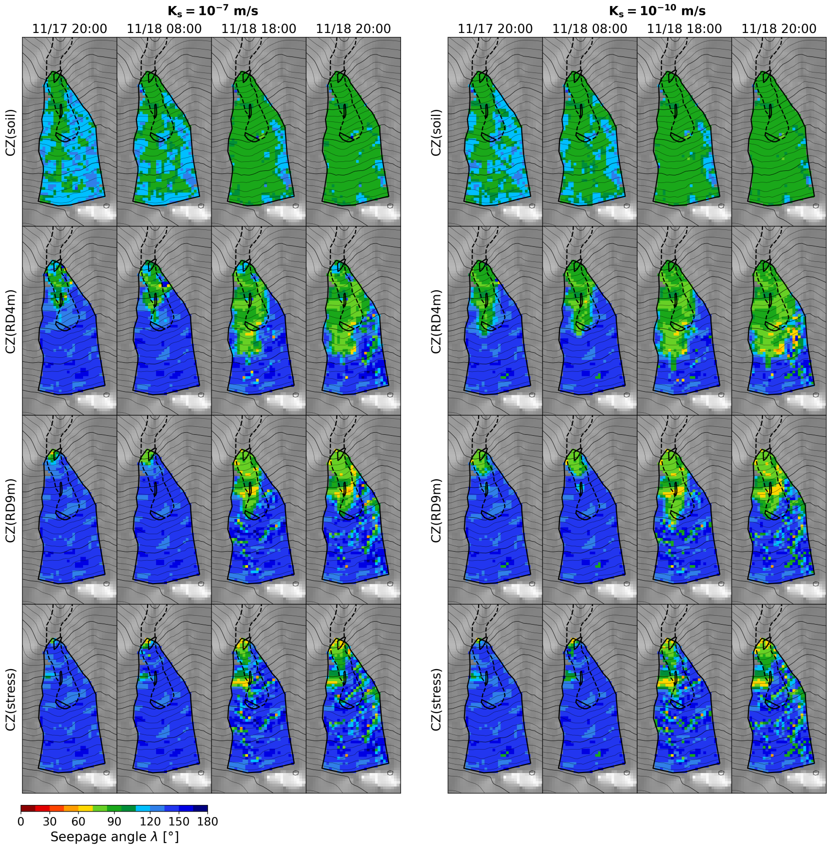

Figure 21. STORM results. Simulated seepage angle at soil-bedrock interface for each CZ scenario subdivided by k_s=10^{-7} m/s (left panels) and k_s=10^{-10} m/s (right panels) at landslide timing, 2, 12 and 24 hours before. The angle indicates the flux orientation with respect to soil base: $\lambda > 90$ water is infiltrating into bedrock, $\lambda \sim 90$ water flow is slope parallel, $\lambda < 90$ the water is exfiltrating from the bedrock. Dashed black line is the 1996 CB1 landslide scar, continuous black lines are the fractures exposed after the event.

The maps of seepage angles at soil-bedrock boundary (Fig. 21) show that bedrock flux into the soil has specific patterns depending on the CZ scenarios rather than UB conductivity. The color scale ranges from 0° (red, upward flow normal to the boundary, exfiltration from underneath bedrock) to 90° (green, slope-parallel flow), extending to 180° (blue, downward flow normal to the boundary, infiltration into bedrock below). In general, the area of slope-parallel flow (green tones) grows as the landslide event gets closer. This change happens alongside an increase in soil-base saturation (Fig. 19 and Fig. S13) and comes at the cost of infiltration into the vadose zone (blue tones). This effect is stronger in CZ scenarios with a thinner WB. Specifically, CZ(soil) indicates that near the peak of rainfall, the soil-bedrock boundary becomes fully saturated. The entire hillslope then shows slope-parallel flow toward the outlet. CZ(RD4m) primarily shows unsaturated infiltration in the upper basin and pseudo-parallel flow in the central and lower sections. In contrast, CZ(RD9m) shows a localized zone of exfiltration from underneath the saturated WB, with flow angles between 60° and 75°. This corresponds to the open central fracture that was visible after the landslide. CZ(stress) displays a similar pattern, shifted leftward outside the scar, with additional exfiltration above the UW. Few isolated yellow-orange pixels in the upper unsaturated basin likely reflect localized high-pressure gradients or topographic artifacts.

Fig. 22 illustrates the pressure field and flux vector orientation for all CZ and both conductivity scenarios at landslide time for NS-EW cross sections (Fig. 16-b). The focus is on the zoom-in areas profiles inside landslide scar are depicted (Fig. 16-k,l). In the NS profile (panels a-to-h), the subsurface flow development is the same across all CZ, nonetheless the saturation entity and water table height above UB are controlled by the geometry and thickness of the WB. Rainfall water collects at the base of the WB, forming a perched water table that rises into the soil layer. Isolated positive pressure pulses are also visible in the upper part of the profile. Subsurface flow is mostly vertical under unsaturated conditions but becomes slope-parallel as the water table rises. Minor differences exist between KS7 and KS10 in soil and WB resulting in higher pressure and slightly shallower water table in KS10. Conversely, bedrock conductivity mainly affects the UB layer. In KS7, the bedrock is very leaky, and the flux orientation is vertical toward the domain bottom. This means that a large amount of water infiltrates to recharge the very deep groundwater. In KS10, the subsurface flow remains slope-parallel, indicating that the initial condition is mostly maintained and only a limited infiltration occurs into the UB.

In the East-West profile (panels i-to-p), subsurface flow in CZ(soil), CZ(RD4m), and CZ(RD9m) is mainly controlled by topography. Flow paths converge from the two lateral divides into the central hollow. In contrast, in CZ(stress), flow is more affected by the WB-UB shape. This is the only configuration that is convex beneath the ridge. It causes water to move laterally toward the deepest part of the WB instead of beneath the central CB1 hollow. Figs. S14, S15, S16, S17 illustrate the temporal evolution of the pressure and flux fields for the two profiles at 24, 12, and 2 hours before, as well as at the time of the landslide.

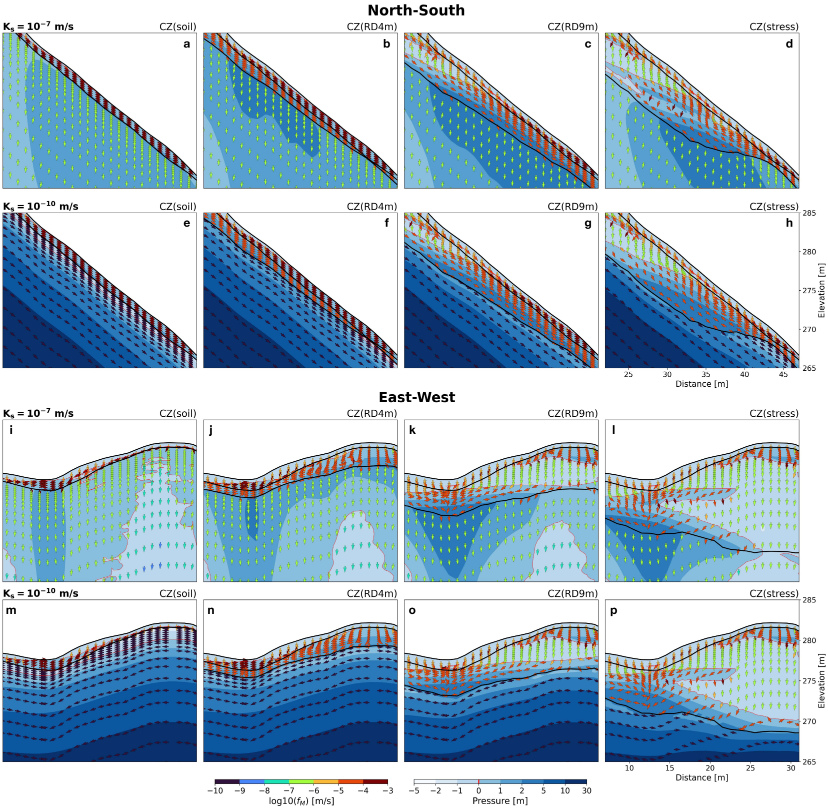

Figure 22. STORM results. North-South CB1 profile showing pressure field and flux direction and magnitude (in log scale) for each CZ scenario at landslide time subdivided by k_S=10^{-7} m/s (a, b, c, d) and k_S=10^{-10} m/s s (e, f, g, h). East-West CB1 profile showing pressure field and flux direction and magnitude (in log scale) for each CZ scenario at landslide time subdivided by k_S=10^{-7} m/s (i, j, k, l) and k_S=10^{-10} m/s (m, n, o, p). Black lines represent topographic surface, soil-bedrock boundary and, if present, weathered- unweathered bedrock boundary. The red line represents the position of the water table. The sub-panel are the zoomed-in area depicted in Fig. 16-k,l.

4.5 Discussion

4.5.1 Advance from previous CB1 CZ hydrological modeling

Ebel et al. (2007b) were the first to conduct high-resolution 3-D transient hydrological modeling of the CB1 CZ to reproduce the 1992 sprinkling experiment. Their CZ conceptualization consisted of a vertically stratification subdivided into a soil mantle, a thin saprolite layer (max. 1.1 m depth at the ridge), a WB layer (max. 4 m depth at the ridge, similar to our CZ(RD4m)), and a leaky UB layer. Both the WB and UB were assigned identical hydraulic properties and treated as UB (Tab. 4, Unweathered Bedrock). Their simulations reproduced several important features of the CB1 hydrologic response, such as runoff generation at the UW, the formation of saturation at the soil-saprolite interface above the channel head, and the overall dynamics of tensiometer pressure-head response in the soil. However, they also produced unrealistic pressure buildups in some tensiometers near the channel head and underestimated the LW discharge by approximately a factor of four. The unrealistic pressure heads resulted from assuming the upper weir as an impermeable boundary, while the LW underestimation was explained by the absence of clear data on fracture aperture, density, and connectivity to characterize the WB. Their model also applied a spatially uniform rainfall rate across CB1, despite the known heterogeneity in sprinkling intensities, and neglected evapotranspiration. Despite these limitations, their work clearly demonstrated that the 3-D geometry and hydraulic properties of the soil-saprolite system strongly control the development of saturation and pore-pressure hotspots, and that thick saprolite efficiently drains overlying soil, preventing saturation and elevated pore pressures in the upper catchment. Their study represented the first attempt to move beyond a simple soil-impermeable bedrock dichotomy and to introduce a novel CZ architecture for hydrological modeling at CB1.

Building on their work, we improved the CZ representation and hydrological modeling by: i) incorporating field-based information on WB depth and structure, ii) extending the computational domain to include the LW, iii) applying spatially distributed measured rainfall, iv) constraining UB hydraulic conductivity, v) computing the energy balance including evapotranspiration for improving the initial condition before the sprinkling, and vi) analyzing both a controlled sprinkling experiment and a high-intensity natural storm that triggered a landslide. A direct comparison shows that the CZ architecture used by Ebel et al. (2007b) falls between our CZ(soil)-KS7 and CZ(RD4m)-KS7 configurations, and their results are consistent with those we obtain using the shallower CZ scenarios (Fig. 6-c, Fig. 8-c, Fig. 17 in Ebel et al., 2007b; compared with Fig. 18-a,b, Fig. 17-a-to-h, Fig. 18-c,d in this study, respectively). With the introduction of deeper and hydrologically active WB layers in CZ(RD4m) and CZ(RD9m), we achieved substantial improvements in the simulation of both distributed and integrated hydrologic response. Tensiometer performance (median and mean NSE for positive NSE instruments) improved from 0.32 and 0.44 in Ebel et al. (2007b) to values between 0.51 and 0.69 in our deeper CZ scenarios. Positive NSE values were obtained even when including all instruments in CZ(RD4)-KS10 and CZ(RD9)-KS10 (Tab. 4 in Ebel et al., 2007b; compared with Tab. 5 in this study). UW discharge NSE increased from 0.64 in Ebel et al. (2007b) to 0.91 in CZ(RD4)-KS7 and remained similar to 0.62 in CZ(RD9)-KS10. LW discharge, which was poorly simulated in Ebel et al. (2007b) with negative NSE, improved to 0.46 in CZ(RD9)-KS10. The total water balance NSE, previously negative, increased to 0.74 in CZ(RD9)-KS10, indicating a more realistic partitioning between runoff and deep groundwater recharge. Overall, our results show that more detailed and physically realistic CZ configurations significantly improve model performance relative to the earlier modeling of Ebel et al. (2007b).

4.5.2 Impact of CZ structures on subsurface hydrology

In most hydrological applications, the near-surface hillslope is treated as a dual soil–bedrock system, with the underlying fresh bedrock assumed to be uniformly more or less permeable. An impermeable lower boundary directly beneath the soil, however, leads to substantial overestimation of both soil saturation (Fig. 20) and discharge (Fig. 18), while a leaky bedrock enhances deep groundwater recharge at the expenses of soil water accumulation and shallow runoff.

The EXP and STORM simulations demonstrate that hydrologic response at CB1 is strongly affected by the structure and depth of the CZ. As WB depth increases (moving from CZ(soil) to CZ(stress)), soil saturation magnitude decreases and its extent shrinks (Fig. 19 and Fig.

S13). Localized, disconnected saturation patches can appear during rainfall in the upper basin where shallow soil overlies thin WB, but the overall soil saturation pattern is more sensitive to CZ structure than to UB conductivity, as opposed to discharge (Fig. 18). Water tends to concentrate within hollows where lateral fast runoff convergence prevails over slow vertical unsaturated infiltration (Fig. 22). Small localized saturation zones are also visible within the WB outside the main hollow or in the upper basin. This behavior arises from the hydraulic conductivity functions of the two layers. Under unsaturated conditions, the WB is more conductive than the overlying soil (Fig. S9-c). As a result, rainfall infiltration is routed into the WB rather than accumulating at soil base.

Pressure hotspots develop in areas where bedrock fractures were exposed following the 1996 landslide. In particular, in the central fracture zone, the CZ(RD9m) scenario produces a localized exfiltration seepage from the WB into the overlying soil. This configuration is especially destabilizing for the hillslope (Iverson and Major, 1986), especially when also the downslope thinning of the hydrologically active bedrock promotes upward seepage orientation. Despite this, deep WB layers can support overall slope stability by storing a large portion of storm runoff and thereby reducing water storage and pore-pressure buildup in the soil. Under these conditions, unsaturated soil and deep WB delay runoff generation, enhance groundwater recharge, and postpone the onset of landslide-triggering saturation because thicker CZ structures require more water to saturate near-surface layers.

The hydrological simulations indicate that the CZ(RD9m) scenario provides the best agreement with both observed and modeled hydrologic variables, as well as the best match between predicted exfiltration locations and documented post-failure fracture outflows. This scenario incorporates the observed material transitions along the hillslope, particularly the change from pervasively oxidized material at approximately 4.5 m depth to fractured weathered bedrock at 9 m depth at the ridge borehole location (Anderson et al., 2002). This transition likely constitutes an important active hydrologic boundary that governs water exchange between soil and WB, although some uncertainties remain regarding the representation of fracture characteristics in the CZ model.

4.5.3 Limitations, uncertainties, and future directions

Our CZ conceptualizations aim to represent the hydrologically significant features of the deep critical zone at CB1. However, these simplified structures cannot fully capture the spatial variability and heterogeneity of the site, which limits our ability to reproduce all localized aspects of CZ hydrologic behavior.

Modeling flow through fractured bedrock remains challenging due to the strong heterogeneity and anisotropy of fracture networks, limited field data on fracture geometry and connectivity, scale-dependent behavior, and the inherently non-linear nature of flow in such systems. Previous work at CB1 pointed out that accurate representation of fracture location and connectivity is essential for simulating WB flow (Ebel et al., 2008), consistent with its role as a preferential flow pathway during storms (Montgomery et al., 1997; Montgomery and Dietrich, 2002; Montgomery et al., 2009). Because detailed fracture distribution data are lacking at CB1, we approximated the WB as a single bulk-conductivity layer, which likely hides important spatial variations. In addition, bedrock weathering progressively transforms low-conductivity rock into a dynamic water storage reservoir (Rempe and Dietrich, 2018). The hydraulic properties of unsaturated bedrock, i.e., SWRC parameters, remain highly uncertain due to the difficulty of obtaining representative measurements at depth. Comprehensive datasets covering the entire CZ depth, rather than only the shallow subsurface, are needed to reduce these uncertainties.

Falling-head tests performed during the steady state of EXP (Torres et al., 1998) revealed contrasting trends in hydraulic conductivity between soil and bedrock piezometers. Soil conductivity decreased with depth, ranging from 10^{-3} m/s in shallow pipes near the channel head to 10^{-6} m/s in deeper locations near the 1996 upper scar, with an arithmetic mean of 10^{-4} m/s. In contrast, conductivity estimated in saprolite, and near-surface bedrock varied of many orders of magnitude between 10^{-3} m/s and 10^{-8} m/s, with an arithmetic mean of 10^{-5} m/s, but exhibited no systematic change with depth or location. Such variability supports the expectation that bedrock flow at CB1 may be highly spatially localized, with substantial subsurface flow focusing on a limited number of high-permeability, shallow bedrock zones (Montgomery et al., 2002). Considering these observations, together with our discharge, tensiometer, soil saturation, and zones of exfiltration results, we presume that the CZ(RD9m) configuration, with WB and UB conductivities of 10^{-5} m/s and 10^{-10} m/s, respectively, currently provides the most realistic representation of the CZ architecture and hydraulic properties between the upper landslide scar and the LW. The mean bedrock conductivity of 10^{-7} m/s, used in KS7 scenarios, provides instead a more reasonable description of the hydrological conditions within the deep CZ at the ridge. This value is consistent with published estimates of water table fluctuations in the ridge borehole, ranging from $5\text{x}10^{-5}$ to $7\text{x}10^{-7}$ m/s at ~20 m depth (Montgomery et al., 2022). On the contrary, the simulation results for the CZ(RD9m) scenario (Fig. S18 of the Supplementary Material for the full NS section extent) indicates a water table depth of approximately ~60 m at the time of the STORM landslide. This low elevation is likely a consequence of representing the UB as a highly permeable also at very deep layers. Indeed, a more physically consistent basin-wide representation would incorporate a hydraulic conductivity profile that decreases exponentially with depth, as fracture density and openness reduce reaching the UB boundary.

Future work is expected to progress toward such a representation. In a novel study (Busti et al., in preparation), a 3-D characterization of CB1 CZ hydraulic conductivity will be developed using slug-test measurements together with datasets of field seismic velocity and topographic stress presented in Higa (2023). Because hydraulic conductivity likely decreases with increasing stress concentration and higher seismic velocities, indicating fracture closure, integrating these datasets should enable more accurate delineation of active deep WB and improved identification of localized preferential-flow zones and pore-pressure hotspots, as inferred previously by Pierson (1977), Wilson and Dietrich (1987), and Montgomery et al. (1997). This enhanced CZ characterization approach will be fundamental not only for improving hydrological predictions at CB1, but for any other weathered landscapes.

4.6 Conclusions

In this investigation, we conducted a comprehensive analysis of different CZ scenarios, emphasizing their implications on hillslope hydrology, specifically within the experimental CB1 catchment. We modeled the hydrological response of the hillslope to two distinct rainfall events and validated our model results by comparing various types of field measurements, without the need to tune free hydrological parameters. We validated a three-dimensional hydrological model using pore water pressure and discharge measurements obtained during the 1992 sprinkling experiment, as well as soil saturation data collected during the 1996 storm that lead to the CB1 landslide. Our results indicated that the accuracy in reproducing the hydrological response of CB1 basin is notably influenced by the assumed structure of the CZ and its hydrologic characteristics. The pressure state within the weathered bedrock significant control over the groundwater level, consequently influencing the saturation pattern and discharge dynamics of the overlying colluvium. From a hydrological perspective, our work builds on previous studies that demonstrated the importance of deep critical zones in hillslope hydrology through direct measurements (e.g., Gabrielli et al., 2012; Rempe and Dietrich, 2018) and emphasized the need to include their geometries and parametrization in hydrological models (Salve et al., 2012; Hahm et al., 2019; Rempe and Dietrich, 2018). Our results highlight the fundamental role of the CZ structure in regulating pore pressure concentration, saturation development, and soil-bedrock seepage dynamics. All these phenomena impact the behavior of infiltration-exfiltration flows and groundwater movement for runoff generation and natural hazard triggering such as flash floods or shallow landslides.

Acknowledgment

This work is supported by National Science Foundation grants EAR-1945431 and EAR-2012073. Any use of trade, firm, or product names is for descriptive purposes only and does not imply endorsement by the U.S. Government.

References

Anderson, S. P., Dietrich, W. E., Torres, R., Montgomery, D. R., and Loague, K. (1997a). Concentration discharge relationships in runoff from a steep, unchanneled catchment: Water Resources Research, 33, 211-225.

Anderson, S. P., Dietrich, W. E., Montgomery, D. R., Torres, R., Conrad, M. E., and Loague, K. (1997b). Subsurface flowpaths in a steep, unchanneled catchment: Water Resources Research, 33, 2637-2653.

Anderson, S. P., Dietrich, W. E., and Brimhall Jr, G. H. (2002). Weathering profiles, mass-balance analysis, and rates of solute loss: Linkages between weathering and erosion in a small, steep catchment. Geological Society of America Bulletin, 114(9), 1143-1158.

Arnone, E., Noto, L. V., Lepore, C., and Bras, R. L. (2011). Physically-based and distributed approach to analyze rainfall-triggered landslides at watershed scale. Geomorphology, 133(3-4), 121-131.

Arora, B., Kuppel, S., Wellen, C., Oswald, C., Groh, J., Payandi-Rolland, D., Stegen, J., and Coffinet, S. (2023). Building Cross-Site and Cross-Network collaborations in critical zone science. Journal of Hydrology, 618, 129248.

Barling, R. D., Moore, I. D., and Grayson, R. B. (1994). A quasi-dynamic wetness index for characterizing the spatial distribution of zones of surface saturation and soil water content. Water Resources Research, 30(4), 1029-1044.

Baum, R. L., Godt, J. W., and Savage, W. Z. (2010). Estimating the timing and location of shallow rainfall-induced landslides using a model for transient, unsaturated infiltration. Journal of Geophysical Research: Earth Surface, 115(F3).

Bellugi, D., Milledge, D. G., Dietrich, W. E., Perron, J. T., and McKean, J. (2015a). Predicting shallow landslide size and location across a natural landscape: Application of a spectral clustering search algorithm. Journal of Geophysical Research: Earth Surface, 120, 2552-2585.

Bellugi, D., Milledge, D. G., Dietrich, W. E., McKean, J. A., Perron, J. T., Sudderth, E. B. and Kazian, B. (2015b). A spectral clustering search algorithm for predicting shallow landslide size and location. Journal of Geophysical Research: Earth Surface, 120, 300-324.

Bellugi, D. G., Milledge, D. G., Cuffey, K. M., Dietrich, W. E., and Larsen, L. G. (2021). Controls on the size distributions of shallow landslides. Proceedings of the National Academy of Sciences, 118(9), e2021855118.

Bertoldi, G., Rigon, R., and Over, T. M. (2006). Impact of watershed geomorphic characteristics on the energy and water budgets. Journal of Hydrometeorology, 7(3), 389-403.

Birkel, C., Soulsby, C., and Tetzlaff, D. (2011). Modelling catchment-scale water storage dynamics: Reconciling dynamic storage with tracer-inferred passive storage. Hydrological Processes, 25(25), 3924-3936.

Borga, M., Dalla Fontana, G., and Cazorzi, F. (2002). Analysis of topographic and climatic control on rainfall-triggered shallow landsliding using a quasi-dynamic wetness index. Journal of Hydrology, 268(1-4), 56-71.

Brantley, S. L., Lebedeva, M. I., Balashov, V. N., Singha, K., Sullivan, P. L., and Stinchcomb, G. (2017). Toward a conceptual model relating chemical reaction fronts to water flow paths in hills. Geomorphology, 277, 100-117.

Brönnimann, C., Stähli, M., Schneider, P., Seward, L., and Springman, S. M. (2013). Bedrock exfiltration as a triggering mechanism for shallow landslides. Water Resources Research, 49(9), 5155-5167.

Brooks, P. D., Chorover, J., Fan, Y., Godsey, S. E., Maxwell, R. M., McNamara, J. P., and Tague, C. (2015). Hydrological partitioning in the critical zone: Recent advances and opportunities for developing transferable understanding of water cycle dynamics. Water Resources Research, 51(9), 6973-6987.

Brutsaert, W. (2005). Hydrology: An Introduction. Cornell University, New York.

Burke, B. C., Heimsath, A. M., and White, A. F. (2007). Coupling chemical weathering with soil production across soil-mantled landscapes. Earth Surface Processes and Landforms: The Journal of the British Geomorphological Research Group, 32(6), 853-873.

Chen, H., Niu, Q., McNamara, J. P., and Flores, A. N. (2024). Influence of subsurface critical zone structure on hydrological partitioning in mountainous headwater catchments. Geophysical Research Letters, 51, e2023GL106964.

Chorover, J., Derry, L. A., and McDowell, W. H. (2017). Concentration-discharge relations in the critical zone: Implications for resolving critical zone structure, function, and evolution. Water Resources Research, 53(11), 8654-8659.

Durmaz, M., Hürlimann, M., Huvaj, N., and Medina, V. (2023). Comparison of different hydrological and stability assumptions for physically-based modeling of shallow landslides. Engineering Geology, 323, 107237

Dwivedi R., Meixner T., McIntosh J. C., Ty Ferré, P. A., Eastoe, C. J., Niu, G., Minor, R. L., Barron-Gafford, G. A., and Chorover, J. (2019). Hydrologic functioning of the deep critical zone and contributions to streamflow in a high-elevation catchment: Testing of multiple conceptual models. Hydrological Processes,33, 476-494.

Ebel, B. A., Loague, K., Dietrich, W. E., Montgomery, D. R., Torres, R., Anderson, S. P., and Gianbelluca, T. W. (2007a). Near-surface hydrologic response for a steep, unchanneled catchment near Coos Bay, Oregon: 1. Sprinkling eperiments. American Journal of Science, 307(4), 678-708.

Ebel, B. A., and Loague, K. (2008). Rapid simulated hydrologic response within the variably saturated near surface. Hydrological Processes: Hydrological Processes, 22, 464-471.

Ebel, B. A., Loague, K., Vandwerkwaak, J. E., Dietrich, W. E., Montgomery, D. R., Torres, R., and Anderson, S. P. (2007b). Near-surface hydrologic response for a steep, unchanneled catchment near Coos Bay, Oregon: 2. Physics-based simulations. American Journal of Science, 307(4), 709-748.

Ebel, B. A., Loague, K., Montgomery, D. R., and Dietrich, W. E. (2008). Physics-based continuous simulation of long-term near-surface hydrologic response for the Coos Bay experimental catchment. Water Resources Research, 44, W07417.

Ebel, B. A., Loague, K., and Borja, R. I. (2010). The impacts of hysteresis on variably saturated hydrologic response and slope failure. Environmental Earth Sciences, 61, 1215-1225.

Ebrahim, K. M. P., Gomaa, S. M. M. H., Zayed, T., and Alfalah, G. (2024). Rainfall-induced landslide prediction models, part ii: deterministic physical and phenomenologically models. Bulletin of Engineering Geology and the Environment, 83, 85.

Endrizzi, S., and Marsh, P. (2010). Observations and modeling of turbulent fluxes during melt at the shrub-tundra transition zone 1: point scale variations. Hydrological Resources, 41, 471-491.

Endrizzi, S., Gruber, S., Dall'Amico M., and Rigon, R. (2014). GEOtop 2.0.: Simulating the combined energy and water balance at and below the land surface accounting for soil freezing, snow cover and terrain effects. Geoscientific Model Development, 7, 2831-2857.

Formetta, G., Simoni, S., Godt, J. W., Lu, N., and Rigon, R. (2016). Geomorphological control on variably saturated hillslope hydrology and slope instability. Water Resources Research, 52(6), 4590-4607.

Gabrielli, C. P., McDonnell, J. J., and Jarvis, W. T. (2012). The role of bedrock groundwater in rainfall-runoff response at hillslope and catchment scales. Journal of Hydrology, 450, 117-133.

Guo, L., and Lin, H. (2016). Critical zone research and observatories: Current status and future perspectives. Vadose Zone Journal, 15(9), vzj2016-06.

Hahm, W. J., Rempe, D. M., Dralle, D. N., Dawson, T. E., Lovill, S. M., Bryk, A. B., Bish, B. L., Schieber, J., and Dietrich, W. E. (2019). Lithologically controlled subsurface critical zone thickness and water storage capacity determine regional plant community composition. Water Resources Research, 55(4), 3028-3055.

Hahm, W. J., Lapides, D. A., Rempe, D. M., McCormick, E. L., and Dralle, D. N. (2022a). The age of evapotranspiration: Lower-bound constraints from distributed water fluxes across the continental United States. Water Resources Research, 58(10), e2022WR032961.

Hahm, W. J., Dralle, D. N., Sanders, M., Bryk, A. B., Fauria, K. E., Huang, M. H., Hudson-Rasmussen, B., Nelson, M. D., Pedrazas, M. A., Schmidt, L., Whiting, J., Dietrich, W. E., and Rempe, D. M (2022b). Bedrock vadose zone storage dynamics under extreme drought: consequences for plant water availability, recharge, and runoff. Water Resources Research, 58(4), e2021WR031781.

Hale, V. C., and McDonnell, J. J. (2016). Effect of bedrock permeability on stream base flow mean transit time scaling relations: 1. A multiscale catchment intercomparison. Water Resources Research, 52, 1358-1374.

Heidbach, O., Rajabi, M., Cui, X., Fuchs, K., Müller, B., Reinecker, J., Reiter, K., Tingay, M., Wenzel, F., Xie, F., and Ziegler, M.O. (2018). The World Stress Map database release 2016: Crustal stress pattern across scales. Tectonophysics, 744, 484-498.

Heimsath, A. M., Dietrich, W. E., Nishiizumi, K., and Finkle, R. C. (2001). Stochastic processes of soil production and transport: erosion rates, topographic variation and cosmogenic nuclides in the Oregon Coast Range. Earth Surface Processes and Landforms, 26, 5, 531-552.

Higa, J. T. (2023). Multi-scale investigations on the impacts of geologic fractures. Ph.D. dissertation, University of California Los Angeles, Los Angeles.

Holbrook, W. S., Riebe, C. S., Elwaseif, M., L. Hayes, J., Basler-Reeder, K., L. Harry, D., Malazian, A., Dosseto, A., C. Hartsough, P. and W. Hopmans, J. (2014). Geophysical constraints on deep weathering and water storage potential in the Southern Sierra Critical Zone Observatory. Earth Surface Processes and Landforms, 39, 366-380.

Iverson, R. M., and Major, J. J. (1986). Groundwater Seepage Vectors and the Potential for Hillslope Failure and Debris Flow Mobilization. Water Resources Research, 22(11), 1543-1548.

Kirchner, J. W. (2009). Catchments as simple dynamical systems: Catchment characterization, rainfall-runoff modeling, and doing hydrology backward. Water Resources Research, 45, W02429.

Li, W. C., Dai, F. C., Wei, Y. Q., Wang, M. L., Min, H., and Lee, L. M. (2016). Implication of subsurface flow on rainfall-induced landslide: a case study. Landslides, 13, 1109-1123.

Lin, H. (2010) Earth's Critical Zone and hydropedology: concepts, characteristics, and advances, Hydrology Earth System Sciences, 14, 25-45.

Liang, W. L. (2020). Dynamics of pore water pressure at the soil-bedrock interface recorded during a rainfall-induced shallow landslide in a steep natural forested headwater catchment, Taiwan. Journal of Hydrology, 587, 125003.

Lu, N., and Godt, J. (2008). Infinite slope stability under steady unsaturated seepage conditions. Water Resources Research, 44(11).

Likos, W. J., and Lu, N. (2004). Unsaturated soil mechanics. John Wiley and Sons Inc., New Jersey.

McDonnell, J. J. (2014). The two water worlds hypothesis: ecohydrological separation of water between streams and trees? Wiley Interdisciplinary Reviews: Water, 1(4), 323-329.

McDonnell, J. J., Spence, C., Karran, D. J., Van Meerveld, H. J., and Harman, C. J. (2021). Fill-and-spill: A process description of runoff generation at the scale of the beholder. Water Resources Research, 57(5), e2020WR027514.

Milledge, D. G., D. Bellugi, J. A. McKean, A. L. Densmore, and W. E. Dietrich (2014). A multidimensional stability model for predicting shallow landslide size and shape across landscapes. Journal of Geophysical Research: Earth Surface, 119, 2481-2504.

Mirus, B. B., Ebel, B. A., Loague, K., and Wemple, B. C. (2007). Simulated effect of a forest road on near-surface hydrologic response: Redux. Earth Surface Processes and Landforms: The Journal of the British Geomorphological Research Group, 32(1), 126-142.

Montgomery, D. R., Dietrich, W. E., Torres, R., Anderson, S. P., Heffner, J. T., and Loague, K. (1997). Hydrologic response of a steep, unchanneled valley to natural and applied rainfall. Water Resources Research, 33(1), 91-109.

Montgomery, D. R., and Dietrich, W. E. (2002). Runoff generation in a steep, soil-mantled landscale. Water Resources Research, 38(9), 1168.

Montgomery, D. R., Dietrich, W. E., and Heffner, J. T. (2002). Piezometric response in shallow bedrock at CB1: Implications for runoff generation and landsliding. Water Resources Research, 38(12), 1274.

Montgomery, D. R., Schmidt, K. M., Dietrich, W. E., and McKean J. (2009). Instrumental records of a debris flow initiation during natural rainfall: Implications for modeling slop stability. Journal of Geophysical Research, 114, F01031.

Montgomery, D. R., and Dietrich, W. E. (1994). A physically based model for the topographic control on shallow landsliding. Water Resources Research, 30(4), 1153-1171.

Moon, S., Perron, J. T., Martel, S. J., Holbrook, W. S., and St. Clair, J. (2017). A model of three-dimensional topographic stresses with implications for bedrock fractures, surface processes, and landscape evolution. Journal of Geophysical Research: Earth Surface, 122(4), 823-846.

Moon, S., Higa, J. T., Formetta, G., Busti, R., Bellugi, D. G., Dietrich, W. E., Milledge, D. G., and Ebel, B. A. (under review). Deep critical zone controls on shallow landslides. PNAS.

Mualem, Y. (1976). A new model predicting the hydraulic conductivity of unsaturated porous media. Water Resources Research 12, 513-522.

O'Loughlin, E. M. (1986). Prediction of Surface Saturation Zones in Natural Catchments by Topographic Analysis. Water Resources Research, 22(5), 794-804.

Pack, R. T., Tarboton, D. G., and Goodwin, C. N. (1998). The SINMAP approach to terrain stability mapping. Proceedings of the 8th congress of the international association of engineering geology, Vancouver, British Columbia, Canada, 21-25.

Pedrazas, M. A., Hahm, W. J., Huang, M.-H., Dralle, D., Nelson, M. D., Breunig, R. E., Fauria, K. E., Bryk, A. B., Dietrich, W. E., and Rempe, D. M. (2021). The relationship between topography, bedrock weathering, and water storage across a sequence of ridges and valleys. Journal of Geophysical Research: Earth Surface, 126, e2020JF005848.

Pierson, T. C. (1977). Factors controlling debris-flow initiation on forested hill- slopes in the Oregon Coast Range, Ph.D. dissertation, 166 pp., University of Washington, Seattle.

Pfister, L., Martínez-Carreras, N., Hissler, C., Klaus, J., Carrer, G. E., Stewart, M. K., and McDonnell, J. J. (2017). Bedrock geology controls on catchment storage, mixing, and release: A comparative analysis of 16 nested catchments. Hydrological Processes, 31(10), 1828-1845.

Regmi, N. R., Giardino, J. R., McDonald, E. V., and Vitek, J. D. (2015). Chapter 11 - A Review of Mass Movement Processes and Risk in the Critical Zone of Earth. Developments in Earth Surface Processes, 19, 319-362.

Rempe, D. M. and Dietrich, W. E. (2014). A bottom-up control on fresh-bedrock topography under landscapes, Proceedings of the National Academy of Sciences, 111, 6576-6581.

Rempe, D. M., and Dietrich W. E. (2018). Direct observations of rock moisture, a hidden component of the hydrologic cycle. Proceedings of the National Academy of Sciences 115, 11, 2664-2669.

Reneau, S. L., and Dietrich, W. E. (1991), Erosion rates in the southern Oregon Coast Range: Evidence for an equilibrium between hillslope erosion and sediment yield. Earth Surface Processes and Landforms, 16, 307-322.

Richards, L. A. (1931). Capillary conduction of liquids in porous mediums. Physics, 1, 318-333.

Rigon, R., Bertoldi, G., and Over, T. M. (2006). GEOtop: A Distributed Hydrological Model with Coupled Water and Energy Budgets. Journal of Hydrometeorology, 7, 371-388.

Roering, J. J., Kirchner, J. W., and Dietrich, W. E. (1999). Evidence for nonlinear, diffusive sediment transport on hillslopes and implications for landscape morphology. Water Resources Research, 35, 3, 853-870.

Rosso, R., Rulli, M. C., and Vannucchi, G. (2006). A physically based model for the hydrologic control on shallow landsliding. Water Resources Research, 42(6).

Salve, R., D. M.Rempe, and W. E.Dietrich (2012), Rain, rock moisture dynamics, and the rapid response of perched groundwater in weathered, fractured argillite underlying a steep hillslope, Water Resources Research 48 (11).

Schmidt, K. M. (1999). Root strength, colluvial soil depth, and colluvial transport on landslide-prone hillslopes. Ph.D. thesis, 258 pp., Univ. of Wash., Seattle.

Shu, L., Chen, H., Meng, X., and Chang, Y. (2024). A review of integrated surface-subsurface numerical hydrological models. Science China Earth Sciences, 67, 1459-1479.

Singha, K., and Navarre-Sitchler, A. (2021). The Importance of Groundwater in Critical Zone Science. Groundwater, 60, 1, 27-34.

St. Clair, J., Moon, S., Holbrook, W.S., Perron, J.T., Riebe, C.S., Martel, S.J., Carr, B., Harman, C., Singha, K.D. and Richter, D.D. (2015). Geophysical imaging reveals topographic stress control of bedrock weathering. Science, 350(6260), 534-538.

Stock, J. D., and Dietrich, W. E. (2006). Erosion of steepland valleys by debris flows. GSA Bulletin, 118, 9-10, 1125-1148.

Torres, R., Dietrich, W. E., Montgomery, D. R., Anderson, S. P., and Loague K. (1998). Unsaturated zone processes and the hydrologic response of a steep, unchanneled catchment. Water Resources Research, 34(8), 1865-1879.

Tromp-van Meerveld, H. J., and McDonnell, J. J. (2006). Threshold relations in subsurface stormflow: 1. A 147-storm analysis of the Panola hillslope. Water Resources Research, 42(2).

Tsukamoto, Y. (1982). Hydrological and geomorphological studies of debris slides on forested hillslopes in Japan. IAHS-AISH Publication, 137, 89-98.

Van Genuchten, M. T. (1980). A closed-form equation for predicting the hydraulic conductivity of unsaturated soils. Soil Science Society of America Journal, 44, 892-898.

Ward, P. J., Blauhut, V., Bloemendaal, N., Daniell, J. E., de Ruiter, M. C., Duncan, M. J., Emberson, R., Jenkins, S. F., Kirschbaum, D., Kunz, M., Mohr, S., Muis, S., Riddell, G. A., Schäfer, A., Stanley, T., Veldkamp, T. I. E., and Winsemius, H. C. (2020). Review article: Natural hazard risk assessments at the global scale, Natural Hazards and Earth System Sciences, 20, 1069-1096.

Weiler, M., McDonnell, J. J., Tromp-van Meerveld, I., and Uchida, T. (2006). Subsurface stormflow. Encyclopedia of Hydrological Sciences (eds M.G. Anderson and J.J. McDonnell)

White, T., Brantley, S., Banwart, S., Chorover, J., Dietrich, W., Derry, L., Lohse, K., Anderson, S., Aufdendkampe, A., Bales, R., Kumar, P., Richter, D., and McDowell, B. (2015). The Role of Critical Zone Observatories in Critical Zone Science. Developments in Earth Surface Processes, 19, 15-78.

Wilson, C. J., and W. E. Dietrich (1987). The contribution of bedrock groundwater flow to storm runoff and high pore pressure development in hollows. Erosion and Sedimentation in the Pacific Rim, 165, 49-59.

Wlostowski, A. N., Molotch, N., Anderson, S. P., Brantley, S. L., Chorover, J., Dralle, D., et al. (2021). Signatures of hydrologic function across the Critical Zone Observatory network. Water Resources Research, 57, e2019WR026635.

Chapter 5: Integrating Field Geophysics and Stress Modeling to Characterize 3D Subsurface Heterogeneity in the Critical Zone: Implications for Hillslope Hydrology and Landslide

Riccardo Busti[1], Giuseppe Formetta[1], and Seulgi Moon[2]

[1]Department of Civil, Environmental and Mechanical Engineering (DICAM), University of Trento, Trento (TN), Italy

[2]University of California Los Angeles, Department of Earth, Planetary, and Space Sciences, Los Angeles, CA, United States of America

This chapter advances 3D characterization of Critical Zone hydrological properties and its implications for hillslope hydrology and stability.

This article is currently under preparation.

5.1 Introduction

Characterizing the Critical Zone (CZ) structure and hydro-mechanical properties is fundamental to understanding how geomorphic processes and climatic forcing regulate near-surface hydrological responses and geohazards across hillslopes (e.g., Anderson et al., 2002; Brooks et al., 2015; Chorover et al., 2017; Rempe and Dietrich, 2018; Brönnimann et al., 2013; Sprenger et al., 2019; Wlostowski et al., 2021; Ackerer et al., 2023; Chen et al., 2024). Within this zone, landslide hazards represent a primary threat to infrastructure and human safety, often triggered by the complex distribution of moisture and pore water pressure in the shallow subsurface (e.g., Iverson, 2000; Wicki et al., 2020; Leonarduzzi et al., 2021). Variations in CZ architecture, including soil depth, bedrock geometry, stratification, and weathering state, control where and when water infiltrates, accumulates, or drains (e.g., Anderson et al. 1997; Anderson et al. 2002). As a result, storm-driven pore-pressure rise and subsurface flow routing (e.g., Iverson and Major, 1986; Brönnimann et al., 2013; Li et al., 2016) play a central role in triggering shallow landslides on soil-mantled hillslopes (e.g., Wilson and Dietrich, 1987; Montgomery et al., 1997; Montgomery et al., 2009; Regmi et al., 2015; Da Silva et al., 2022). However, the heterogeneous nature and poorly constrained hydrologic properties of CZ subsurface layers, particularly fractured, weathered bedrock beneath steep slopes, have made it difficult to represent realistic CZ structure in predictive hydro-geo models, which often rely on empirical or simplified parameterizations (e.g., Lin, 2010).

Geophysical surveys provide a powerful, non-invasive means of characterizing this subsurface heterogeneity (e.g., Parsekian et al. 2015). Seismic, electrical, and radar methods have revealed substantial lateral and vertical variability in CZ structure, porosity, and weathering state, demonstrating that hydraulic properties are not simply functions of depth but instead reflect landscape-scale processes (Holbrook et al., 2014; Holbrook et al., 2019). Among these methods, seismic velocity has emerged as a particularly informative proxy for subsurface mechanical and hydraulic properties. Numerous studies show that lower seismic velocities are commonly associated with increased fracture density, enhanced porosity, and higher saturated hydraulic conductivity, whereas higher velocities often reflect more intact, less permeable material (e.g., Cassiani et al., 1998; Ellefsen et al., 1999; Hyndman et al., 2000). These relationships highlight the potential of seismic imaging to constrain spatial patterns of conductivity, while also underscoring that conductivity-seismic velocity relationships are often nonlinear and site specific (e.g., Chen et al., 2001).

Despite these advances, many hydrologic simulations continue to represent subsurface saturated hydraulic conductivity using one-dimensional parameterizations, commonly assuming either constant values within layers or monotonic vertical decay functions. Such approaches are rooted in classic observations of declining saturated hydraulic conductivity with soil depth (e.g., Beven, 1984; Elsenbeer et al., 1992) and remain widespread due to their simplicity and limited data requirements. However, growing geophysical and hydrologic evidence indicates that these 1-D representations fail to capture the true three-dimensional complexity of the CZ, particularly in steep, weathered and fractured terrain where lateral contrasts in permeability can dominate subsurface flow paths and pore-pressure evolution.

Recent work further suggests that this three-dimensional heterogeneity is strongly influenced by topography-induced stress fields. Geophysical imaging and mechanical modeling show that extensional stresses near ridges promote fracture development, enhanced weathering, and elevated permeability, whereas compressional stresses in valleys tend to suppress fracturing and reduce fluid flow (St. Clair et al., 2015). Moreover, physically based models of 3-D topographic stresses provide a mechanistic framework linking landscape form to fracture density, weathering depth, and hydraulic properties (Moon et al., 2017; Moon et al. 2020). These stress-controlled variations generate pronounced lateral and vertical contrasts in CZ hydraulic properties that cannot be captured by depth-only parameterizations, yet are critical for understanding hillslope hydrology and landslide initiation.

This work aims to improve hydrological and landslide simulations of the CB1 landslide (1996) by representing subsurface saturated hydraulic conductivity (k_s) as a function of CZ properties inferred from field geophysics and topographic stress modeling, rather than prescribing constant k_s values for CZ layers as adopted in previous studies (e.g., Formetta et al. (submitted); Moon et al. (under review)). The 3-D variability of CZ k_s is constrained using: (i) a dataset comprising hundreds of slug tests conducted in piezometers, (ii) near-surface seismic refraction surveys, and (iii) modeled topographic stresses. This integrated framework is referred to throughout the chapter as the "$k_s - p_v - \sigma$" relationship. The resulting spatially variable k_s field is used to parameterize the subsurface hydrologic properties of the GEOtop 3-D hydrologic model (Rigon et al. 2006) and to simulate the rainfall event that triggered the 1996 CB1 landslide. Slope failure is addressed with a multi-dimensional slope stability model combined with spectral search algorithm (Milledge et al. 2014; Bellugi et al. 2015a). Results obtained using the $k_s - p_v - \sigma$ approach are compared against two commonly adopted alternatives: a classical one-dimensional exponential decay of hydraulic conductivity with depth ("$k_s - z$") and a spatially uniform hydraulic conductivity ("$k_s - const$").

5.2 Study area

The CB1 experimental catchment (Fig. 23) is an 860 m² zero-order basin located on Mettman Ridge in the Oregon Coast Range (Fig. 23-a), 15 km north-northeast of Coos Bay (Ebel et al. 2007b; Anderson et al. 2002; Borja and White 2010; Montgomery et al. 1997). This catchment contributes to a first-order stream and is typical of the steep, soil-covered headwater hollows found in the Coast Range, where land sliding is a major geomorphic process (Dietrich and Dunne 1978; Dietrich et al. 1986; Montgomery et al. 2000). The average annual precipitation in the area is about 1500-1600 mm, mostly falling during the winter months (Haagen 1989; Taylor et al. 2005).

The CB1 catchment is an unchanneled valley with converging bedrock topography and an average slope of about 40-45° (e.g., Anderson et al. 2002; Borja and White 2010) located in the upper portion of a larger catchment called B1 (Fig. 23-b). Soil depth (Fig. 23-c) varies widely across the site. It ranges from around 0.5 m on topographic noses to nearly 2 m along the hollow axis (Montgomery et al. 1997). The soil layer consists of colluvium derived from local bedrock. It mainly contains well-mixed, gravelly silty sands that have low plasticity (Haagen 1989; Borja and White 2010). Long-term erosion rates of 0.05-0.08 mm per year over the last 4-15 ka closely match uplift rates, suggesting a rough dynamic balance at landscape scales (Reneau and Dietrich 1991).

The near-surface bedrock is variably weathered and fractured, creating a shallow fractured zone that is crucial for subsurface stormflow. In contrast, the deeper bedrock is relatively solid and less permeable (Montgomery et al. 1997, 2002). Ridge borehole shows that weathered bedrock is composed of pervasively oxidized rock down to 4.5 m depth, and fractured oxidized rock down to 9 m depth; below the subsurface is considered unweathered fresh bedrock (Anderson et al. 2002).

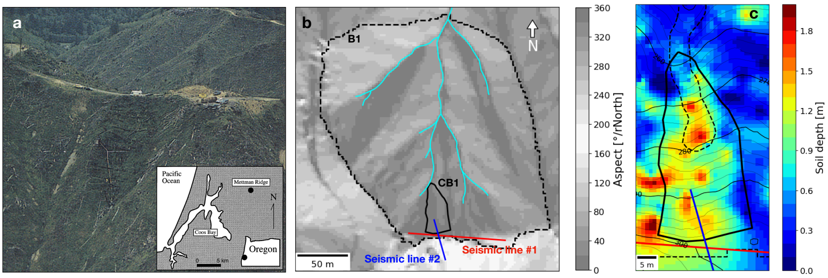

Figure 23. (a) Aerial photo of CB1 catchment and inset showing its location in Mettman Ridge, Coosbay, Oregon (from Montgomery et al. 1997). (b) B1 catchment outline (dashed black line) with channel network (cyan line); at the ridge are shown the experimental catchment CB1 (black bold line), and the two seismic refraction survey lines (red and blue bold lines). (c) Soil depth map and 1996 landslide scar (dashed black line). Bottom left corner maps coordinates in (c) are (x,y)=(410002,4812902.5) in EPSG:26910 reference system.

Instrumentation at the CB1 catchment began in late 1989 and continued until November 1996, when an extreme storm triggered a debris flow that destroyed much of the site (Anderson et al., 1997, 2002; Montgomery et al., 1997; Montgomery et al., 2009). The site was equipped with a dense network of rain gauges, piezometers, tensiometers, time-domain reflectometry probes, lysimeters, meteorological sensors, and weirs, making CB1 one of the most intensively monitored steep, deforested catchments to date (Ebel et al., 2007a). Observations from natural storms and controlled sprinkling experiments showed that runoff generation at CB1 was dominated by subsurface stormflow within a shallow fractured bedrock zone, with additional contributions from vadose-zone percolation (Montgomery et al., 1997, 2002; Torres et al., 1998). In mid-November 1996, an extreme rainfall event delivered approximately 225 mm of precipitation, with peak intensities reaching ~40 mm/h and 24 and 48-hour average rainfall rates of 145 mm/day and 85 mm/day, respectively (Montgomery et al., 2009). This storm caused a shallow landslide on November 18 between 19:50 and 20:00 (Fig. 23-c), resulting in extensive instrument loss and removal of colluvial soils down to bedrock in the upper portion of the failure scar (Montgomery et al., 2009). The exposed bedrock surface at the base of the scar was smooth and exhibited three visible fractures that allowed water to drain from beneath the soil following failure. Notably, 15 automated piezometer nests within the hollow successfully recorded pore water pressures at the soil-bedrock interface immediately prior to landslide initiation

5.3 Data and Methods

5.3.1 $k_s - z$ scenario

A comprehensive dataset of k_s was obtained from 177 falling-head slug tests conducted in piezometers installed at the CB1 site, subdivided by 118 tests in colluvial soil and 59 tests in weathered bedrock. These measurements were collected during sprinkling experiments performed in 1990 and 1992 (Montgomery et al., 2002; Montgomery et al., 2009). The slug test data were reanalyzed using the Bouwer and Rice (1976) method, and a summary of the reprocessed results is presented in Ebel et al. (2007a).

The measurements reveal a clear decrease in k_s with z in both colluvial soil and weathered bedrock (Fig. 24). k_s values span four orders of magnitude, ranging from approximately 10^{-7} to 10^{-3} m/s (Fig. 24-a). Soil measurements were obtained at depths between 0 and 2 m, whereas weathered bedrock measurements extend from approximately 0.5 to 3 m depth (Fig. 24-b). Empirical cumulative distribution functions (ECDFs, Fig. 24-c) indicate greater variability in within the soil layer around 10^{-4} m/s and within the weathered bedrock layer between 10^{-6} and 10^{-5} m/s. A small number of weathered bedrock measurements near the outlet exhibit relatively high k_s (>10^{-4} m/s), likely reflecting localized zones of fracturing around the channel head. A vertical trend is visible for the two layers, but there is no visible dependence of $k_s$with the distance from channel head, i.e., CB1 outlet where an upper weir is installed.

To parameterize the depth dependence of k_s, we adopt the commonly used exponential decay relationship (e.g., Cabral et al. 1992; Ameli et al. 2016):

$$k_s(z) = k_{s,0} \cdot e^{-\frac{z}{r}} \tag{1}$$

where $k_{s,0}$ [m/s] and r [m] are fitting parameters.

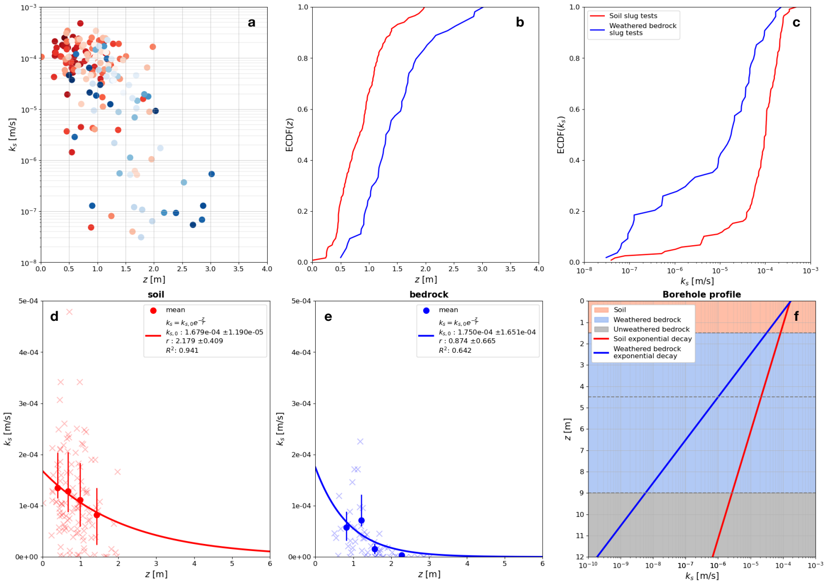

Figure 24. (a) Scatter plot of falling head slug tests into CB1 piezometers showing sample depth and estimated saturated hydraulic conductivity for soil (in red) and weathered bedrock (in blue). Colors get darker as distance from CB1 outlet increases. (b) ECDF of slug test depths. (c) ECDF of slug test saturated conductivities. (d), (e) Exponential decay of k_s *with z, obtained using four depth mean bins defined by the 25th-percentile interval, for soil and weathered bedrock respectively. (f)* k_s *profiles at the borehole location; horizontal dashed lines indicate the boundaries of soil, oxidized rock and oxidized-fractured rock. "x" markers are raw data.*

The exponential fits were obtained by binning the data for each layer into four depth bins defined by the 25th-percentile intervals, ensuring an equal number of observations per bin. Least-squares regression was then applied to the mean binned data. Results are shown in Fig. 24-d,e,f, which includes the individual measurements, binned values with error bars, fitted $k_s - z$ relationships for each layer, estimated parameters with associated uncertainties, and the regression correlation coefficient

(R^2). The $k_s - z$ formulation provides a reasonable description of the observed depth trends, with R^2 values of 0.94 for soil and 0.64 for weathered bedrock. Within the weathered bedrock layer, k_s values vary between approximately 10^{-10} and 10^{-4} m/s. These values are consistent with bounds identified by Ebel et al. (2007a), who reported mean k_s values of ~$7 \cdot 10^{-5}$ m/s for thin saprolite and ~$5 \cdot 10^{-7}$ m/s for underlying oxidized-fractured bedrock, as well as with the value of 10^{-10} m/s predicted for fresh bedrock by Rempe and Dietrich (2014).

In this scenario, the CZ is subdivided into three layers: soil, weathered bedrock (WB), and unweathered bedrock (UB). Soil thickness was estimated using kriging interpolation based on 195 colluvial soil-depth measurements from soil borings (Schmidt, 1999). For the weathered bedrock layer, we adopt the CZ(RD9m) conceptual model previously used by Moon et al. (under review) and Formetta et al. (submitted), which is based on the drainage model of Rempe and Dietrich (2014). In this framework, the WB-UB boundary is represented by a sloping surface extending from exposed bedrock at the channel head to greater depths upslope, corresponding to the ~9 m depth at which fracture closure was observed at ridge borehole (Anderson et al., 2002). The same CZ configuration is adopted also for $k - const$, while we assume k_s=$1.1 \cdot 10^{-4}$,$7 \cdot 10^{-5}$ [m/s] for soil and WB respectively, as mean values indicated in Ebel et al. (2007b).

5.3.2 $k_s - \mathrm{v_p} - \sigma$ scenario

<u>Seismic data</u>

Seismic refraction surveys were conducted along two lines (Fig. 23-b) using 24-channel seismographs with 1 m geophone spacing and 3 m shot intervals. One second of data was recorded at a millisecond sample rate for each shot, with off-end shots included. P-wave (v_p) arrival times were manually identified and processed through a Bayesian inversion to generate seismic velocity profiles. More details are available in Higa (2023). The results of the seismic inversion are presented for two CB1 cross sections in Fig. 25: the “ridge-CB1 profile” (Seismic line #1) shows a 96 m-long and 35 m-deep v_p field at the CB1 ridge; the “cross-CB1 profile” (Seismic line #2) shows instead a 40-long 20 m-deep v_p field on the opposite direction (~70-degree rotation). The intersection point of the profiles closely coincides with the location of the borehole reported by Anderson et al. (2002).

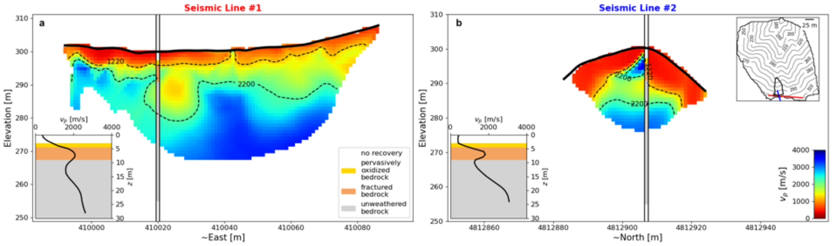

Figure 25. (a) Seismic Line #1 tomogram at the ridge; the inset shows the vertical profile at borehole location. (b) The same for Seismic Line #2 profile across the upper portion of CB1.

v_p surveys conducted across the upper part of CB1 catchment revealed seismic velocities ranging from 400 to 3500 m/s, providing a detailed map of the subsurface structure. In the shallowest layers (Fig. 25-a), velocities around 500 m/s correspond to the surface soil, while the transition to weathered saprolite and fractured bedrock occurs as velocities increase toward 1220 m/s. These shallow velocity contours generally run parallel to the ground surface. In contrast, the deeper transition to unweathered bedrock, characterized by velocities exceeding 2200 m/s, features significant undulations that do not follow the surface topography. These deep variations, with amplitudes between 10 and 15 meters, appear to correlate with the locations of topographic spur ridges rather than the surface slope. Additionally, comparisons between the intersecting survey line (Fig. 25-b) indicate that seismic anisotropy is present, particularly at a depth of 6 meters, where v_p shows noticeable variability that may be influence by fracture orientation, since seismic velocities are decreased in a direction normal to the plane of the cracks (e.g., Anderson et al. 1974). Inset panels at the borehole location shows that around 9 m the v_p decreases, to increase again progressing downward in the unweathered bedrock.

Stress data

We model spatial variations in CZ 3-D topographic stress calculations based on methods developed by St. Clair et al. (2015) and Moon et al. (2017). This method shows subsurface stresses as the combined effects of tectonic compression, gravitational loading, and topographic changes, assuming linear-elastic and uniform rock properties. Model is calibrated using 14 regional in-situ stress measurements from the World Stress Map (Heidbach et al., 2019). Linear least squares regression is used to derive best-fit profiles for maximum horizontal, minimum horizontal, and vertical stresses, which define the overall tectonic stress state. A 2 m-resolution LiDAR DEM of Coos Bay is then used to compute the topographic stress field. We convert the DEM into a triangular mesh with variable element sizes to balance resolution and computational efficiency. Stresses are evaluated on a three-dimensional observation grid with 5 m horizontal and 3 m vertical spacing, extending to about 100 m depth. Finally, the total stress field beneath the site is simulated using the boundary element model Poly3D (Thomas, 1993), assuming linear-elastic, uniform, and isotropic material behavior. In this study, the least compressive stress (σ:LCS) is used as a proxy for bedrock fracture openness across the entire site, with compressive stresses taken as positive and tensile stresses as negative. Further details are provided in Higa (2023) and Moon et al. (under review). LCS results for the entire domain, as well as selected North-South and East-West transects, are presented in Fig. S19 in the Supplementary Material. Some transects show a characteristic “bowtie” pattern in which the LCS field shows lower compressive stresses beneath ridges and higher compressive stresses in valleys, producing a concavity in the LCS field that is opposite to the topographic surface.

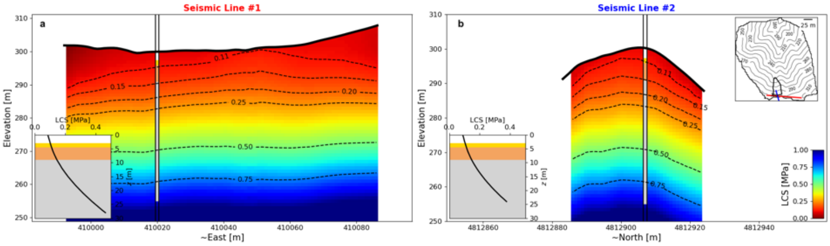

Figure 26. (a) Seismic Line #1 LCS field at the ridge; the inset shows the vertical profile at borehole location. (b) The same for Seismic Line #2 profile across the upper portion of CB1.

Processing

The first step is to generate a catchment-wide field of v_p. Since seismic measurements are limited to the upper ridge of CB1, it is necessary to establish a relationship linking v_p to the LCS and extrapolate these values across the entire CB1. This, in turn, will be used to determine a relationship between hydraulic conductivity and seismic velocity at slug test locations, which is also inherently a function of the stresses. In principle, if a sufficiently extensive v_p dataset is available, this extrapolation step would be unnecessary for local-scale applications, but would still be required for regional-scale characterization (e.g., B1 catchment). The procedure adopted here is as follows.

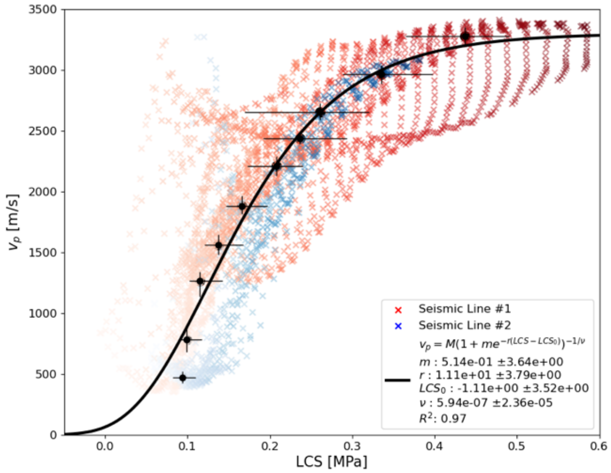

Figure 27. Least squares regression of seismic velocity as function of least compressive stresses $v_p = v_p(LCS)$*. The data are binned such that each 10% quantile contains an equal number of points for Seismic lines #1 and #2 together.*

LCS field is initially interpolated to the seismic profiles grid points (Fig. 26). We then identify a relationship that satisfies the condition that v_p increases with LCS, consistent with the observation that seismic velocity is higher in unfractured bedrock. A Richards logistic function (Richards, 1959) is fitted to describe the growth of v_p as a function of LCS. This function is advantageous because it is bounded by an upper limit, does not follow a symmetric S-shape, and remains valid for negative LCS values while ensuring $v_p > 0$:

$$v_p = \mathrm{M}\left(1 + me^{-r(LCS-LCS_0)}\right)^{-1/\nu} \tag{2}$$

Here, M=3300 m/s represents the maximum bedrock-representative seismic velocity, beyond which v_p does not increase with LCS as fractures close and rocks becomes intact. A single curve representative of the two seismic profiles is computed. The data are binned such that each 10% quantile contains an equal number of points. The resulting relationship, including all points, bins, error bars, and the correlation coefficient, is shown in Fig. 27. The curve exhibits a steep increase between 0.1-0.25 MPa and 500-2500 m/s, then flattens for higher LCS values. Equation (2) is subsequently used to extrapolate v_p across the LCS grid. Fig. 28 shows the results for the North-South cross section through CB1 hollow. The ridgetop of CB1 exhibits lower velocities at depth, while the outlet (the valley) higher velocities at shallow depth under the channel.

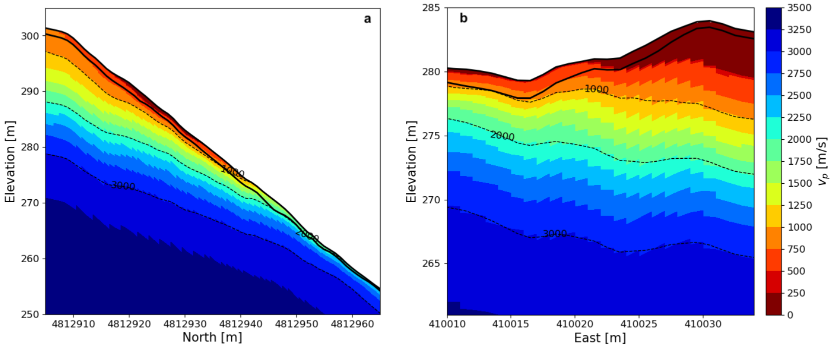

Figure 28. Extrapolated seismic velocity field. (a) North-South view across CB1 hillslope. (b) East-West view across CB1 landslide scar.

Finally, at each slug test location, trilinear interpolation is applied to obtain a weighted average of the surrounding v_p cells for each k_s sampling point. The relationship between k_s and v_p is modeled as a linear relationship between seismic velocity and log-transformed conductivities:

$$log k_s = a + b \cdot v_p \tag{3}$$

where a, b are fitting parameters. The result of the regression is displayed in Fig. 29. The linear fits were obtained by binning the data for each layer into four depth bins defined by the 25th-percentile intervals, ensuring an equal number of observations per bin. For this scenario the R^2 for WB (0.96) is much greater than the soil (0.38). A more explicit and systematic relationship between hydraulic conductivity and seismic velocity is expected in weathered bedrock and fractured bedrock than in soils because both properties are primarily controlled by fracture density and aperture. In bedrock, increases in effective stress and crack closure simultaneously increase seismic velocity and reduce fracture permeability, leading to a well-defined inverse relationship between k_s and v_p. In contrast, soil hydraulic conductivity is strongly influenced by macroporosity, biological activity, and textural heterogeneity, which are only weakly captured by seismic velocity measurements. As a result, the $k_s - p_v - \sigma$ relationship in soils is typically more scattered and less predictive than in fractured bedrock.

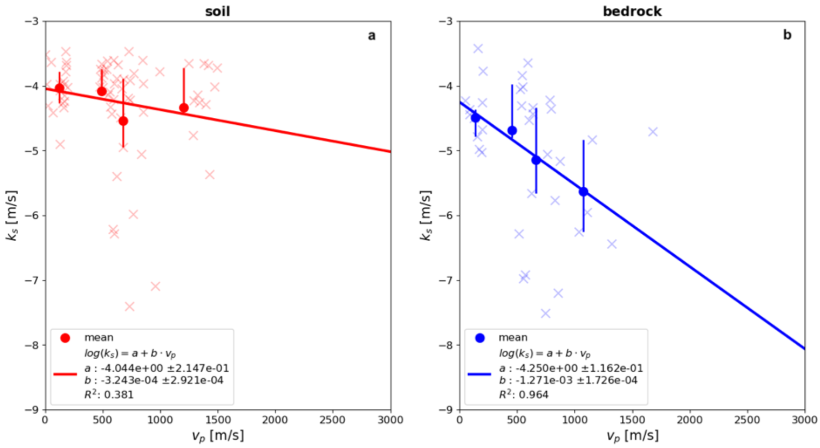

Figure 29. Linear decay of $log(k_s)$ *with* v_p *infered from LCS, obtained using four depth mean bins defined by the 25th-percentile interval, for soil (a) and weathered bedrock (b) respectively. "x" markers are raw data.*

For this scenario, the CZ is only subdivided into two layers: soil and bedrock. No UB is imposed and the transition from WB to UB occurs smoothly, governed by the $k_s - p_v - \sigma$ decay rather than an abrupt change from a permeable to impermeable layer.

5.4 Numerical simulations

5.4.1 Hydrological modeling

The GEOtop model (Rigon et al., 2006) was used to simulate the three-dimensional coupled surface-subsurface hydrological of CB1 hillslope.

Surface runoff and hillslope flow are simulated using de Saint-Venant equation, while subsurface flow is modeled by solving the 3-D Richards equation for variably saturated conditions. Soil hydraulic properties were parameterized using the Van Genuchten formulation, with values prescribed separately for soil and bedrock. Specifically, we use θ_s=0.5,0.15 [-], θ_r=0.18,0.08 [-], α=18,4 [1/m], n=2.8,1.25, for soil and bedrock, respectively, following the values reported in Ebel et al. (2007b) and Torres et al. (1998), and used in Formetta et al. (submitted) and Moon et al. (under review). For each hydraulic conductivity scenario, i.e., $k_s - const$, $k_s - z$, $k_s - p_v - \sigma$, a hydrological simulation of the landslide event is performed, for a total of three tests. Fig. 30 shows the comparison between the three used k_s fields for the hydrological simulations. The CB1 digital elevation model was generated by kriging 630 elevation measurements (Ebel et al. 2007b), producing a 1 m resolution surface grid. The soil map is based on 195 measurements of colluvial soil depth from soil borings (Schmidt, 1999) The subsurface was discretized using vertically variable layer thicknesses, with finer resolution (0.05 m) in the upper 4 m and progressively coarser layers at depth. A horizontal impermeable boundary was imposed at a depth of 40 m below the outlet. Lateral boundaries were treated as impermeable, except along the northern boundary where both surface and subsurface outflow were permitted.

5.4.2 Landslide modeling

We used a multidimensional slope stability model combined with a spectral search algorithm to predict the occurrence of discrete shallow landslides, their sizes and locations based on the stability of clusters of grid cells (Milledge et al., 2014; Bellugi et al., 2015a; Bellugi et al., 2015b). The model represents the landscape as a graph, with vertices for soil columns and edges for the forces between them. Using a spectral graph-theoretical approach for image segmentation, the algorithm separates the graph by minimizing the ratio of resisting to driving forces within each cluster. This generates clusters of soil columns that may fail as shallow landslides. Predicted failures are assumed to mobilize the full soil column down to the soil-bedrock interface. The model assumes rigid-block Mohr-Coulomb failure along a plane parallel to the soil-bedrock interface. Under this assumption, the model performs a force balance considering gravity- driven driving forces, resistive forces from friction and root cohesion, and earth pressures on landslide boundaries. Specifically, it computes: lateral resisting forces R_l, resisting forces on downslope faces R_d, net driving forces on upslope faces R_u, basal shear resisting forces R_b, and basal driving forces F_b. Basal driving and resisting forces are modified from Milledge et al. (2014) to include the non-slope-parallel seepage forces, i.e., i [-] flux gradient and λ [°] seepage angle (Iverson and Major 1986). The factor of safety (FS) of an entire soil cluster is the sum of all resisting forces from all cells divided by the sum of all driving forces from all cells as:

$$FS = \frac{\Sigma_{all} R_b + \Sigma_{lateral} R_l + \Sigma_{down} R_d - \Sigma_{up} R_u}{\Sigma_{all} F_b} \tag{4}$$

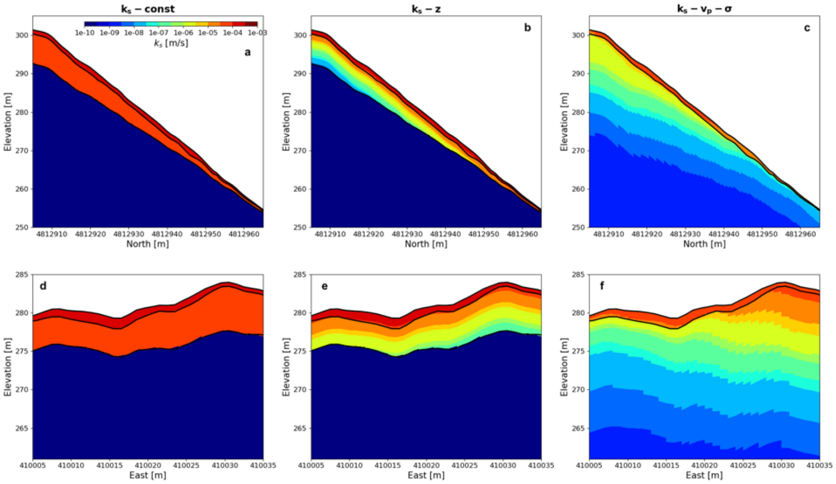

Figure 30. Saturated hydraulic conductivity scenarios: (a,d) constant scenario $k_s - const$; (b,e) depth-decay scenario $k_s - z$; (c,f) seismic-decay scenario $k_s - p_v - \sigma$. Profiles are shown for North-South cross section across CB1 hillslope (a,b,c) and for East-West cross section across CB1 landslide (d,e,f). In (a,b,d,e) the weathered-unweathered bedrock boundary is CZ(RD9m).

The identification of discrete soil landslides involves recognizing singular and overlapping clusters of unstable cells (i.e., FS<1). Based on the predicted overlapping clusters of unstable cells, we calculate the relative frequency of potential discrete landslides (RF) by dividing the number of potential discrete landslides occurring in a pixel by the total number of potential landslides across the study area. A higher relative frequency indicates that a higher number of possible discrete landslides are predicted for that pixel. We set the following model parameters: soil density ρ_s=1600 kg/m^3, water density

ρ_w=1000 kg/m^3, friction angle ϕ=40°, a depth-decaying root cohesion according to Schmidt et al. (2001).

5.5 Results and Discussion

Fig. 31 shows: i) the maps of pore water pressure at the soil base, ii) the soil saturation ratio h/z, and iii) the comparison between simulated and observed h/z at the 15 piezometers at the moment of landslide triggering. The h/z ratio is defined as the ratio between pressure at the soil base and soil depth.

The results highlight a clear improvement in the hydrological response of the CZ when heterogeneity in k_s is considered. The $k-const$ scenario shows a limited extent of the saturated area until the central fracture. In contrast, the two scenarios with variable k_s reproduce soil saturation in the upper scar and in the upper portion of the hillslope. Major differences are observed between the pressure and h/z maps obtained with the k_s-z and $k_s-v_p-\sigma$ scenarios, mainly in the central-lower portion of the hillslope.

The $k_s-v_p-\sigma$ scenario shows a slight overestimation of h/z at the piezometers located around the central fracture compared to the k_s-z scenario. This behavior is mainly attributed to the seimic velocity dataset confined to the ridgetop. The extrapolation of v_p from LCS outside this region may lead to misleading results towards the landslide scar and at the CB1 outlet, as the original dataset mainly represents conditions at the ridge and not at the outlet in the valley. This limitation is related to differences in the stress field between these areas. At the ridge, stress isolines tend to be parallel to the surface, whereas at the outlet they present more complex patterns, including bowtie shapes and compressional stresses. As a consequence, the $k_s-v_p-\sigma$ field estimates lower conductivities at the outlet compared to k_s-z (Fig. 30). This feature promotes saturation within the soil rather than subsurface flow in the WB. Despite this limitation, the $k_s-v_p-\sigma$ provides a better prediction of h/z in the upper part of the hillslope compared to k_s-z.

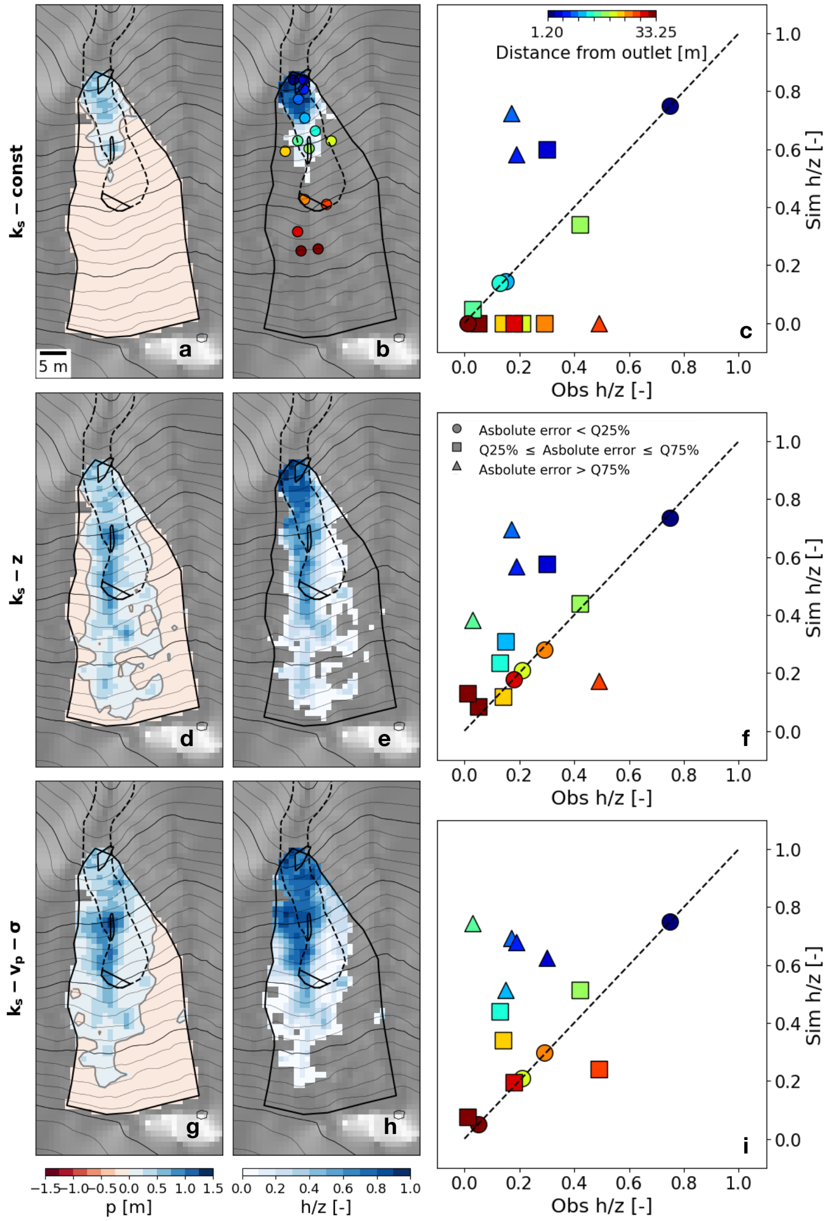

Figure 31. $k_s - const$ results: (a) pore water pressure at soil base; (b) soil saturation ratio h/z; (c) comaprison between observed and simulated h/z in the piezometers. Maps and points are presented at the moment of hillslope failure. The piezometers are colored by the distance from the CB1 outlet, why their shape in (c) is based on the quantiles of the absolute error between measurements and simulations. (d,e,f) The same for $k_s - z$. (g,h,f) The same for $k_s - v_p - \sigma$. The dashed-black line is the 1996 landslide scar, and the three black patches are the fractures exposed after the event. Background is the aspect.

The saturation extent of $k_s - v_p - \sigma$ is also wider than $k_s - z$. This result is mainly attributed to the spatial distribution of the k_s field. As shown in Fig. 30, $k_s - v_p - \sigma$ depends on the seismic velocity, which is also function of LCS, that follows the spatial pattern of LCS and has higher conductivities in WB under the eastern drainage divide of CB1. In contrast, $k_s - z$ is only depth-dependent and the 3-D spatial distribution is consequence of the topographic gradient. During low-to-medium persistent rainfall, water is likely to move toward more conductive regions outside the CB1 hollow in $k_s - v_p - \sigma$, while in $k_s - const$ and $k_s - z$ subsurface flow is mainly driven by slope. Acquiring seismic data across the entire CB1 catchment would significantly enhance characterization of the CZ at the outlet and improve understanding of how variable source areas influence streamflow generation (Anderson et al. 1997). At present, this area remains uncertain due to limited extention of measured v_p (Fig. 25) and field information on fracture openings and density. Seismic refraction tomography could provide the necessary resolution in the lower part of the hillslope, where also slug tests have not detected significant variations in soil and WB k_s between the channel head and the mid-to-upper hillslope (Fig. 24).

Fig. 32 shows the map of λ at the soil-bedrock interface and the map of RF in log scale. λ indicates the direction of hydraulic gradient with respect to the soil base normal: 0° is the upward normal direction, 180° is the downward normal direction, λ<90° means exfiltration from bedrock (upward flux), λ ~90° means slope-parallel flux, λ>90° means infiltration (downward flux). Results for λ show no particular exfiltration inside the landslide scar for $k_s - z$. On the contrary, for $k - const$ and $k_s - v_p - \sigma$ a distinct exfiltration pattern (λ=60-70) from the WB is visible around the central fracture. This area is larger for $k_s - v_p - \sigma$ and covers a large portion of the upper scar. Exfiltration is considered playing an important role destabilizing the soil layer at CB1 (Montgomery et al. 1997; Montgomery et al. 2002), and the fractures opened after the landslide event have been acknolewdged as localized areas of exfiltration of fracture flow from the scarp (Montgomery et al. 2009).

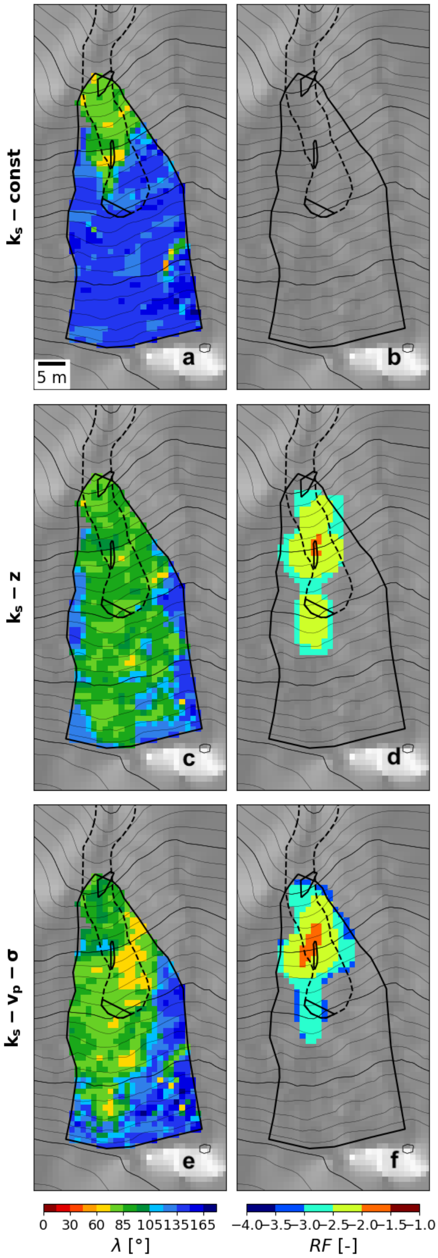

Figure 32. $k_s - const$ results: (a) seepage vector at soil-bedrock interface; (b) relative frequency of discrete landslides. (c,d) the same for $k_s - z$. (e,f) the same for $k_s - v_p - \sigma$. The dashed-black line is the 1996 landslide scar, and the three black patches are the fractures exposed after the event. Background is the aspect.

No landslide occurs in $k - const$, because soil saturation is not intense and spread enough to make the hillslope unstable. The variable k_s scenarios instead exhibit hillslope failure. The unstable area covers tha landslide scar end eventually a small portion above the crown. Both cases show a higher RF in the central fracture corresponding to a higher concentration of predicted discrete landslide per pixel. This can be seen also as the potential triggering point for failure. The landslide area is a little shifted to the left compared to expectations. This can also be seen in the h/z and pressure map where soil saturation and higher pressure develop along the vertical axis of CB1, which is shifted on the left of the upper scar where the deepest soil pits are found. $k_s - z$ overpredicts landslide frequency and area uphillslope compared to $k_s - v_p - \sigma$.

5.6 Conclusions

This study explored the heterogeneity within the CZ at the CB1 experimental catchment. By incorporating variations in the hydraulic conductivity of subsurface layers, hydrological and landslide simulations demonstrated that saturation development in the soil depends heavily on the spatial pattern of the hydraulic conductivity field in both the soil and bedrock, which in turn significantly influences landslide prediction. The analysis indicated that assuming constant conductivity ($k - const$) is insufficient to characterize the hydro-mechanical response of the hillslope compared to variable conductivity scenarios. Specifically, the scenario based on the depth-dependent decay of conductivity ($k_s - z$) and the scenario defined as a function of field seismic velocity and topographic stresses ($k_s - v_p - \sigma$) both showed improved results regarding saturation development and landslide prediction.

The methodology presented a novel approach to predicting 3D variations in hydraulic conductivity based on a field of seismic velocity inferred with modeled topographic stresses, offering a promising physically-based solution for characterizing the CZ in larger basins at a regional scale.

References

Ackerer, J., Kuppel, S., Braud, I., Pasquet, S., Fovet, O., Probst, A., Pierret, M. C., Ruiz, L., Tallec, T., Lesparre, N., et al. (2023). Exploring the Critical Zone Heterogeneity and the Hydrological Diversity Using an Integrated Ecohydrological Model in Three Contrasted Long-Term Observatories. Water Resources Research, 59(12), e2023WR035672.

Ameli, A. A., McDonnell, J. J., and Bishop, K. (2016). The exponential decline in saturated hydraulic conductivity with depth: A novel method for exploring its effect on water flow paths and transit time distribution. Hydrological Processes, 30 (14), 2438-2450.

Anderson, D. L., Minster, B., and Cole, D. M. (1974). The effect of oriented cracks on seismic velocities. Journal of Geophysical Research Atmospheres, 79 (26), 4011-4015.

Anderson, S. P., Dietrich, W. E., Montgomery, D. R., Torres, R., Conrad, M. E., and Loague, K. (1997). Subsurface flow paths in a steep, unchanneled catchment. Water Resources Research, 33 (12), 2637-2653.

Anderson, S. P., Dietrich, W. E., and Brimhall, G. H. (2002). Weathering profiles, mass-balance analysis, and rates of solute loss: Linkages between weathering and erosion in a small, steep catchment. Geological Society of America Bulletin, 114(9), 1143-1158.

Bellugi, D., Milledge, D. G., Dietrich, W. E., Perron, J. T., and McKean, J. (2015a). Predicting shallow landslide size and location across a natural landscape: Application of a spectral clustering search algorithm. Journal of Geophysical Research: Earth Surface, 120, 2552-2585.

Bellugi, D., Milledge, D. G., Dietrich, W. E., McKean, J. A., Perron, J. T., Sudderth, E. B. and Kazian, B. (2015b). A spectral clustering search algorithm for predicting shallow landslide size and location. Journal of Geophysical Research: Earth Surface, 120: 300-324.

Beven, K. J. (1984). Infiltration into a class of vertically nonuniform soils. Hydrologic Sciences Journal, 29, 425-434.

Borja, R. I., and White, J. A. (2010). Continuum deformation and stability analyses of a steep hillside slope under rainfall infiltration. Acta Geotechnica, 5, 1-14.

Bouwer, H., and Rice, R. C. (1976). A slug test for determining hydraulic conductivity of unconfined aquifers with completely or partially penetrating wells: Water Resources Research, 12, 423-428.

Brönnimann, C., Stähli, M., Schneider, P., Seward, L., and Springman, S. M. (2013). Bedrock exfiltration as a triggering mechanism for shallow landslides. Water Resources Research, 49(9), 5155-5167.

Brooks, P. D., Chorover, J., Fan, Y., Godsey, S. E., Maxwell, R. M., McNamara, J. P., and Tague, C. (2015). Hydrological partitioning in the critical zone: Recent advances and opportunities for developing transferable understanding of water cycle dynamics. Water Resources Research, 51(9), 6973-6987.

Cabral, M. C., Garrote, L., Bras, R. L., and Entekhabi, D. (1992). A kinematic model of infiltration and runoff generation in layered and sloped soils. Advances in Water Resources, 15, 311-324

Cassiani, G., Böhm, G., Vesnaver, A., Nicolich, R. (1998). A geostatistical framework for incorporating seismic tomography auxiliary data into hydraulic conductivity estimation. Journal of Hydrology, 206, 58-74.

Chen, H., Niu, Q., McNamara, J. P., and Flores, A. N. (2024). Influence of subsurface critical zone structure on hydrological partitioning in mountainous headwater catchments. Geophysical Research Letters, 51, e2023GL106964.

Chen, J., Hubbard, S., and Rubin Y. (2001). Estimating the hydraulic conductivity at the South Oyster Site from geophysical tomographic data using Bayesian techniques based on the normal linear regression model. Water Resources Research, 37 (6), 1603-1613.

Chorover, J., Derry, L. A., and McDowell, W. H. (2017). Concentration-discharge relations in the critical zone: Implications for resolving critical zone structure, function, and evolution. Water Resources Research, 53(11), 8654-8659.

da Silva, A. C., Resende, I., da Costa, R. C., Uagoda, R. E. S., & Avelar, A. d. S. (2022). Geophysical for granitic joint patern and subsurface hydrology related to slope instability. Journal of Applied Geophysics, 199, 104607.

Dietrich, W. E., and T. Dunne (1978). Sediment budget for a small catchment in mountainous terrain. Z. Geomorphol. Suppl., 29, 191-206.

Dietrich, W. E., Wilson, C. J., and Reneau, S. L. (1986). Hollows, colluvium, and landslides in soil-mantled landscapes. Hillslope Processes, 361-388.

Ebel, B. A., Loague, K., Dietrich, W. E., Montgomery, D. R., Torres, R., Anderson, S. P., and Gianbelluca, T. W. (2007a). Near-surface hydrologic response for a steep, unchanneled catchment near Coos Bay, Oregon: 1. Sprinkling eperiments. American Journal of Science, 307 (4), 678-708.

Ebel, B. A., Loague, K., Vandwerkwaak, J. E., Dietrich, W. E., Montgomery, D. R., Torres, R., and Anderson, S. P. (2007b). Near-surface hydrologic response for a steep, unchanneled catchment near Coos Bay, Oregon: 2. Physics-based simulations. American Journal of Science, 307 (4), 709-748.

Ellefsen, K. J., Hsieh, P. A., and Shapiro, A. M. (1999) Relation between Seismic Velocity and Hydraulic Conductivity at the USGS Fractured Rock Research Site. Morganwalp, D.W., and Buxton, H.T., eds., U.S. Geological Survey Toxic Substances Hydrology Program-Proceedings of the Technical Meeting, Charleston, South Carolina, March 8-12, 1999. U.S. Geological Survey Water-Resources Investigation Report 99-4018C, 3, 735-745.

Elsenbeer, H., Cassel, K., and Castro, J. (1992). Spatial analysis of soil hydraulic conductivity in a tropical forest catchment. Water Resources Research, 28, 3201-2143.

Haagen, J. T. (1989). Soil Survey of Coos County, Oregon, 269 pp., Natl. Cooper. Soil Surv., Washington, D. C.

Heidbach, O., Rajabi, M., Reiter, K., and Ziegler, M. (2019). World Stress Map. In R. Sorkhabi (Ed.), Encyclopedia of Petroleum Geoscience. Springer Nature Switzerland AG.

Higa, J. T. (2023). Multi-scale investigations on the impacts of geologic fractures. Phd Thesis, UCLA, Los Angeles, USA.

Holbrook, W. S., Riebe, C. S., Elwaseif, M., L. Hayes, J., Basler-Reeder, K., L. Harry, D., Malazian, A., Dosseto, A., C. Hartsough, P. and W. Hopmans, J. (2014). Geophysical constraints on deep weathering and water storage potential in the Southern Sierra Critical Zone Observatory. Earth Surface Processes and Landforms, 39, 366-380.

Holbrook, S., Marcon, V., Bacon, A., Brantley, S., Carr, B., Flinchum, B., Richter, D., and Riebe, C. (2019). Links between physical and chemical weathering inferred from a 65-m-deep borehole through Earth’s critical zone. Scientific Reports, 9, 4495.

Hyndman, D. W., Harris, J. M., and Gorelick, S. M. (2000). Inferring the relation between seismic slowness and hydraulic conductivity in heterogeneous aquifers. Water Resources Research, 36 (8), 2121-2132.

Iverson, R. M. (2000). Landslide triggering by rain infiltration. Water Resources Research, 36(7), 1897-1910.

Leonarduzzi, E., McArdell, B. W., and Molnar, P. (2021). Rainfall-induced shallow landslides and soil wetness: Comparison of physically based and probabilistic predictions. Hydrology and Earth System Sciences, 25, 5937-5950.

Li, W. C., Dai, F. C., Wei, Y. Q., Wang, M. L., Min, H., and Lee, L. M. (2016). Implication of subsurface flow on rainfall-induced landslide: a case study. Landslides, 13, 1109-1123.

Lin, H. (2010). Earth's Critical Zone and hydropedology: concepts, characteristics, and advances. Hydrology and Earth System Sciences, 14(1), 25-45.

Liu, H., Zhang, J., Liao, A., Liu, C., Du, M., Huang, A., Liang, C., Sun, Z., Guo, J., and Wang, G.(2022). Estimation of variability in soil water content in a forested critical-zone experimental catchment in Eastern China. Journal of Contaminant Hydrology, 248, 104022.

Milledge, D. G., Bellugi, D., McKean, J. A., Densmore, A. L., and Dietrich, W. E. (2014). A multidimensional stability model for predicting shallow landslide size and shape across landscapes. Journal of Geophysical Research: Earth Surface, 119, 2481.2504.

Montgomery, D. R., Dietrich, W. E., Torres, R., Anderson, S. P., Heffner, J. T., and Loague, K. (1997). Hydrologic response of a steep, unchanneled valley to natural and applied rainfall. Water Resources Research, 33(1), 91-109.

Montgomery, D. R., Schmidt, K. M., Greenberg, H., and W. E. Dietrich (2000). Forest clearing and regional landsliding. Geology, 28, 311-314.

Montgomery, D. R., Dietrich, W. E., and Heffner, J. T. (2002). Piezometric response in shallow bedrock at CB1: Implications for runoff generation and landsliding. Water Resources Research, 38 (12), 1274.

Montgomery, D. R., Schmidt, K. M., Dietrich, W. E., and McKean, J. (2009). Instrumental records of a debris flow initiation during natural rainfall: Implications for modeling slop stability. Journal of Geophysical Research: Earth Surface, 114, F01031.

Moon, S., Perron, J. T., Martel S. J., Holbrook, W. S., and St. Clair, J. (2017). A model of three-dimensional topographic stresses with implications for bedrock fractures, surface processes, and landscape evolution. Journal of Geophysical Research: Earth Surface, 122 (4), 823-846.

Moon, S., Perron, J. T., Martel, S. J., Goodfellow, B. W., Mas Ivars, D., Simeonov, A., Munier, R., Näslund, J. O., Hall, A., Stroeven, A. P., Ebert, K., and Heyman, J. (2020). Present-day stress field influences bedrock fracture openness in the deep subsurface. Geophys. Res. Lett., 47, e2020GL090581.

Moon, S., Higa, J. T., Formetta, G., Busti, R., Bellugi, D. G., Dietrich, W. E., Milledge, D. G., and Ebel, B. A. (under review). Deep critical zone controls on shallow landslides. PNAS.

Murielle, G., Roy, C., and Alexia, S. (2011). The influence of plant root systems on subsurface flow: implications for slope stability. Bioscience 61 (11), 869-879.

Parsekian, A. D., Singha, K., Minsley, B. J., Holbrook, W. S., and Slater, L. (2015). Multiscale geophysical imaging of the critical zone. Reviews of Geophysics, 53, 1-26.

Regmi, N. R., Giardino, J. R., McDonald, E. V., and Vitek, J. D. (2015). Chapter 11 - A Review of Mass Movement Processes and Risk in the Critical Zone of Earth. Developments in Earth Surface Processes, 19, 47.

Rempe, D. M. and Dietrich, W. E. (2014). A bottom-up control on fresh-bedrock topography under landscapes, Proceedings of the National Academy of Sciences, 111, 6576-6581.

Rempe, D. and Dietrich, W. E. (2018). Direct observations of rock moisture, a hidden component of the hydrologic cycle. PNAS, 115 (11), 2664-2669.

Reneau, S. L., and Dietrich, W. E. (1991). Erosion rates in the southern Oregon Coast Range: Evidence for an equilibrium between hillslope erosion and sediment yield. Earth Surface Processes and Landforms, 16, 307-322.

Rengers, F. K., McGuire, L. A., and Coe, J. A. (2016). The influence of vegetation on debris-flow initiation during extreme rainfall in the northern Colorado Front Range. Geology 44 (10), 823-826.

Rigon, R., Bertolfi, G., and Over, T. M. (2006). GEOtop: A Distributed Hydrological Model with Coupled Water and Energy Budgets. Journal of Hydrometeorology, 7, 371-388.

Robison, E. G., Mills, K., Paul, J., Dent, L., and Skaugset, A. (1999). Storm impacts and landslides of 1996, Tech. Rep. 4, 145 pp., Oreg. Dep. of For., Salem.

Schmidt, K. M. (1999). Root strength, colluvial soil depth, and colluvial transport on landslide-prone hillslopes. PhD Thesis, University of Washington, Seattle, USA.

Schmidt, K., Roering, J., Stock, J., Dietrich, W., Montgomery, D., and Schaub, T. (2001). The variability of root cohesion as an influence on shallow landslide susceptibility in the Oregon Coast Range. Canadian Geotechnical Journal 38, 995-1024.

Sprenger, M., Stumpp, C., Weiler, M., Aeschbach, W., Allen, S.T., Benettin, P., et al. (2019). The demographics of water: A review of water ages in the critical zone. Reviews of Geophysics, 57 (3), 800-834.

St. Clair, J., Moon, S., Holbrook, W. S., Perron, J. T., Riebe, C. S., Martel, S. J., Carr, B., Harman, C., Singha, K .D. and Richter, D. D. (2015). Geophysical imaging reveals topographic stress control of bedrock weathering. Science, 350(6260), 534-538.

Taylor, G., Hale, C., and Joos, S. (2005). Climate of Coos County, Special report, Oregon Climate Service: Corvallis. Oregon, Oregon State University, 1-4.

Thomas, A. L. (1993). POLY3D: A three-dimensional, polygonal element, displacement discontinuity boundary element computer program with applications to fractures, faults, and cavities in the earth's crust. Stanford University.

Torres, R., Dietrich, W. E., Montgomery, D. R., Anderson, S. P., and Loague K. (1998). Unsaturated zone processes and the hydrologic response of a steep, unchanneled catchment. Water Resources Research, 34 (8), 1865-1879.

Wicki, A., Lehmann, P., Hauck, C., Seneviratne, S. I., and Waldner, P. (2020). Assessing the potential of soil moisture measurements for regional landslide early warning. Landslides, 17, 1881-1896.

Wilson, C. J., and Dietrich, W. E. (1987). The contribution of bedrock groundwater flow to storm runoff and high pore pressure development in hollows. document title: IAHS Publication, 49-59.

Wlostowski, A. N., Molotch, N., Anderson, S. P., Brantley, S. L., Chorover, J., Dralle, D., et al. (2021). Signatures of hydrologic function across the Critical Zone Observatory network. Water Resources Research, 57, e2019WR026635.

Chapter 6: Conclusions

6.1 Research outcomes

This doctoral research advances the understanding of the influence of the Critical Zone (CZ) on hillslope hydrology and stability across different regions, climates and landscapes. The main aim was to improve the physical realism of hydro-mechanical predictions by explicitly representing subsurface architecture, including soil layering, bedrock geometry, weathering state, and three-dimensional heterogeneity, to overcome the standard application of simplified conceptual models.

To overcome these challenges, the thesis integrates multiple data sources and methods, and a combination of field monitoring, laboratory experiments, geophysical surveys, and physically based numerical modeling. The manuscript explored the hydrological response and landslide susceptibility of pyroclastic layered soils in Campania (Southern Italy), alpine terrains in Alto Adige (Northern Italy) and weathered environments in Coos Bay (Oregon, USA). Across these case studies, high-resolution hydrological simulations are coupled with stability analyses to investigate infiltration processes, subsurface flow routing, pore-pressure dynamics, and landslide initiation mechanisms under both controlled experiments and natural rainfall events. This multi-scale, multi-method approach enables a consistent evaluation of how CZ controls hydrological response and slope instability across diverse environments. Each investigated CZ scenario revealed specific results to rainfall forcing, largely controlled by its underlying geomorphological framework and climatic context.

Pyroclastic soil mantles in the Sarno area have been shown as highly layered and anisotropic. The stratification between ashy and pumiceous layers leads to strong contrasts in hydraulic conductivity and water retention, promoting perched water tables and rapid pore-pressure buildup during intense rainfall events. Physically based hydrological modeling, constrained by field and laboratory observations, showed that lateral subsurface flow concentrates along stratigraphic boundaries, controlling instability initiation. These results highlight the necessity of explicitly representing internal soil architecture when assessing landslide susceptibility in volcanic terrains.

The study in the Alto Adige used a physical-based hydro-mechanical framework for assessing hillslope stability with the Local Field Factor of Safety (LFS) and demonstrated its applicability in a complex real-world setting in the Braies catchment. The model successfully captured rainfall-induced landslide initiation, with failure surfaces occurring approximately parallel to the ground at the soil-bedrock interface. The proposed framework, built upon open data and physically based modeling, shows strong potential for transferability to other catchments for regional scale landslide assessment.

The investigation of the CB1 catchment in Coos Bay highlighted how deep CZ regulate hillslope-scale hydrological processes. Model results indicated that the interaction between soil and weathered bedrock governs water storage, streamflow generation, and the development of transient saturation zones. Comparison between different CZ conceptualizations, based on drainage or topographic stress models, demonstrated that realistic representation of bedrock structure is essential to reproduce observed pore-pressure dynamics and runoff response. Further analyses at this site demonstrated that the three-dimensional heterogeneity of the CZ represents a first-order control on hillslope hydrology and stability, significantly improving simplified homogeneous representations. A new methodology was presented to integrate geophysical information from seismic refraction surveys with numerical modeling of topographic stresses to constrain spatially variable subsurface hydraulic conductivity within deep CZ, leading to improved simulation of soil saturation patterns and landslide prediction.

6.2 Limitations and future work

Despite the advances presented, several limitations remain, primarily related to: i) slope stability modeling in the Alto Adige study and ii) the general availability of high-resolution field data. Future research will focus on extending the mechanical component of the LFS approach from 2-D to 3-D, enabling the explicit representation of lateral stress redistribution and a more realistic characterization of catchment-scale stress field and LFS-determined unstable area.

The availability of site-specific field measurements is essential for accurately characterizing the complex CZ structure and its spatially variable properties, including soil and bedrock depth as well as hydro-mechanical parameters. In the absence of such data, large-scale datasets must be used, which may not adequately capture local conditions. For this reason, geophysical techniques play a key role by providing deep, quantitative information that supports multi-source validation and data-constrained modeling of CZ architecture. These surveys must be complemented by borehole logging, test pits, and cores to acquire detailed information on the local stratigraphy and to collect undisturbed soil samples for laboratory experiments. Additionally, in-situ hydraulic tests, such as sprinkling experiments and tracer studies, and the deployment of piezometers, tensiometers, TDR sensors, or lysimeters enhance the estimation of hillslope hydrological response and water balance.

From an operational perspective, the proposed framework could support Early Warning Systems for rainfall-induced hazards by providing a more physically based representation of subsurface controls on slope instability and improving process-based warning alarms. However, several limitations hinder its large-scale implementation. The parameterization complexity and the need for detailed subsurface characterization constrain scalability, as such data are rarely available across broad regions. This work suggests that future efforts should focus on identifying geomorphological proxies, such as using topographic stress-field modeling or seismic-derived trends, to infer hidden CZ architecture where direct subsurface measurements are missing. In addition, the computational cost of fully coupled hydro-mechanical simulations may limit real-time applications, unless supported by high-performance computing or focused on high-risk “hot-spot” areas. Future developments should therefore aim at reducing model complexity and exploring simplified or hybrid approaches to balance physical realism and operational efficiency.

Building on these needs, I plan to continue my research on the CZ at ETH Zürich, where I will conduct comprehensive field measurements, deploy monitoring instruments, and apply numerical modeling tools to better understand subsurface controls on hydrological processes and landslide susceptibility in the Swiss Alps, a region characterized by geomorphic settings transitioning toward deglaciated and fractured landscapes rather than dominated by physical-chemical weathering.

6.3 Final comments

Characterizing CZ structure and hydro-mechanical properties is fundamental to understanding how different hillslopes regulate near-surface hydrological responses. Variations in CZ depth, geometry, stratification, and degree of weathering control where and when water infiltrates, accumulates, or drains, thereby dictating the timing and magnitude of floods, droughts, and landslide initiation. Integrating geophysical data, field surveys and monitoring, and physically based modeling enables a realistic representation of subsurface heterogeneity and provides a robust framework for interpreting CZ processes, guiding the development of improved hydrological forecasting tools and supporting the implementation of early warning and pre-alert systems for geohazard mitigation. By offering physically meaningful and transferable insights into CZ hillslope hydrology and stability, this work contributes to enhance landslide forecasting and decision-making for local authorities operating in landslide-prone environments and assist researchers in creating more reliable forecasting tools to characterize and simulate the CZ processes.

Supplementary Material

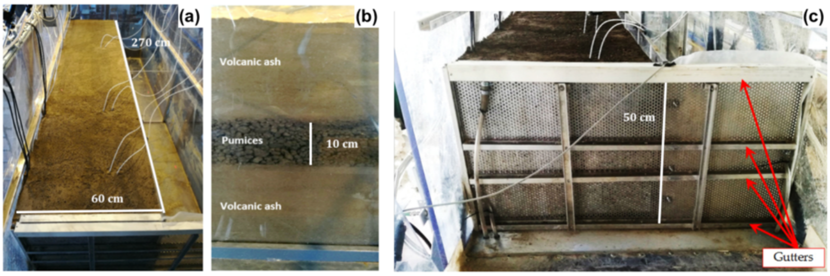

Figure S1. Laboratory physical model (a) view from above, (b) lateral view showing the layered soil (detail), (c) downstream outlet gutters (from Capparelli et al. 2020).

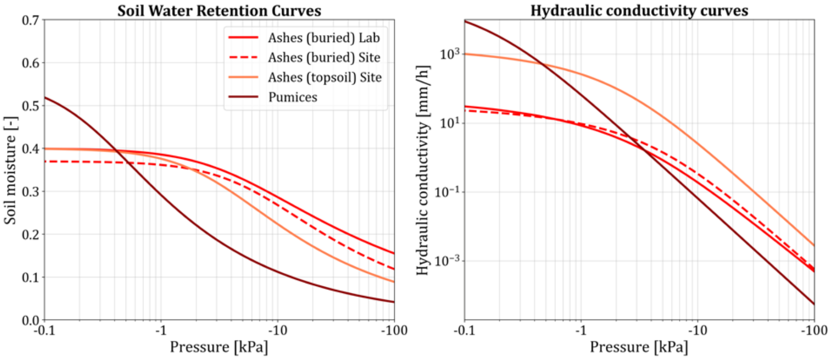

Figure S2. (a) Soil water retention curves and (b) Hydraulic conductivity curves for ashes (topsoil and buried layers) and pumices.

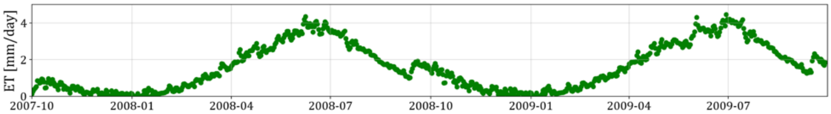

Figure S3. Application 2 results. Daily actual evapotranspiration.

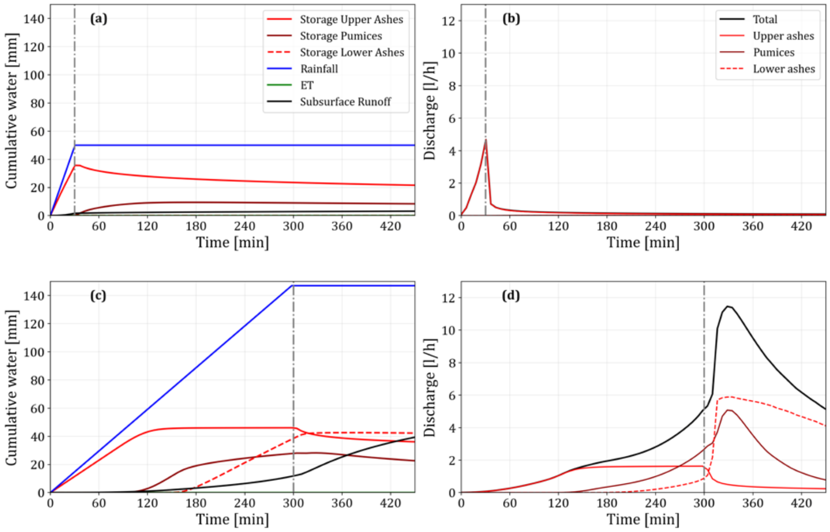

Figure S4. Application 1 results. (a) water balance and (b) lateral subsurface runoff redistribution for high intensity/short duration rainfall; (c) water balance and (d) lateral subsurface runoff redistribution for medium-low intensity/long duration rainfall. The dashed vertical lines represent the moments when applied rainfall stops.

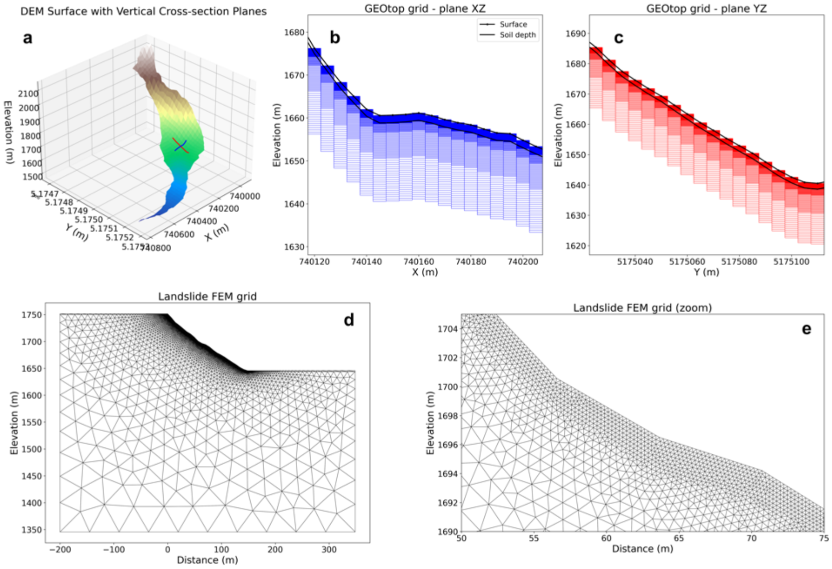

Figure S5. Computational grids: a) 3D view of a digital elevation model with vertical cross section planes (North-South in red and East-West in blue); b) XZ-view of the 3D GEOtop grid; c) YZ-view of the 3D GEOtop grid; d) 2D unstructured mesh used in the landslide model, and e) a zoom closer to the surface.

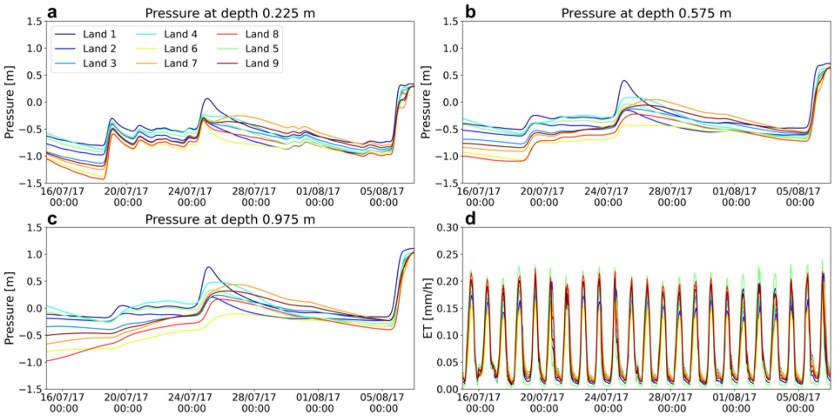

Figure S6. Hydrological model results: a), b) and c) pressure time series at different depth; d) evapotranspiration. Results are shown for all 9 landslide sites and up to three weeks before the storm.

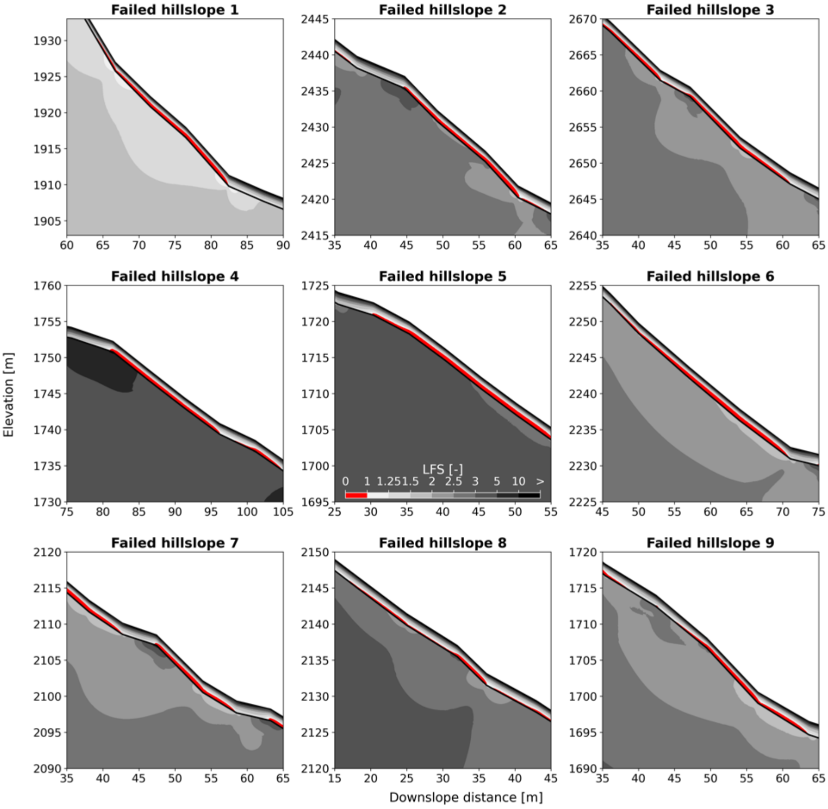

Figure S7. Results of the Monte Carlo uncertainty analysis. Cross sections of 9 hillslopes within the Braies catchment at the timing of landslide occurrences. The LFS, here the 5% quantile, is mapped along each hillslope, with darker shades representing areas of higher stability. The red segments indicate portions of the soil where LFS≤1, corresponding to the initiation zones of landslides.

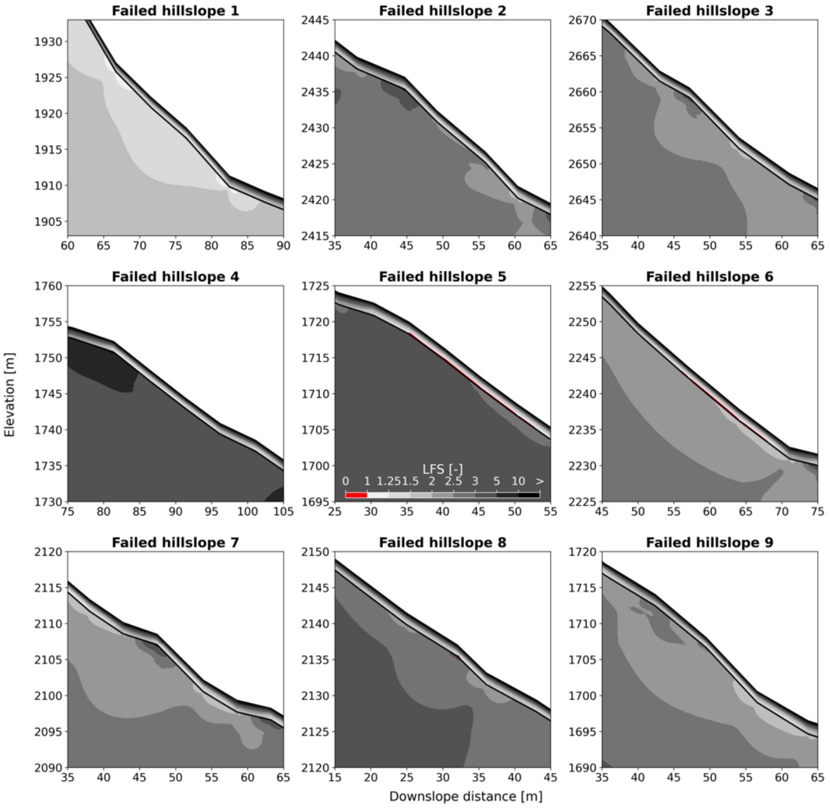

Figure S8. Results of the Monte Carlo uncertainty analysis. Cross sections of 9 hillslopes within the Braies catchment at the timing of landslide occurrences. The LFS, here the 95% quantile, is mapped along each hillslope, with darker shades representing areas of higher stability. The red segments indicate portions of the soil where LFS≤1, corresponding to the initiation zones of landslides.

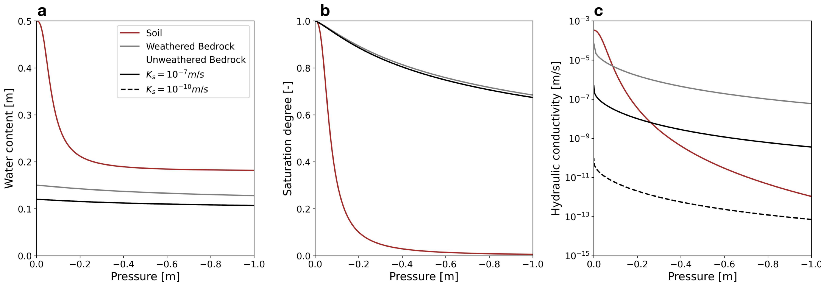

Figure S9. (a) Soil water retention curve (SWRC, values from Ebel at el. 2008) in terms of pressure and water content; (b) SWRC in terms of pressure and saturation degree; (c) Hydraulic conductivity function (HCF, values from Ebel at el. 2008) in terms of pressure and unsaturated hydraulic conductivity. Hydraulic parameters are described in Tab. 4. The curves are displayed for each layer, i.e., soil (brown line), weathered bedrock (grey line) permeable (black line, k_s=10^{-7} m/s, Ebel at el. 2007b) and less permeable (dashed black line, k_s=10^{-10} m/s, Rempe and Dietrich 2014) unweathered bedrock. In panels (a) and (b), the SWRCs of the two unweathered bedrocks overlap, as they share identical hydraulic parameters except k_s.*

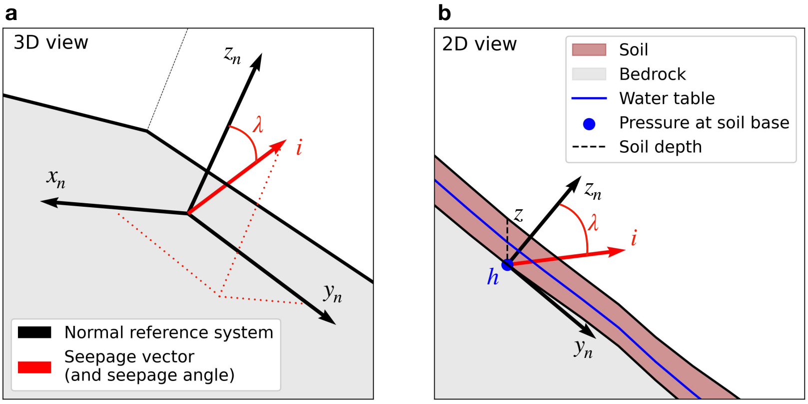

Figure S10. Three-dimensional (a) and two-dimensional (b) visualization of the hydrological quantities computed in this study. The soil saturation ratio (h/z) is defined as the ratio of the pressure head at the soil base to the soil thickness. The seepage angle (λ) is the 3D angle between the seepage vector (i) at the soil base and the vertical axis of a local reference system oriented normal to the soil base.

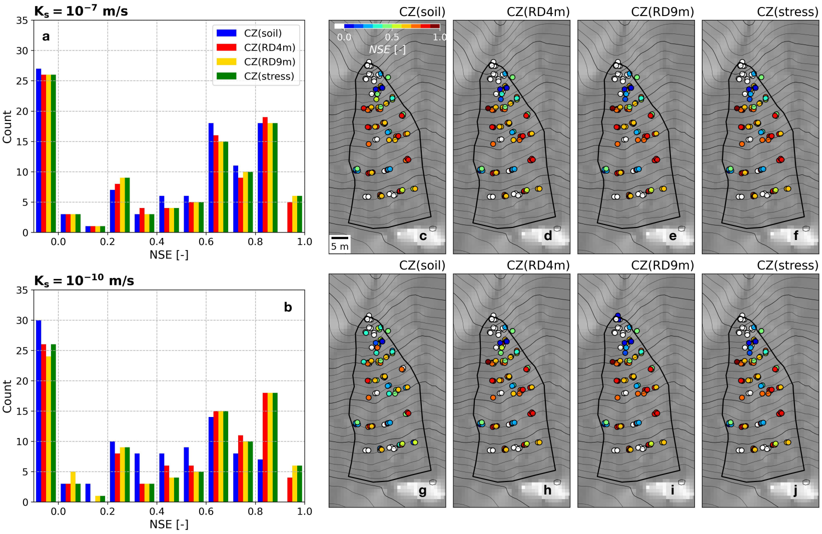

Figure S11. EXP results. (a) histogram and (c, d, e, f) spatial variation of NSE across all CZ for k_s=10^{-7} m/s. (b, g, h, i, j) The same for k_s=10^{-10} m/s.

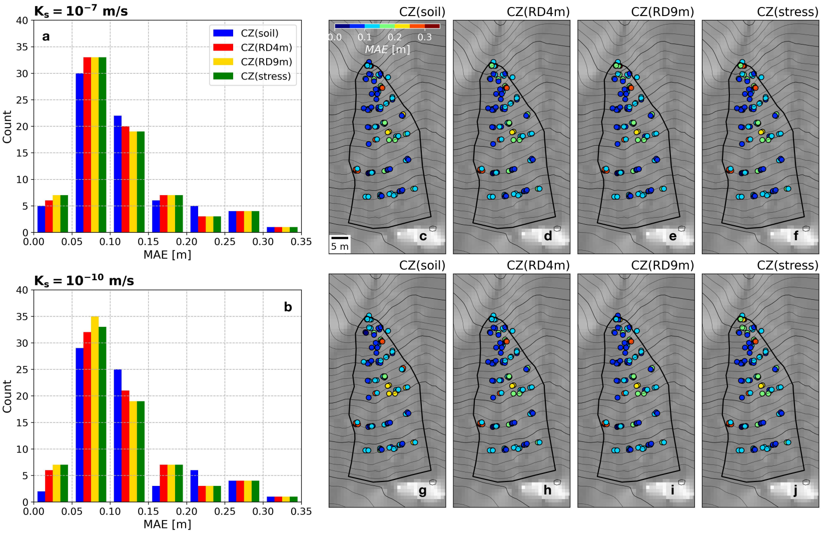

Figure S12. EXP results. (a) histogram and (c, d, e, f) spatial variation of MAE across all CZ for k_s=10^{-7} m/s. (b, g, h, i, j) The same for k_s=10^{-10} m/s.

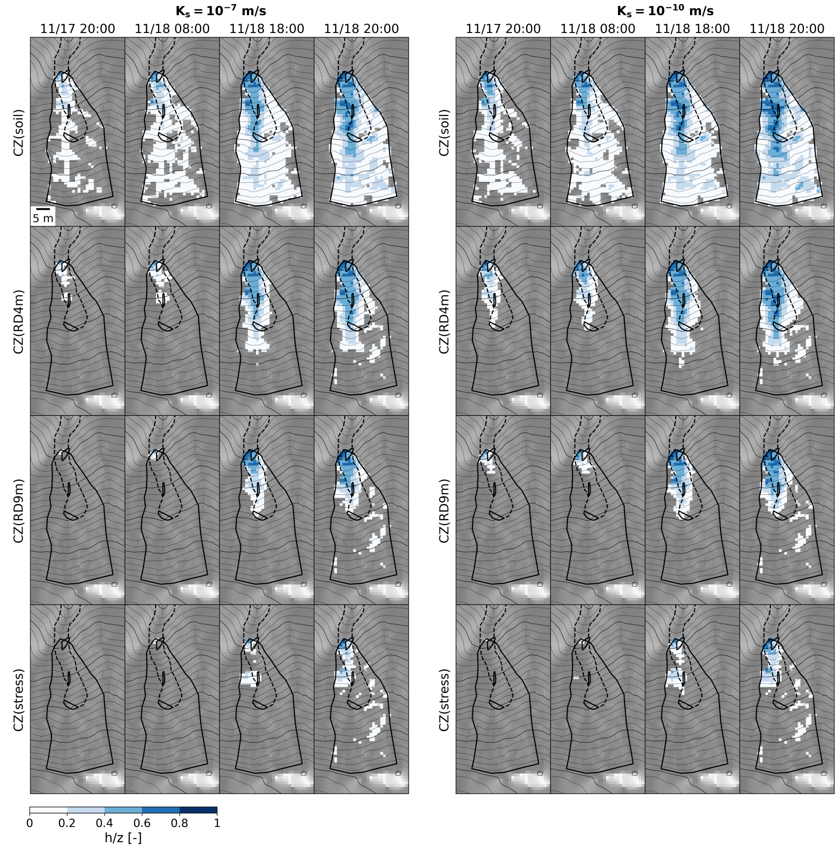

Figure S13. STORM results. Simulated saturation ratio at soil base (h/z) for each CZ scenario subdivided by $k_s=10^{-7}$ *m/s (left panels) and* $k_s=10^{-10}$ *m/s (right panels) at landslide timing, 2, 12 and 24 hours before. From top to bottom, the degree of bedrock weathering increases, while from left to right, the time approaches the landslide event. Dashed black line is the 1996 CB1 landslide scar, continuous black lines are the fractures exposed after the event.*

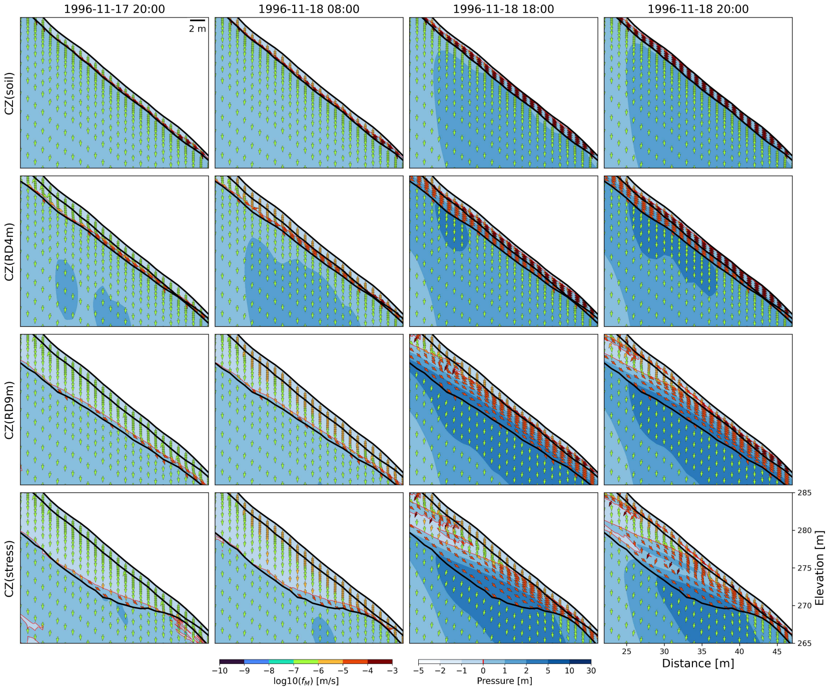

Figure S14. STORM results. North-South cross section showing pore water pressure field, flux directions and magnitude (in log scale) for each CZ scenario for $k_s=10^{-7}$ *m/s case, at landslide timing, 2, 12 and 24 hours before. From top to bottom, the degree of bedrock weathering increases, while from left to right, the time approaches the landslide event. Black lines represent topographic surface, soil base and if present, weathered bedrock bottom. The red line represents the position of the water table.*

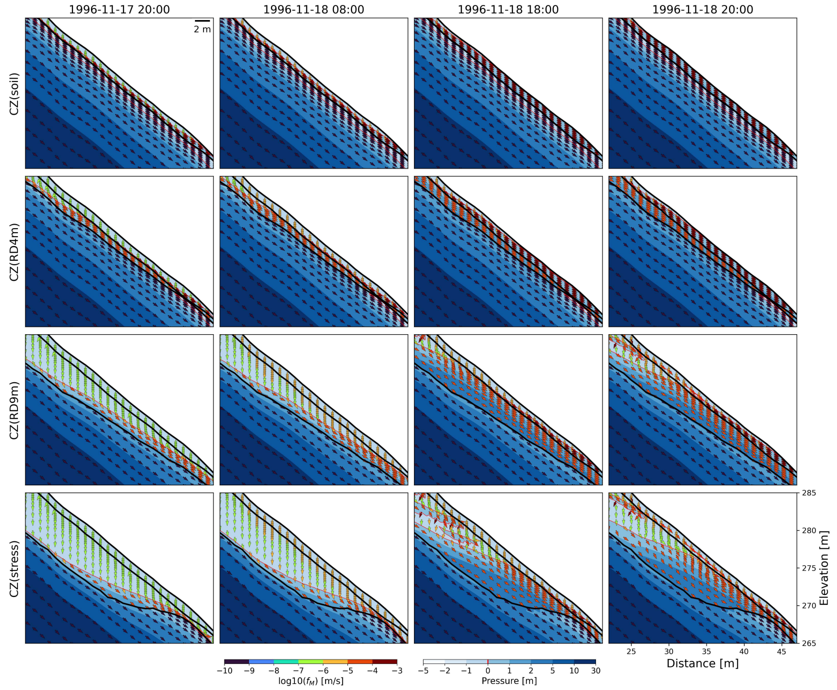

Figure S15. STORM results. North-South cross section showing pore water pressure field, flux directions and magnitude (in log scale) for each CZ scenario for $k_s=10^{-10}$ *m/s case, at landslide timing, 2, 12 and 24 hours before. From top to bottom, the degree of bedrock weathering increases, while from left to right, the time approaches the landslide event. Black lines represent topographic surface, soil base and if present, weathered bedrock bottom. The red line represents the position of the water table.*

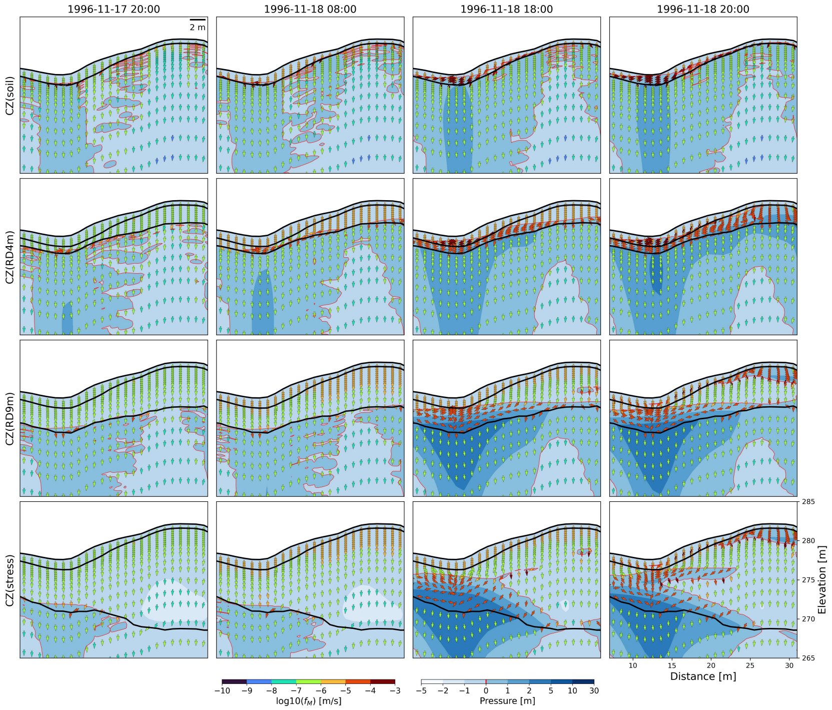

Figure S16. STORM results. East-West cross section showing pore water pressure field, flux directions and magnitude (in log scale) for each CZ scenario for for $k_S=10^{-7}$ m/s case, at landslide timing, 2, 12 and 24 hours before. From top to bottom, the degree of bedrock weathering increases, while from left to right, the time approaches the landslide event. Black lines represent topographic surface, soil base and if present, weathered bedrock bottom. The red line represents the position of the water table.

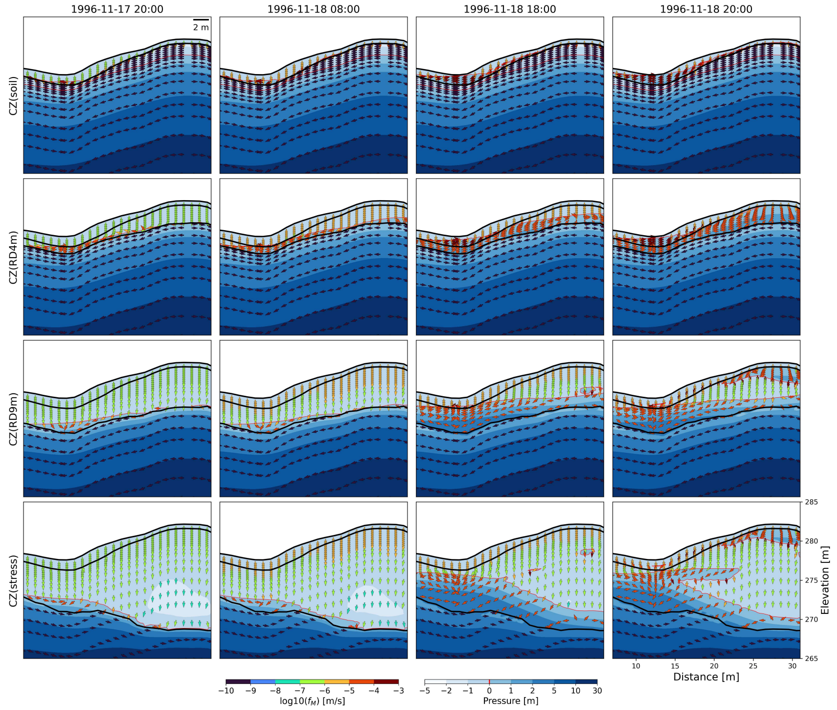

Figure S17. STORM results. East-West cross section showing pore water pressure field, flux directions and magnitude (in log scale) for each CZ scenario for $k_s=10^{-10}$ *m/s case, at landslide timing, 2, 12 and 24 hours before. From top to bottom, the degree of bedrock weathering increases, while from left to right, the time approaches the landslide event. Black lines represent topographic surface, soil base and if present, weathered bedrock bottom. The red line represents the position of the water table.*

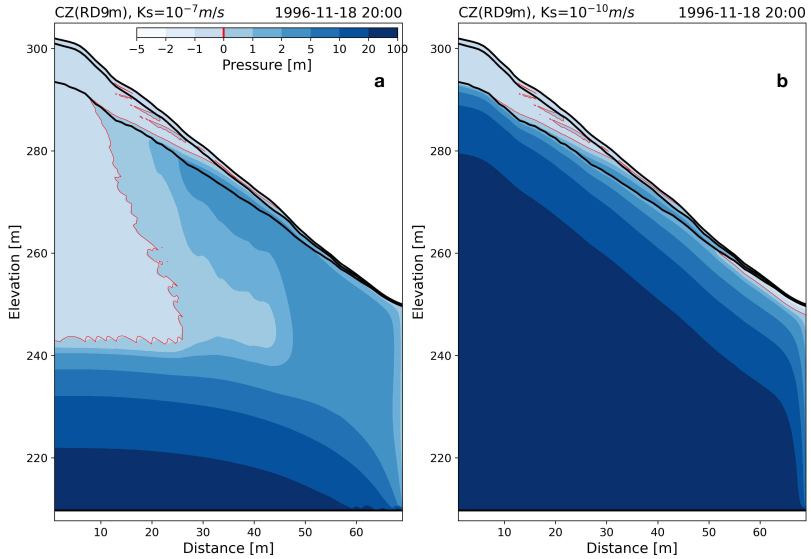

Figure S18. STORM results. North-South full-extent profile (bottom boundary at 40 m depth below lower weir) showing pressure field at landslide time for CZ(RD9m) scenario for bedrock conductivities 10^{-7} m/s (a) and 10^{-10} m/s (b).

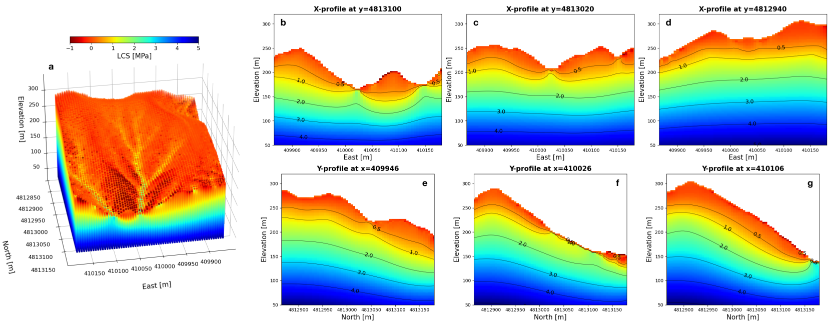

Figure S19. (a) 3D results of the LCS for Mettman Ridge. (b,c,d) East-West profiles of LCS for different North coordinates. (e,f,g) North-South profiles of LCS for different East coodinates.